IMPACTS OF ACQUISITION FOOTPRINT

ON SEISMIC ATTRIBUTE ANALYSIS

A Thesis

Presented to

The Faculty of the Department of Geosciences

University of Houston

In Partial Fulfillment

of the Requirements for the Degree

Master of Science

By

Burcin Inanli

December 2002

ACKNOWLEDGMENTS

I am very thankful to people who serve, challenge, encourage, support me throughout my academic program in the University of Houston. My sincere appreciation especially goes to my advisor, Dr. Kurt J. Marfurt, and my committee members, Dr. Bob Wiley, Dr. Hua-Wei Zhou, and Dr. Edip Baysal for their excellent ability of instruction, leading and patience. I am also very grateful to Dr. Orhan Yilmaz, Irfan Tanritanir, and Cory Hoelting who had contributed great efforts to my thesis at Paradigm Geophysical Company and the University of Houston. I would like to thank Dr. K.K. Sekharan, Jay Krishnan, and all my friends at the University of Houston for their friendship and support. In addition, thanks to Paradigm Geophysical Company and GX Technologies for providing a royalty-free license to AGL for use in education and research. The last but not the least, I am deeply thankful to my family.

ABSTRACT

Seismic data quality is impacted not only by fold, but also by the distribution of source-receiver offsets and azimuths that make up this fold. The impact of the seismic acquisition program on processing and on the quality of the final image is commonly called acquisition footprint. The seismic acquisition program impacts the quality of the subsurface image in several ways, the most fundamental of which is subsurface illumination. A more subtle impact of the seismic acquisition program, and the object of this work, is the variation of amplitude and signal-to-noise ratio as a function of illumination angle and backscattered coherent noise.

The acquisition footprint signature of land acquisition programs and of obstacles that modify these programs is well known, through not necessarily well treated at this time. The impact of more recent advances in seismic acquisition, including using an increasing number of marine towed streamers, vertical cables, and ocean bottom cables are less well known. The impact of acquisition footprint on seismic attribute analysis has been barely addressed.

To understand the impact of marine survey design on acquisition footprint analysis, I acquired 3-D multi-streamer marine data over a physical model containing complex channel structures sandwiched between simple homogenous and isotropic elastic layers. In this work, I addressed the impact of acquisition footprint on seismic attributes and illumination by employing conventional processing methods and a suite of different migration algorithms.

CONTENTS

Chapter 1

INTRODUCTION

1.1 Acquisition Footprint Signature

Acquisition footprint is defined as an artifact that is introduced in the final seismic results due to the 3-D acquisition geometry (Moldoveanu and Ronen, 1999). Fold, offset distribution, and azimuth distribution characterize each 3-D acquisition geometry. The choice of acquisition design can bias the data binning in terms of offset and azimuth that cause biased NMO stretch and amplitude variation with offset [AVO] (Marfurt, *et. al.*, 1998). The acquisition footprint signature of land acquisition programs as well as obstacles on seismic data has been well studied (Hill, *et. al.*, 1999). 3-D land seismic acquisition surveys have great flexibility that provide a wide distribution of offsets and azimuths in any given bin (Stone, 1994). Hill (1999) shows periodicity in signal due to inaccurate velocity estimation and AVO. In this case, unwanted amplitude contamination in traces cannot be easily discerned. The acquisition footprint in land 3-D data is more apparent because of the greater lateral variability in offsets in different bins. Seismic attributes need to be interpreted with these artifacts in mind. The impact of acquisition footprint on seismic attribute analysis is more subtle in the marine environment. Single streamer marine data collected in seas without strong currents provide nearly uniform subsurface coverage. More modern, multistreamer acquisition surveys cover more

surface area per unit time and cost. Such multi-streamer surveys cause periodic variations in source-receiver offset and azimuth in each CMP gather (Calderon, *et. al.*, 1999). The periodicity in offset and azimuth trace distributions is preserved through processing using DMO and common offset prestack migration sections of seismic data.

Vertical cables (VC) provide an extremely rich suite of azimuths in the marine environment (Krail, 1994). Appropriate vertical hydrophone distance in each anchored cable and dense areal shot coverage can yield higher resolution seismic data than surface streamer acquisition. Vertical cable data also are amenable to an economic common receiver wave equation migration flow. However, the quality of VC data may suffer from large azimuthal variations of vertical cable deployments as well as a lack of stabilization due to strong underwater currents. Such limitations may result in inadequate attenuation of coherent noise including multiples and back-scattered noise from a rugose sea floor (Moldoveanu and Ronen, 1999). Such acquisition footprints on the processed seismic section may lead to the misinterpretation of seismic attributes.

Like vertical cables, Ocean Bottom Cables (OBC) are a recently developed technology that has acquisition flexibility and promises to reveal information both from S-waves and P-waves. In conventional P-P AVO analysis, high frequency V_p/V_s ratios are estimated from the variation of amplitude with offset being more sensitive to shear wave impedance changes. Converted wave analysis provides similar information on shorter offsets. In addition, 3-D OBC technology can provide the direct measurement of V_p and V_s from conventional traveltime analysis. This background or low frequency estimate of V_s

information helps constrain our lithology estimation. OBC technology suffers from many challenges, among them the inability of exactly positioning the cable on the sea floor (Entralgo and Spitz, 2001). In addition, the subsurface coverage, and hence fold and azimuth distribution of PS sections, is different from PP sections. To my knowledge, no one has yet analyzed the differences in acquisition footprint between PP and PS waves.

1.2 Review of Techniques to Suppress Acquisition Footprint

A major problem with today's 3-D surveys is the acquisition footprint that appears on the final migrated volume. These artifacts can cause misinterpretations on both vertical and horizontal seismic sections and slices. Shot generated coherent noise, variation in fold, azimuth and offsets, and errors in velocity estimation all contribute to acquisition footprint. Under these conditions and if budget limitations constraint our acquisition program, acquisition footprint is best treated during the conventional data processing phase. In this section, I will provide an overview of recent developments regarding the acquisition footprint attenuation in both phases.

In reality, the surface multi-streamer and single-streamer marine surveys always involve fold, azimuth, and bin irregularities due to survey directions and streamer feathering. However, it is often possible to modify a marine survey to minimize acquisition footprint. For instance, (La Bella *et. al.*, 1998) used a marine cross-shooting technique to reduce footprint on a 1600 km^2 survey in the Adriatic sea. The key characteristic of this concept

is to acquire two data sets at right angles to each other (Figure 1.2.1), much like a conventional wave test.

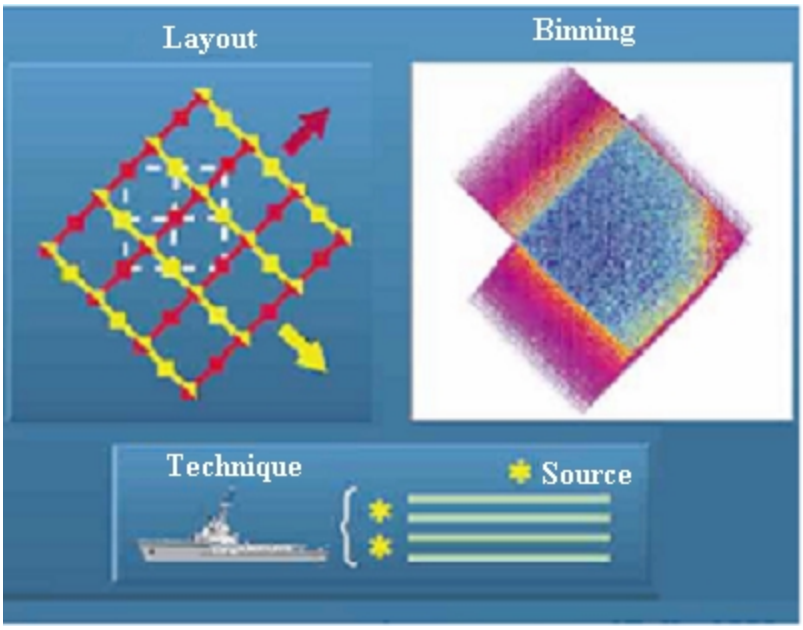

FIG.1.2.1. Cross-shooting acquisition layout and relevant binning (after La Bella *et. al.*, 1998).

This methodology enhances azimuth sampling, and especially the number of near offset traces, thereby increasing the accuracy of velocity analysis, and the quality of AVO angle stacks. The result of this particular survey demonstrates that not only amplitude and frequency content of the data are preserved between the two 'merged' surveys, but also the acquisition footprint is remarkably reduced in the combined section (Figure 1.2.2).

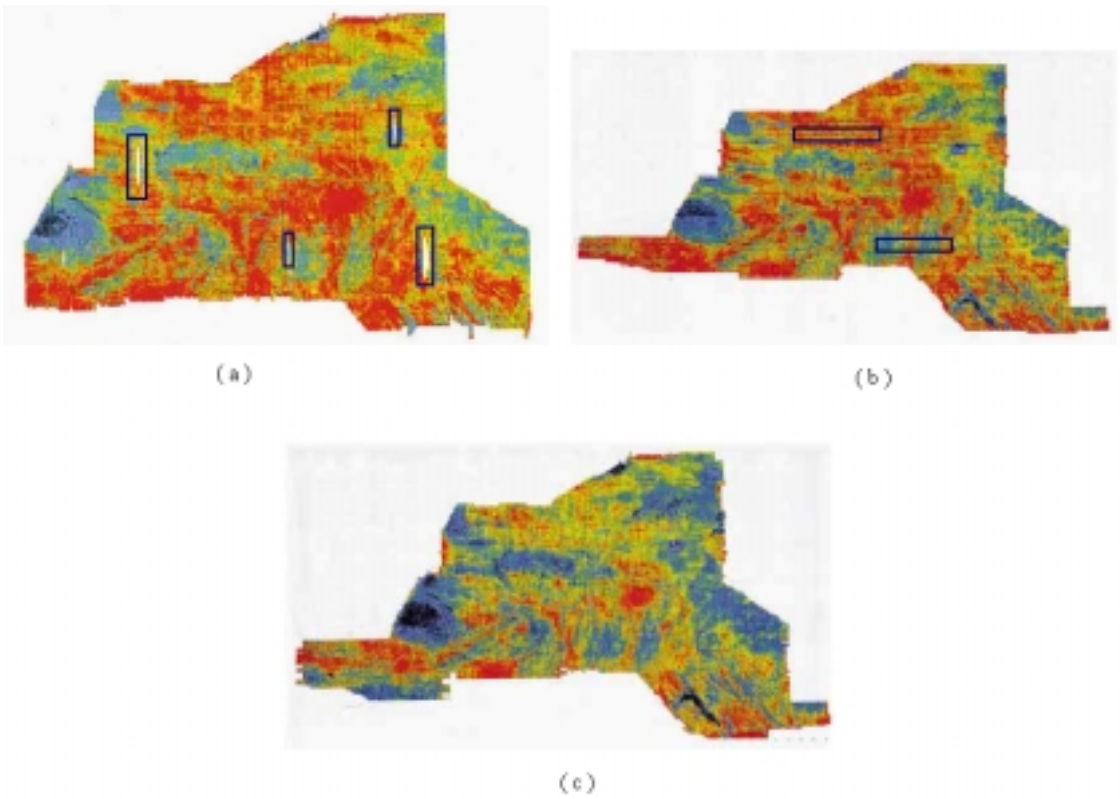

FIG.1.2.2. Time slice at 1995 ms of the survey, (a) dip direction, (b) strike direction, and (c) combined surveys. After La Bella *et. al.*, (1998). Blue rectangles indicate acquisition footprint.

For economic reasons, the careful survey design described above is not routinely used to minimize acquisition footprint in the marine environment. Acquisition footprint may also be partially suppressed during the data processing phase, either before or after migration. The most common technique in the literature is dip filtering of acquisition footprint where the entire data volume is transferred into the (ω, k_x, k_y) domain. The interpreter identifies key spectral components of the footprint, mutes them, and transforms back to the (x, y, z) domain (Soubaras, 2002; Gulunay, 1999). A noteworthy study was done by

Marfurt *et. al.* (1998) in which the data volume was treated in the (τ, p, q) domain using an efficient running window algorithm. For poor quality sets of data, the (τ, p, q) approach yields the possibility of post-stack (τ, p, q) predictive deconvolution as well as a nonlinear weighting of the coherent signal. A variation of the (ω, k_x, k_y) method that recognizes the change of footprint with depth is to filter the data time slice by time slice in the (t, k_x, k_y) domain (Drummond *et. al.*, 2001). To address data spacing (but not back scattered noise) Canning and Gardner (1998), and Chiu and Stolt, (2002) have developed improved data mapping and reconstruction algorithms. In this approach, each input trace is weighted with respect to its neighbors and input to a general 3-D pre-stack migration integral :

$$m(x, y, z) = \int w(S,R) \frac{d}{dt} d(\tau, S, R)\, dS\, dR \quad , \qquad (1.2.1)$$

where, S and R are the source and receiver coordinates,

d indicates the data,

m is the migrated reflectivity,

τ is the travel time in seconds along the diffraction surface ,and

w (S,R) is a weighting function.

The theory emphasizes that for an irregular geometry, dR and dS, the weighting coefficients should be evaluated for each data point according to the relative portion of the space that it represents (Figure 1.2.3).

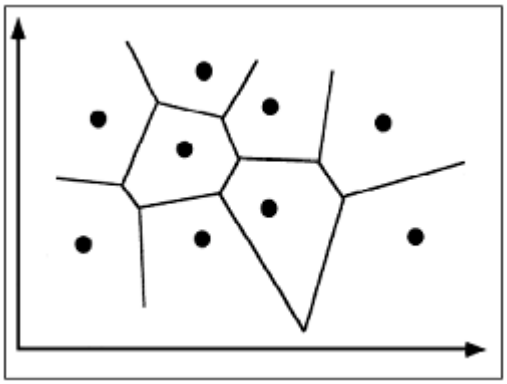

FIG.1.2.3 Map view of the polygons constructed around each trace to calculate weighting factor (w). After Canning and Gardner (1998).

In regions where the traces are close, the weighting factor (w) has a small value, while sparse trace distribution requires the assignment of a large value of weighting. Figure 1.2.4 shows the success of this implementation on 3-D pre-stack migration of 3-D synthetic irregular survey data before and after using the weighting factor.

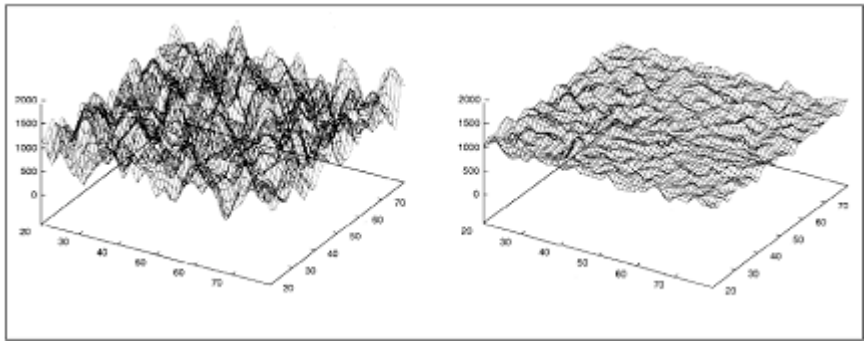

FIG.1.2.4. Results of 3-D pre-stack migration without weights of the 3-D survey (left) and with weights (right). The ideal response of the data mapping and reconstruction technique should look like the one shown on the right. After Canning and Gardner (1998).

Stolt (2000) addresses data irregularity using a 3-D data mapping and reconstruction (DRC) algorithm). The DRC algorithm approximates the 3-D integral equation by a straight path Kirchhoff-like solution and obtains an azimuth moveout operator (AMO). Theoretically, the 3-D operator transforms the data for a given source-receiver configuration to a different source-receiver configuration. The DRC algorithm holds promise in data regularization, interpolation of missing data, and azimuth moveout. Figure 1.2.5 demonstrates common offset section of 3-D land dataset before and after successful implementation of the DRC algorithm.

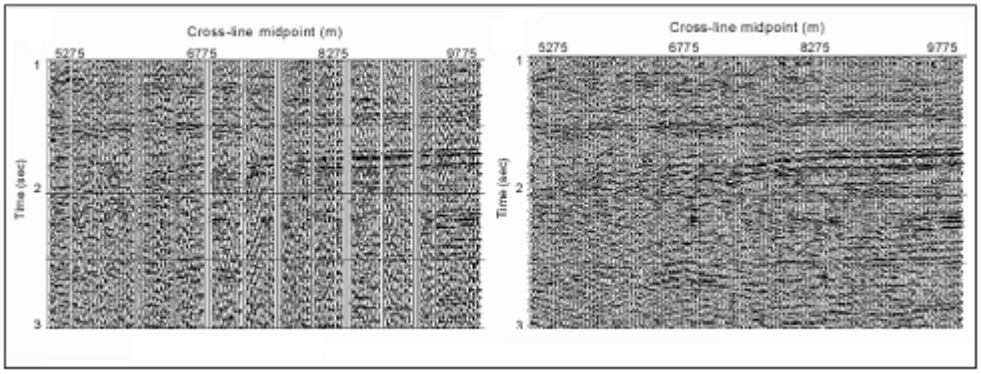

FIG.1.2.5. Common offset section of 3-D land dataset before (left) and after (right) the DRC method is implemented. After Chiu and Stolt (2002).

We should note that while the Canning and Gardner (1998) and Chiu and Stolt (2002) methods compensate for irregular trace spacing, they do not help in suppressing back-scattered seismic noise. In many if not most cases (e.g. Drummond *et. al.*, 2001), leakage

of back-scattered noise into the stack (or migration stack) array is the principal cause of acquisition footprint.

By this review, I hope to demonstrate that acquisition footprint is an active area of research. The goal of my thesis is not to add to these suppression techniques, but rather to show how 3-D physical models can provide economic 3-D data of alternative acquisition schemes for others to evaluate these processing flows.

1.3 Tools for Research

In this project, I acquired 3-D four-streamer data over a physical model made of simple homogenous and isotropic layers containing complex channel structures (see Chapter 2, Figure 2.2) at the Allied Geophysical Laboratories (AGL) of the University of Houston. Physical modeling is a tool that provides realistic studies of elastic wave propagation containing reflection, refraction, and noise events. Given known velocity model, structure and survey parameters, I will process the physical model dataset by applying a suite of conventional processing techniques to increase the signal-to-noise ratio. Furthermore, I will attempt to investigate the influence of acquisition geometry on a suite of attribute analyses. In fact, such attribute analyses serve as a quantitative means of measuring the impact of acquisition footprint on seismic reflections.

In conjunction with the physical model experiment, I also conducted a numerical modeling experiment based on the physical model survey and parameters (see Appendix C). This study provided comparative results of imaging efforts on both numerical and physical models. These efforts can also be utilized as guidance for developing migration algorithms in the future.

1.4 Organization of Chapters

In Chapter 2, I describe the physical model construction technique and document the material specifications used in creating the physical model. Also, I address the methodology for multi-streamer acquisition and the acquisition geometry over the model.

In Chapter 3, I address the data processing flow used on 3-D physical model dataset. To increase signal-to-noise ratio, I compare these results with those from an idealized numerical model using asymptotic ray theory.

In Chapter 4, I show the impact of acquisition footprint on a suite of attributes.

In Chapter 5, I register final concluding remarks as well as future plans and suggestions.

In Appendix A, I describe the laser profilometry study from A to Z. In this work, I mainly focus on generating 3-D spatial coordinates for channel model used in numerical modeling.

In Appendix B, I review piezoelectric components, and describe measurements of the transducer radiation patterns.

Finally in Appendix C, I address the 3-D ray trace modeling experiment.

Chapter 2

PHYSICAL MODELING

2.1 Model Construction

Construction methods of physical models vary depending on both the materials used and the complexity of the earth structures to be simulated. Because of the 1:10000 scale factor we commonly use, we need to accurately measure P and S velocities as well as reflector surfaces. Over many years in the AGL, different physical model materials have been molded, milled and ground. Plexiglas, PVC, glass, epoxy resin, rubber, and metals have proven to be excellent candidates. These materials are easily worked, have reproducible velocities and densities, low attenuation, and may simulate limestone, sandstone, shale, and salt dome structures in the real world. Recently the AGL has experimented with new materials in collaboration with the UH Art Department consisting of marble and baked clay. For example, Wardhana (2001) used sintered glass beads to build a porous channel in order to simulate a time-lapse physical model experiment.

In this study, which aims to evaluate the sensitivity of edge detection attributes on physical model data over channels in the presence of acquisition footprint, I used conventional materials that have been used for over two decades in the AGL: plexiglas,

and black epoxy resin; indeed, the milled plexiglas channel structure I embedded in my model was actually created in the distant past by some unknown AGL student who may already have retired from a successful career in geophysics. In Appendix A, I describe how I obtain detailed measurements of each individual channel using laser profilometry (Figure 2.1). These surfaces will be used in subsequent numerical modeling and in calibrating my final images.

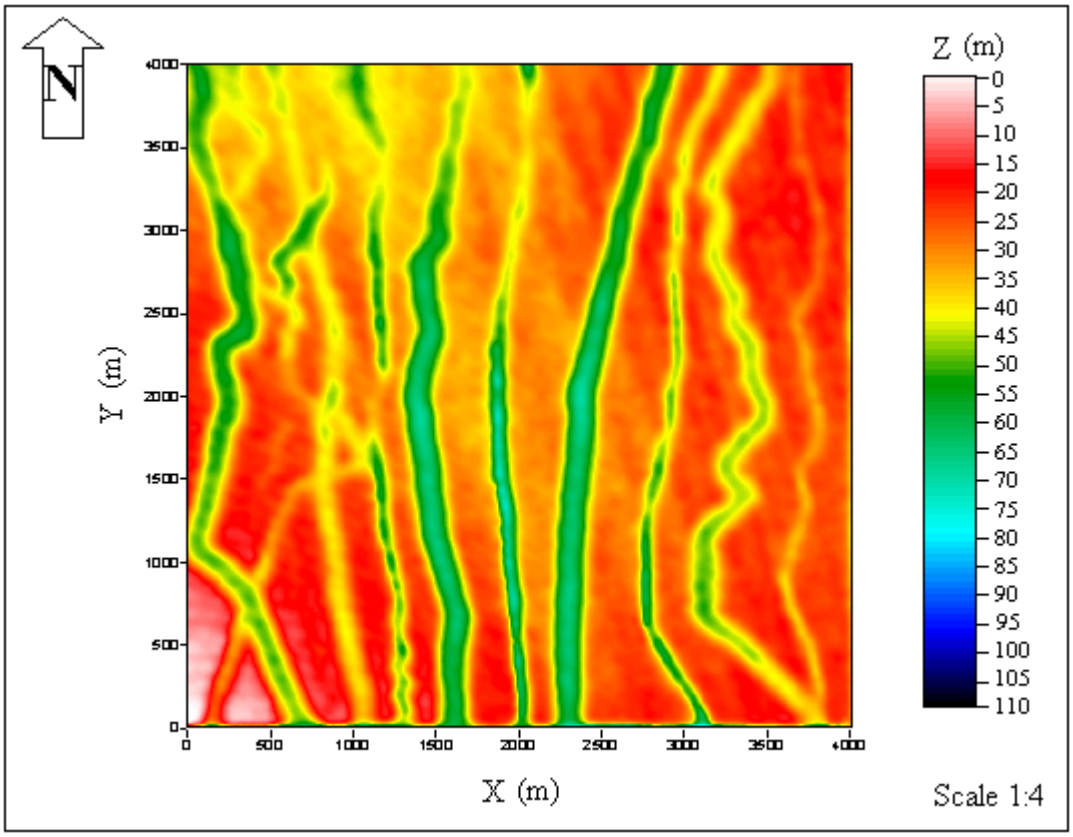

FIG. 2.1. Scanned image of plexiglas channel model before being filled with resin in world coordinates (10^4 * physical model coordinates) obtained using laser profilometry.

As a first step, I performed some back of the envelope calculations on seismic wave scattering from these channels in order to design my acquisition and predict my final

seismic image. Both vertical and horizontal resolution are important in mapping channels. The source bandwidth, seismic aperture, as well as the processing flow control our resolution. A well-designed deconvolution operator may help broaden the spectrum and thereby increase the vertical resolution, while a well-designed migration may improve the lateral resolution by narrowing or compressing the Fresnel Zone (Sheriff, 1984). Both lateral and vertical resolution can be estimated by knowing the velocity field and dominant frequency of the geologic structure of concern. The limit on vertical resolution is primarily dependent on the thickness of our channels, and is usually defined as 1/4 of the dominant wavelength, λ:

$$\lambda = \nu / f \,, \tag{2.1}$$

where ν is the velocity in m/s, and f is the dominant frequency in Hz. In Figure 2.1 where the channel thicknesses are displayed in color, we note variation between 5 and 80 m. Hence, for my signal centered about 30 Hz (in world coordinates) propagating in a medium of 2100 m/s, I expect unresolved results for thicknesses $h = \lambda/4 < 17.5$ m. Thus, those channels colored from dark red to dark blue will be well resolved. The lateral resolution is a measure of how close two points can be located next to each other. This threshold is also determined by the dominant frequency and the velocity of a medium. The lateral resolution of unmigrated data can be given by the Fresnel zone equation (Yilmaz, 1987):

$$r = (\nu / 2) * (t / f)^{\frac{1}{2}} \,, \tag{2.2}$$

where r is the horizontal limit or Fresnel zone radius in m, ν is the velocity of a medium in m/s, t is the two-way time in s, and f is the frequency in Hz. We observe that channel widths in Figure 2.1 vary between 1 to 500 m. With a dominant frequency, f = 30 Hz, velocity, v = 2100 m/s velocity, and a two-way travel time, t = 1.53 s, the minimum horizontal resolution of unmigrated data is 237 m. By using high angle diffractions, seismic migration significantly increases the horizontal resolution. The migrated seismic image in Figure 3.11.1, Chapter 3, shows that we are able to resolve the channels with a minimum width of 210 m . Since the aim of this project is to detect the edge of the channels by using a suite of alternative seismic attributes and to analyze the impacts of acquisition footprint on these attributes, I did not only consider this low horizontal resolution problem, but also diffractions from the channel edges while designing the multistreamer acquisition program.

The physical model consists of 5 layers. The black epoxy resin filled channel (layer 3) is squeezed in between a 120 m thick top acrylic plexiglas (layer 2) and a 500 m thick bottom acrylic plexiglas (layer 4). Finally, this structure is covered on top by a 500 m thick first black epoxy resin (layer 1) and on the bottom by a final 200 m thick black epoxy resin (layer 5). In order to prevent water leakage into this structure, an extra 250 m thick black epoxy resin covers sides of the model (Figure 2.2).

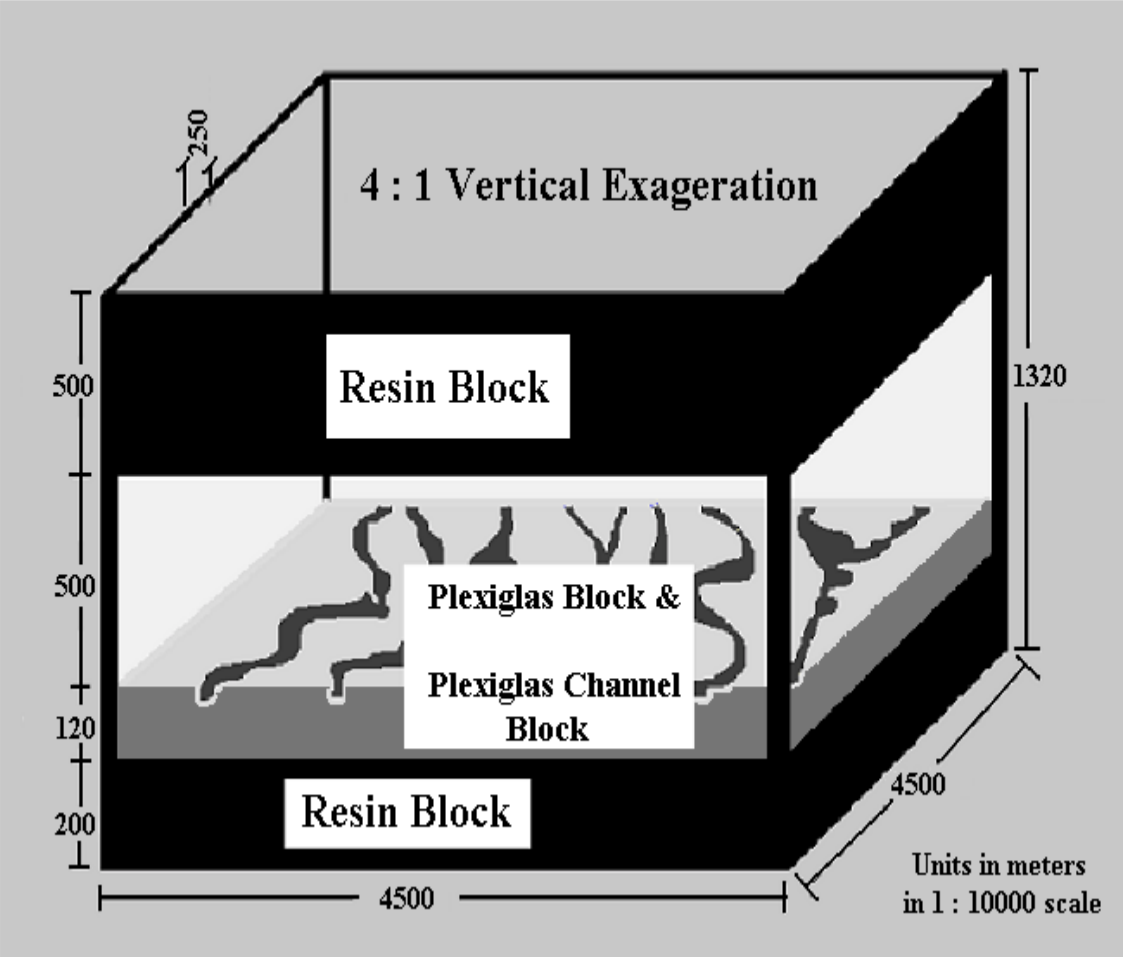

FIG. 2.2. The physical model consists of five layers. The top layer (layer 1) consists of 5 cm thick black epoxy resin. Layer 2 is a 5 cm thick plexiglas. Layer 3 is the channels filled with black epoxy resin. Layer 4 is a 1.2 cm of plexiglas. Finally, layer 5 is a 2 cm thick black epoxy resin World coordinates are displayed in the figure such that the 45cm*45cm*13.2cm physical model represents a 4500m*4500m*1320m section of the earth.

To constrain the shape and size of the layers, I built a square rectangular metal mold with the dimensions of 45 * 45 * 15 cm^3. I started with the channel layer first, squeezing my two part resin compound (layer 3) between acrylic plexiglas block and the layer 4 plexiglas channel structure.

The seismic reflection method is sensitive to impedance variations, which correspond to velocity and density contrasts in between different layers. The black epoxy resin channel has a P-wave velocity contrast of about 20 percent, an S-wave velocity contrast of about 56 percent, and density contrast of 68 percent with the plexiglas (Table 2.1).

Black Epoxy Resin		
Property	**Stycast 2741LV**	**Catalyst 15LV**
Chemical Type	Epoxy	Amin
Appearance	Black	Black
Density	N/A	N/A
Mix Ratio	1	1
Mix Density	1.10 g/cc.	
Primary Velocity	2162 m/sec.	
Shear Velocity	784 m/sec.	
Transparent Acrylic		
Property	**Plexiglas**	
Chemical Type	Acrylic - PMMA	
Appearance	Transparent	
Density	1.18 g/cc.	
Primary Velocity	2604 m/sec.	
Shear Velocity	1784 m/sec.	

Table 2.1. Physical properties of black epoxy resin and plexiglas materials.

Properties of black epoxy resin can be adjusted as it mixes with an auxiliary catalyst (Table 2.2).

Properties of Materials As Supplied	Stycast 2741LV	Catalyst 15LV
Chemical Type	Epoxy	Amin
Appearance	Black	Black
Density	1.58 g/cc.	0.97 g/cc.
Primary Velocity	N/A	N/A
Shear Velocity	N/A	N/A

Properties of Materials As Mixed	Rigid	Semi-Rigid	Flexible
Mix Ratio	4:1	2:1	1:1
Working Life	120 min./100 g.	90 min./100 g.	90 min./100 g.
Density	1.43 g/cc.	1.34 g/cc.	1.23 g/cc.

Table 2.2. Manufacturer specifications of black epoxy resin as it mixes with catalyst.

I mixed enough Stycast 2741LV-type black epoxy resin with Catalyst 15LV with the weight ratio of 1:1 in room temperature to fill the channels. I poured the mixed resin into channels and made the epoxy surface even with a spatula in order to avoid overfilling the very thin channel layers (Figure 2.3.a). It usually takes less than half a day for the resin to solidify. After making sure that epoxy is dried completely, I used a commercial leg wax to bind the top plexiglas block (Figure 2.3.b) with the bottom channel structure, then to minimize air bubbles in the suture, employed extra pressure from top and bottom of the single model using a metal clamp. Next, I placed this new 40 * 40 * 5.2 cm^3 structure consisting of layers 2, 3, and 4 into my metal mold in an upside down position in order to start building the bottom black epoxy resin layer. I made the metal mold larger than the plexiglas model's width and length in order to seal the plexiglas model inside the larger

black epoxy resin to prevent possible water leakage into the plexiglas model during the marine acquisition.

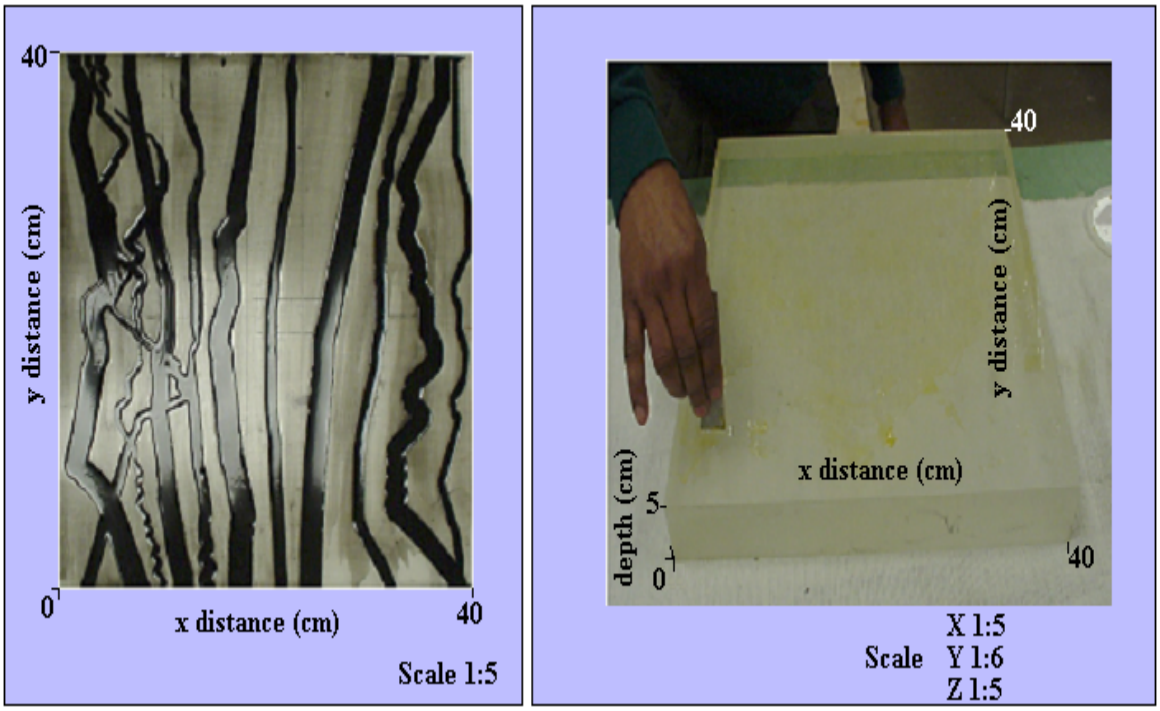

(a) (b)

FIG. 2.3. (a) Layers 3 and 4 acrylic plexiglas channels filled with black epoxy resin. (b) Bottom of layer 2, 5 cm thick plexiglas layer surface covered with cohesive commercial leg wax.

I again used the same weight ratio of 1:1 for mixing Stycast 2741LV-type black epoxy resin with Catalyst 15LV. But this time, instead of immediately pouring this mixture into the metal mold, because of the relatively large amount compared to the amount used for filling the channels, I placed this solution in a vacuum and mixed it about 5 to 10 minutes

before the resin starts to solidify. This operation is mandatory in order to eliminate air bubbles, which can significantly attenuate the wavefield. Black epoxy resin is a very cohesive material that sticks easily on metal after solidification. Since the metal mold should be removed from the model at the end of building process, I applied a very thin layer of lubricant on the bottom and sides of the metal mold before pouring the resin mixture onto the plexiglas and metal mold. Then, I poured the resin close and uniformly onto the plexiglas model and bottom surface of the mold in order to prevent air bubbles. Epoxy resin exhibits an exothermic reaction and its solidification process in room temperature takes days or even weeks according to its thickness. I used approximately 4000 grams of resin mixture for a 2 cm thick layer; it took about 3 days for the resin to completely solidify. Next, I removed the layer 2-5 structure from the metal mold, and turned it right side up. Then, I prepared the top epoxy resin mixture by mixing 5000 grams of Stycast 2741LV-type black epoxy resin with 5000 grams of Catalyst 15LV to produce a 5 cm thick layer 1. I employed the same construction technique as I applied to layer 5 while preparing and pouring top resin mixture. Figure 2.4 shows the entire model after the top black epoxy resin completely solidified and the model is removed from metal mold and weights around 40 kg.

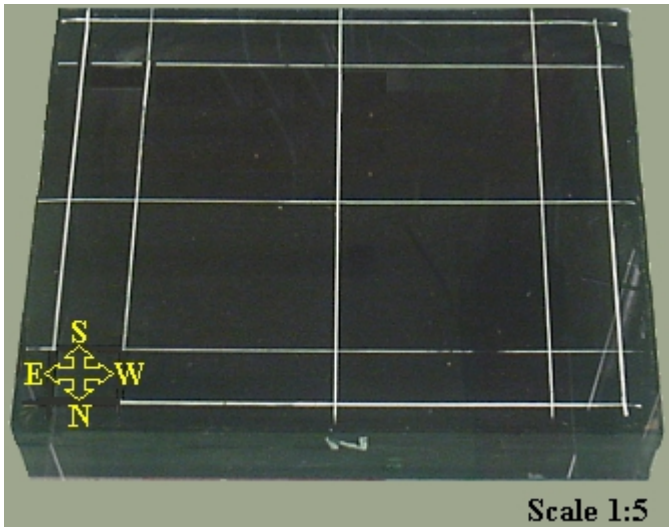

FIG. 2.4. Physical model after addition of layers 1 and 5.

2.2 Acquisition Geometry

As the name implies, the acquisition program has a direct impact on acquisition footprint on the final migrated three-dimensional volume. In the real world, due to feathering of long marine cables, irregular sampling of azimuths, offsets, and folds, acquisition footprint may significantly complicate the interpretation of seismic volumes. Testing different survey designs to minimize these artifacts during the acquisition phase may be quite effective, but it requires enormous capital resources and time. On the other hand, a specific method that reduces footprint for one survey may not help in a different geologic terrain. For instance, the cross-shooting methodology in multistreamer marine survey, introduced by La Bella and Loinger (1998), is quite effective for one of a kind design on suppression of acquisition footprint during the survey phase. However, cross shooting may not help when using different acquisition techniques such as OBC or VC.

Physical modeling can be an economic, useful tool to assess the impact of acquisition footprint for alternative survey designs. VC, OBC, multi and single streamer surveys may all be simulated in the water filled physical modeling environment in order to study the impacts of survey design on seismic attribute analysis. However, these studies extend the complication and duration of processing and interpretation of each unique dataset in the limited time available to complete this thesis. I therefore designed a single survey to collect data over the physical model I built.

Two physical modeling systems, elastic and acoustic are operational at the AGL facility. The 4 * 2 * 1.75 meter acoustic water tank and computer supported acquisition system yield full control over any physical model experiments. I simulated regularly separated 4 streamer marine acquisition using Panametrics HTI-96-300 spherical transducers as both source and receivers whose radiation characteristics are described in Appendix (B). The advantage of simulating multistreamer marine survey in the physical modeling facility is that sources and receivers can be distributed arbitrarily within the water layer. This distribution provides adequately sampled subsurface bins in terms of azimuths, offsets and fold to avoid spatial aliasing that increases the chance of seeing footprint on the processed seismic section. Therefore, holding one of the sources of acquisition footprint under control, I can investigate other possible sources.

The data were acquired in the AGL during the first quarter of 2002 by using computer program called SAM [Seismic Acquisition Manager] written in 1990s subject to 1990

computer and controller technology limitations. This older technology yields 1 trace every two seconds due to time needed for data transfer, transducer movement, and writing to tape. Given these time constraints and the 2 month closure of our lab due to Tropical Storm Allison, I only collected 20 lines of single azimuth 3-D data separated by 25 m, giving a crossline coverage of 475 m. Each line has 838 CDP gathers with the maximum fold of 140 separated by 7.5 m apart from each other. As a result of 280 source-receiver offset, Δh = 7.5 m, CDPs resulted in a total of 1,568,000 traces. In this physical modeling experiment, the nearest source-receiver separation will be 236 m on the closest streamer, and 425 m on the farthest streamer due to the size of transducers Figures 2.5, 2.6, and 2.7 shows the acquisition survey described above.

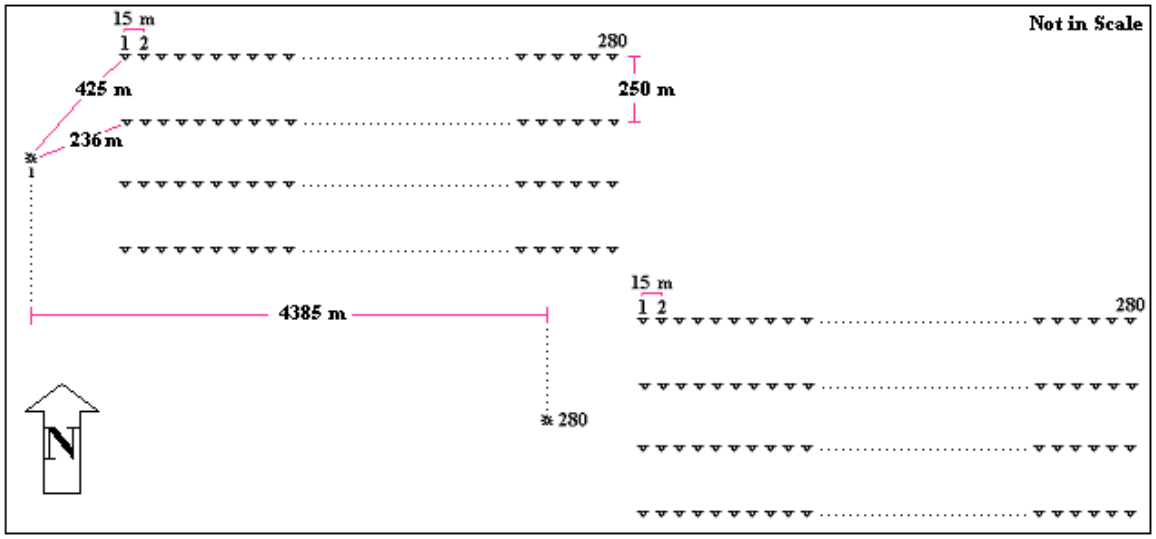

FIG.2.5. 2-D Map view of four-streamer marine acquisition along the model surface that is repeated 5 times to establish 20 lines.

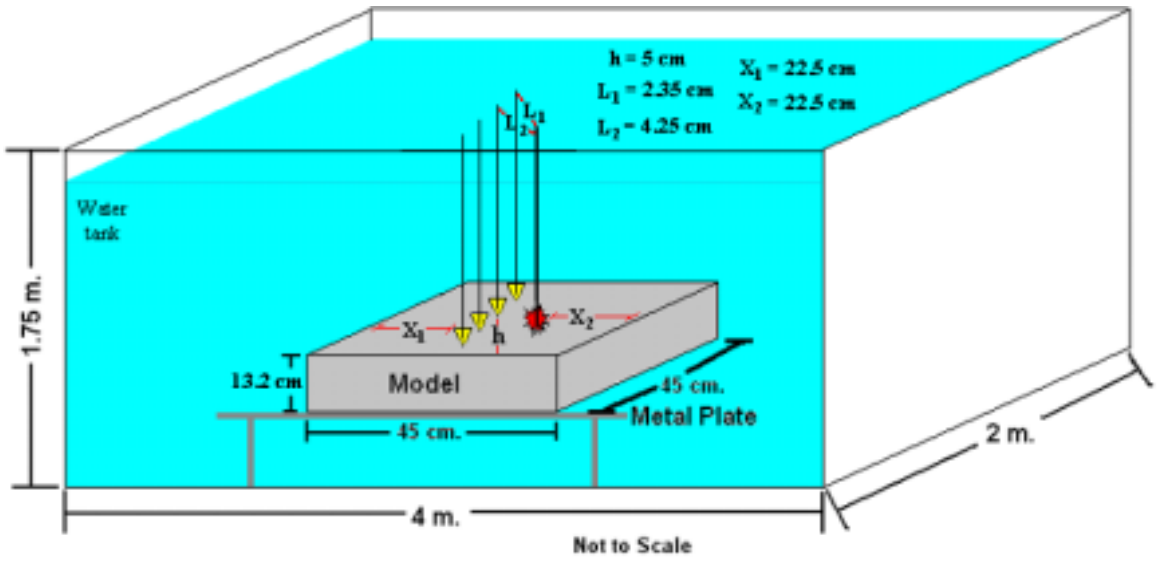

FIG.2.6. 3-D view of source-receiver locations. Note that the initial source location, X_2, is 22.5 cm from the right side of the model, the nearest streamer, L_1, is 2.35 cm farthest streamer, L_2, is 4.35 cm away from the initial source location.

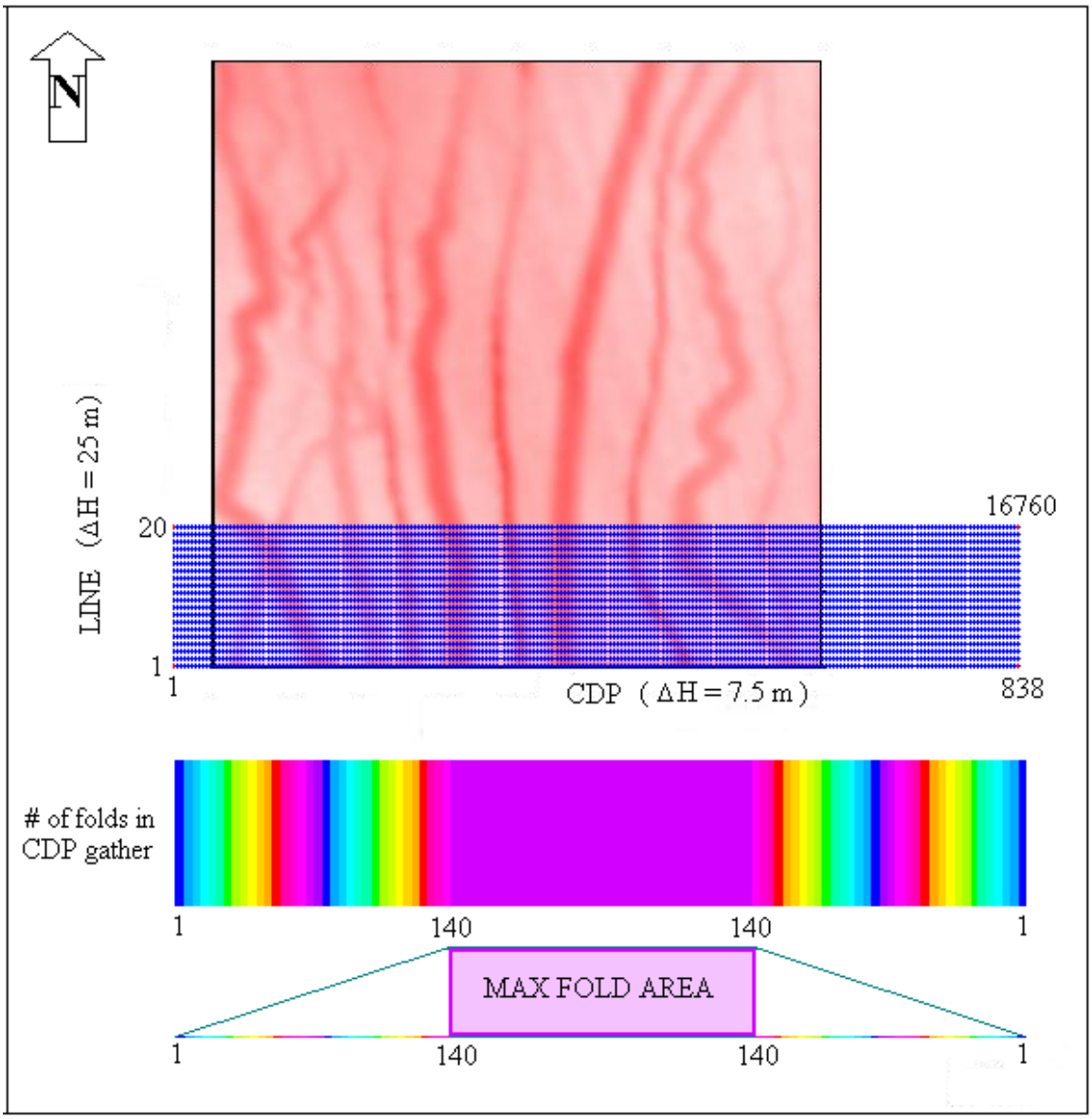

FIG.2.7. CDP coverage over the channel model, indicated by blue dots, with the maximum of 140 fold.

Chapter 3

FOUR STREAMER MARINE DATA PROCESSING

3.1 Introduction

I placed my model in our water tank and acquired four-streamer P-wave seismic data over the physical model shown in Figure 2.4. My model data suffer from both coherent and incoherent noise that severely reduce the signal-to-noise ratio. Incoherent noise sources include electrical and mechanical devices including generators, air conditioners, elevators, fluorescent lights, and the recording system itself. On the other hand, high amplitude source generated coherent noise includes direct, surface, and scattered waves that can easily mask lower amplitude reflection in seismic records. For instance, Drummond *et. al.* (2001) show that such coherent noise is the major cause of acquisition footprint in Berkine Basin, Algeria. In this chapter, I will discuss both theoretical and practical aspects of my processing flow (Figure 3.1.1) to reduce both coherent and incoherent noise required to image my thin channel target.

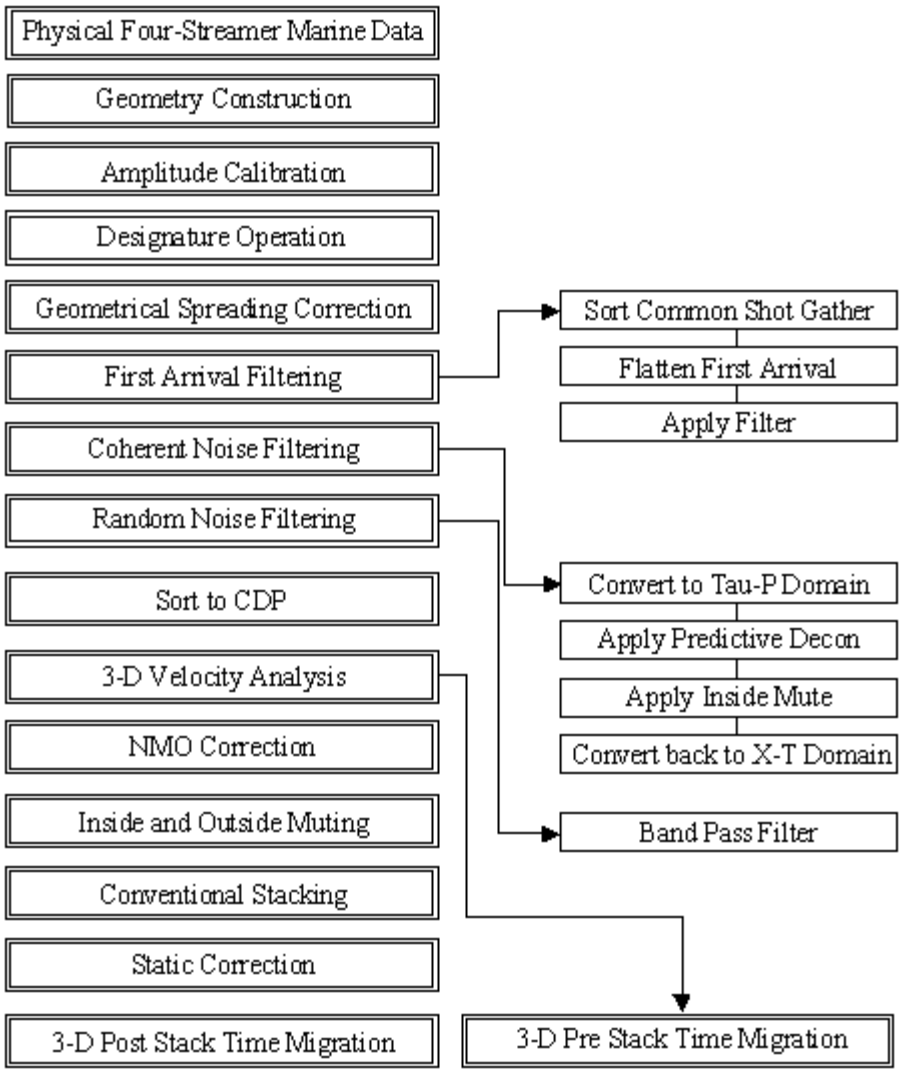

FIG. 3.1.1. Processing flow for P-Component four streamer marine data.

3.2 Geometry Construction

The physical model four-streamer marine data were recorded on digital tape in standard SEGY format. Our seismic recording system allows us to use a maximum of four physical recording channels at one time for each shot. In order to simulate four-streamer marine survey with 280 channels in each streamer, I simply kept my source transducer stationary and moved the four recording transducers an increment corresponding to 25 m and repeated the experiment. In a water tank, the piezoelectric transducer sources have perfectly repeatable coupling and wavelet characteristics. The seismic traces are recorded on tape in the order they were collected (Figure 3.2.1.a). Therefore, I first sorted the data into common recording gathers with group number faster than streamer number (Figure 3.2.1.b) and then renumbered them into separate streamer gathers (Figure 3.2.1.c) to facilitate subsequent filtering.

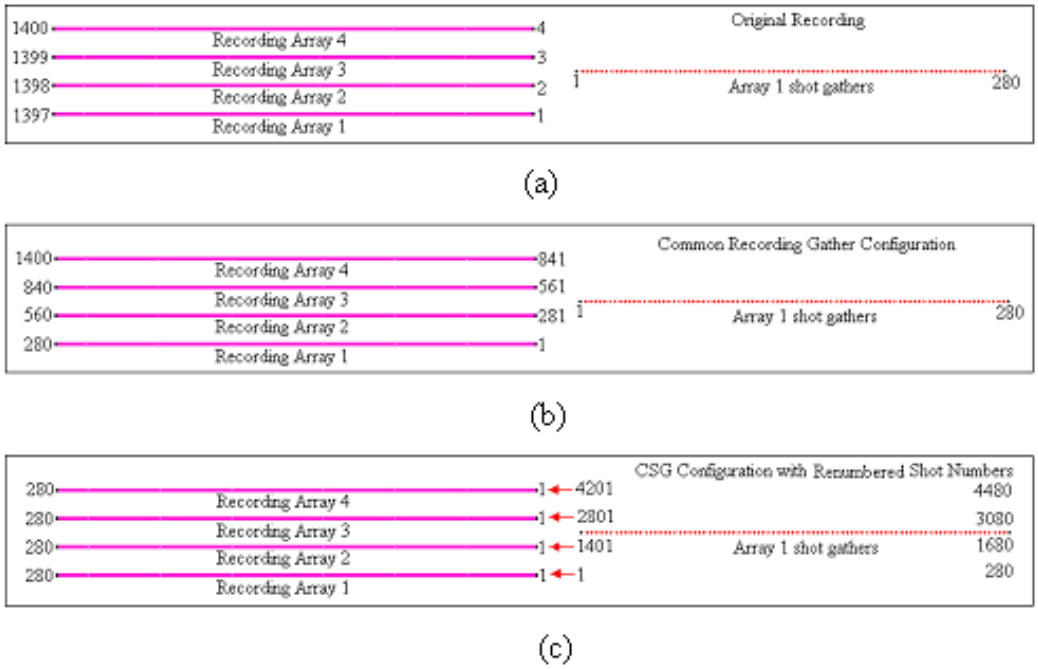

FIG. 3.2.1. Trace ordering after (a) Original recording, (b) Sorting common receiver gathers, and (c) Renumbering into separate streamer gathers.

3.3 Amplitude Calibration

The radiation field of our Panametrics HTI-96-300 spherical transducers varies with incident angle (see Appendix B). Amplitude versus offset (AVO) analyses necessary for hydrocarbon reservoir prediction, time lapse, thin bed evaluation, and so forth that are based on observing amplitude variations need to be corrected for the surface ghost and source array radiation pattern. Although AVO is not a primary concern of this study, I felt that calibrating amplitudes in our physical model data by using the measured transducer directivity function (see Appendix B, Figure B.2.2) would be beneficial for further studies. Therefore, I calculated the necessary emergence angle for transducer

directivity correction by building a simple v(z) model and calculated emergence angles using software provided by GX Technology (Figure 3.3.1).

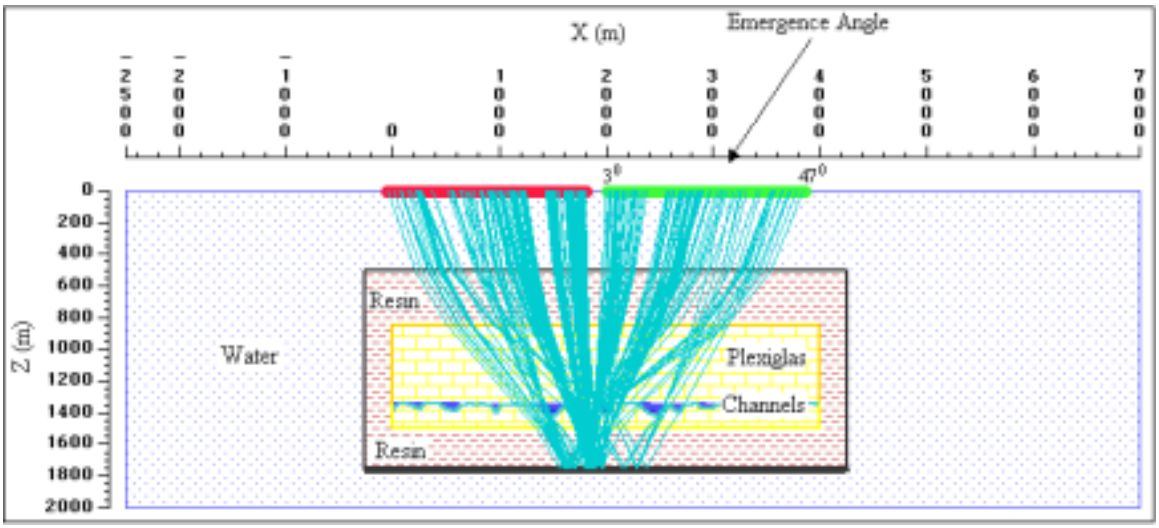

FIG.3.3.1. 2-D ray tracing model of the plexiglas reflection to predict the emergence angle used in transducer calibration.

After calculating the corresponding emergence angles for this model, I calculated the trace envelope of the physical model data. Next, I extracted the envelope value of the reflection signal from channel plexiglas layer. Finally each amplitude value from near to far offset were scaled by the values of the transducer directivity curve shown in Figure 3.3.2.

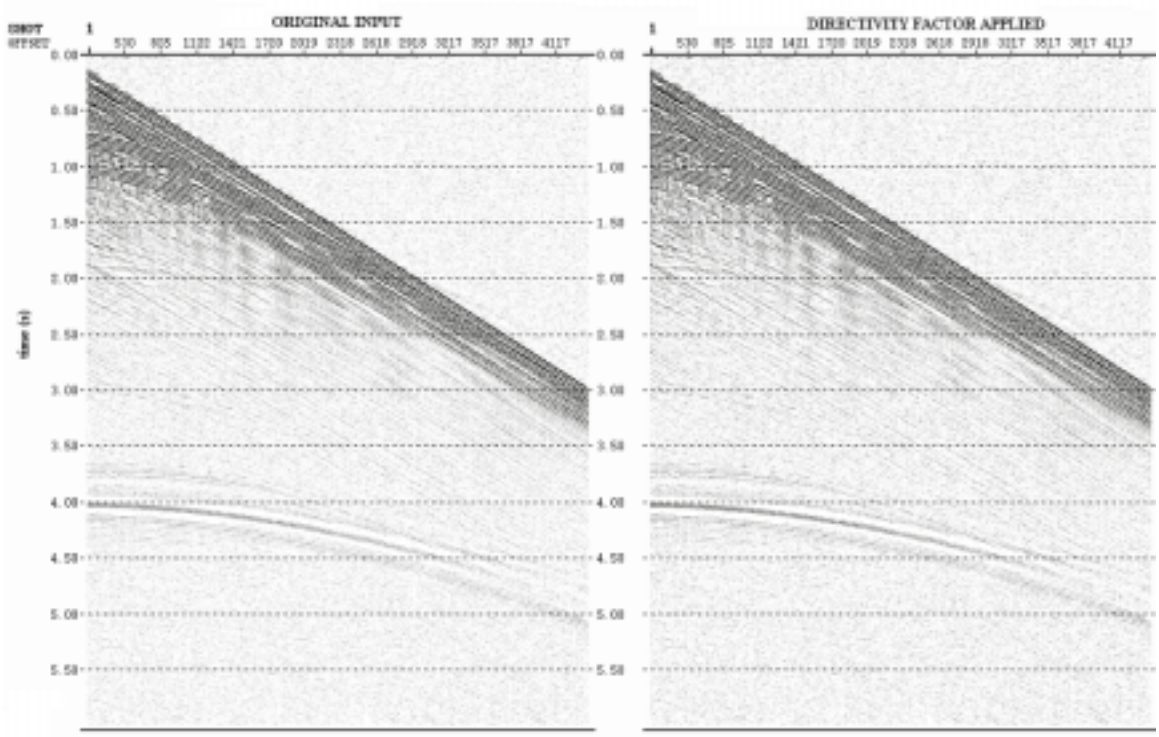

(a) (b)

FIG.3.3.2. Common shot gather record of (a) Original physical model data, and (b) Transducer directivity corrected physical model data.

3.4 Designature Operation

The seismic model data x(t) is composed of the earth impulse response g(t), the far field source signature s(t), and noise n(t) :

$$x(t) = g(t) * w(t) + n(t) , \qquad (3.4.1)$$

where the asterisk * denotes the convolution operator. One objective of data processing is to remove the source signature from the data in order to recover the earth impulse response, g(t), from the measured data, x(t). To accomplish this work, three conditions should be well established (Ziolkowski and Stoffa, 1983): (1) The Signal to Noise ratio |s (t) * g (t)| / |n (t)| must be large; (2) The frequency bandwidth of the generated far field signature s(t) must be broad; and (3) The shape of the far-field signature s(t) must be known. When these three requirements are met successfully, a deterministic deconvolution operator can be applied to the data.

As I mentioned earlier, my physical model data has a low signal-to-noise ratio due to the high ambient noise sources in the basement of a 6 story building. Wardhana (2001), showed how this random noise can be controlled and reduced by stacking the data vertically. Unfortunately, Wardhana's system is not a productive system at the time of this thesis. Our Panametrics HTI-96-300 spherical transducers are operated at a resonance frequency of 350 kHz (which scales in world coordinates to 35 Hz) and exhibit a ringy waveform (Figure 3.4.1.a). This ringy characteristic of spherical transducers definitely is a problem with A-D (analog-digital) converter (Figure 3.4.1.b).

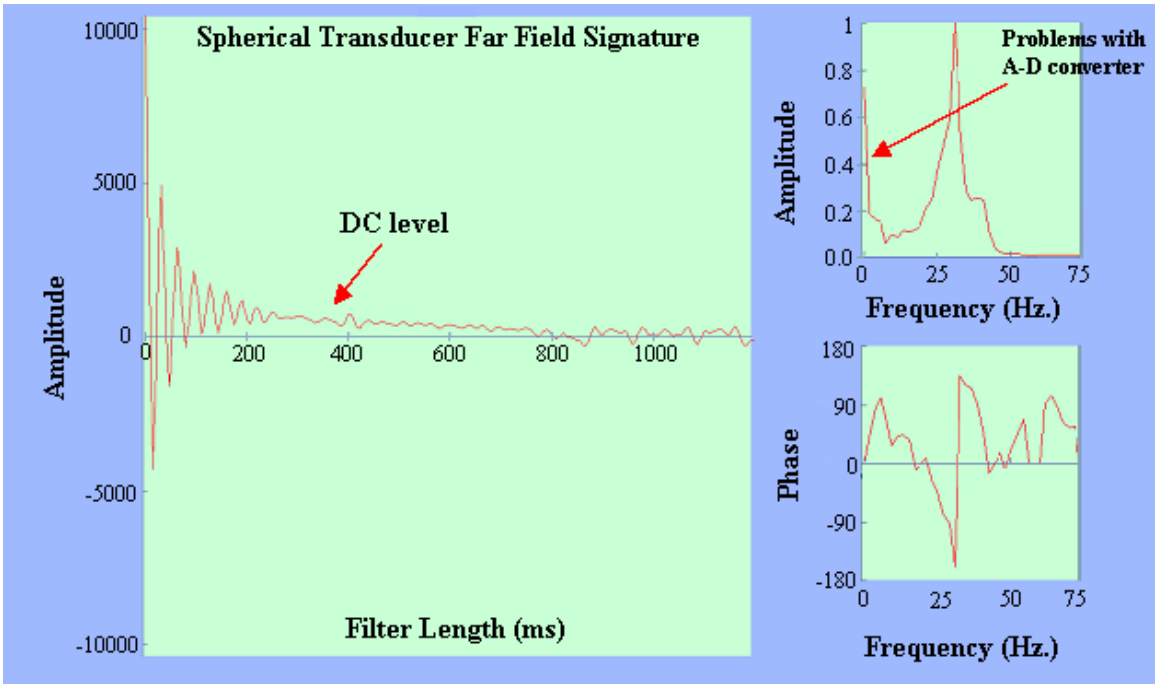

(a) (b)

FIG. 3.4.1. Spherical transducer far field source signature, (a) zero time wavelet, and (b) amplitude and phase response. Note the DC level in both time and frequency domain, probably due to problems with our amplifier or A-D converter.

This ringy signature changes with angle such that the Panametrics HTI-96-300 spherical transducers do not exhibit the same radiation pattern in all directions due to the imperfect shape of active elements (see Appendix B). Krail and Shin (1990) propose a method developed to compensate for the directivity of transducers in deconvolution to remove the directionality effect of such a source.

3.5 Geometrical Spreading Correction

I used a simple gain function to compensate for spreading:

$$g(t) = \frac{[v(t)]^2 \; t}{[v(0)]^2 \; t(0)} \;, \qquad (3.5.1)$$

where t is the two way travel time, v(t) is the rms velocity of the primary reflection, and v(0) is the velocity value at a reference time t(0). I used the rms velocity values, v(t), simply calculated from the interval velocity model (see Figure 3.9.1) and t(0) as 0.5 s. Figure 3.5.1 shows a representative shot gather before and after applying the gain function.

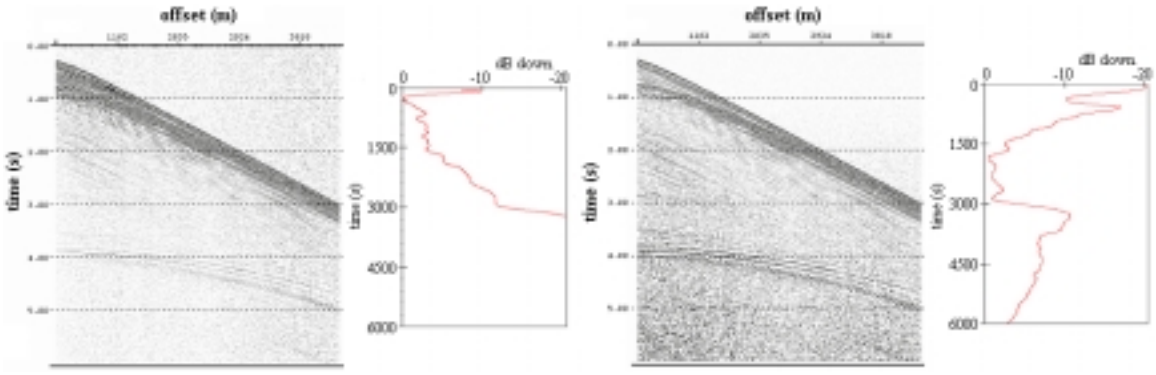

(a) (b)

FIG. 3.5.1. Spherical divergence correction, (a) before, and (b) after.

3.6 Filtering the First Arrival

A source towed streamer seismic survey is simulated in the acoustic model tank by relative movement of source and receiver pairs. The shot is repeated from a stationary source while the receiver is moved away until the desired length of the streamer is simulated. In the absence of both ghost reflections and source and receiver arrays, the strong direct arrival event in our seismic section masks the deeper reflectors of interest. There are several practical techniques to remove the direct arrival from our seismic gathers. Wardhana (2001) simply placed a rubber pad in front of the source to degrade the direct arrival. Unfortunately, this method can be dangerous for long offset surveys where the rubber pad may affect the shape of wavefront at high emergence angles. An alternative approach is to mute the direct arrival during the data processing phase. Unfortunately, the long ringy character of the direct arrival interferes with shallow reflections such that I can not apply muting. Therefore, I used a two step methodology to lessen the effect of the direct. Figure 3.6.1 shows the first step of this process.

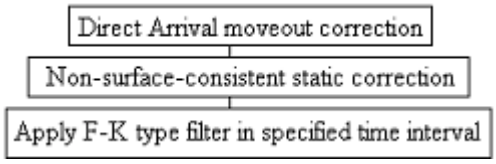

FIG. 3.6.1. Direct arrival suppression flow chart.

Knowing the water velocity, I performed a simple refraction moveout correction to the direct arrival:

$$t_x = t_0 + \frac{X}{V_{water}} \quad , \qquad (3.6.1)$$

where T_x is the two-way travel time at offset X,

T_0 is the intercept time at x=0,

X is the source to receiver offset,

and V_{water} is the water velocity of 1485 m/s.

Small offset changes due to the spherical transducer size and some time fluctuations are observed on moveout corrected direct arrival event (Figure 3.6.2.a). To be able to successfully apply zero dip rejection filter on a specific time interval including this event, I must sharply flatten the direct arrival. To do so, I simply selected a pilot trace on the most flattened area. Then, I crosscorrelated each seismic trace within the ensemble with this pilot trace in order to determine the static correction for each trace. Finally, I applied a static correction by using stored crosscorrelation values (Figure 3.6.2.b).

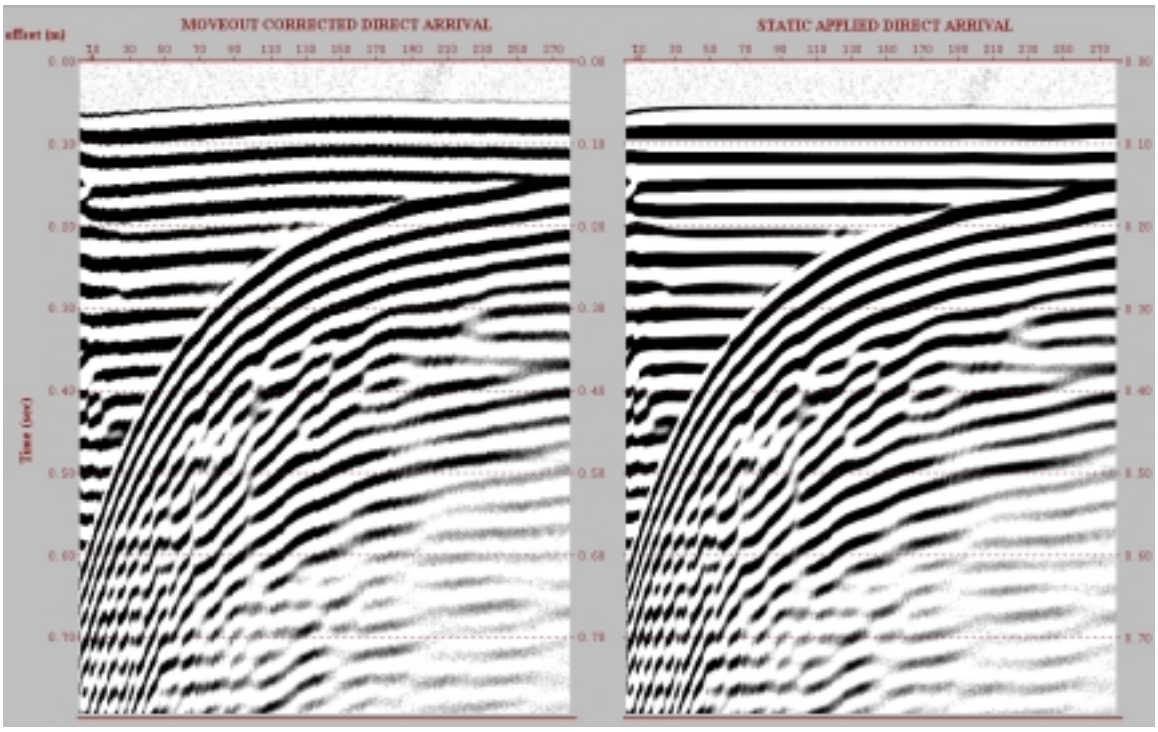

(a) (b)

FIG. 3.6.2. A representative shot gather after (a) moveout using equation (3.6.1), and (b) static applied to moveout corrected direct arrival.

Processing and interpretation of particular events in the time-space domain would be impractical in some conditions. For instance, muting the direct arrival event between 0 and 0.40 s in Figure 3.6.2 may bring harm to our shallow primary reflections. Therefore, it would be more convenient to transform and process the ensembles in other domains. The recorded wave field is a composite of many dip and frequency components (Yilmaz, 1987). In this manner, dipping events in the time-space domain can be represented in terms of their frequency and wavenumber (k) in f-k domain. Zero-dip components such as the corrected direct arrival in our case, will be lined up along k_x=0 in the 2-D Fourier domain where:

$$P(k_x , \omega) = \iint p(x,t) \exp (ik_x x + i\omega t)\, dk_x\, d\omega. \quad , \qquad (3.6.2)$$

where $P(k_x , \omega)$ is the wavefield in the frequency-wavenumber domain

$p(x , t)$ is the wavefield in time-space domain

ω is the angular frequency, $2\pi f$ in radians/s,

k_x is the wavenumber in cycles/m,

x is the offset in meters, and

t is the time.

Muting the k_x=0 component and transforming back to (t,x) I obtain the gather shown in Figure 3.6.3.

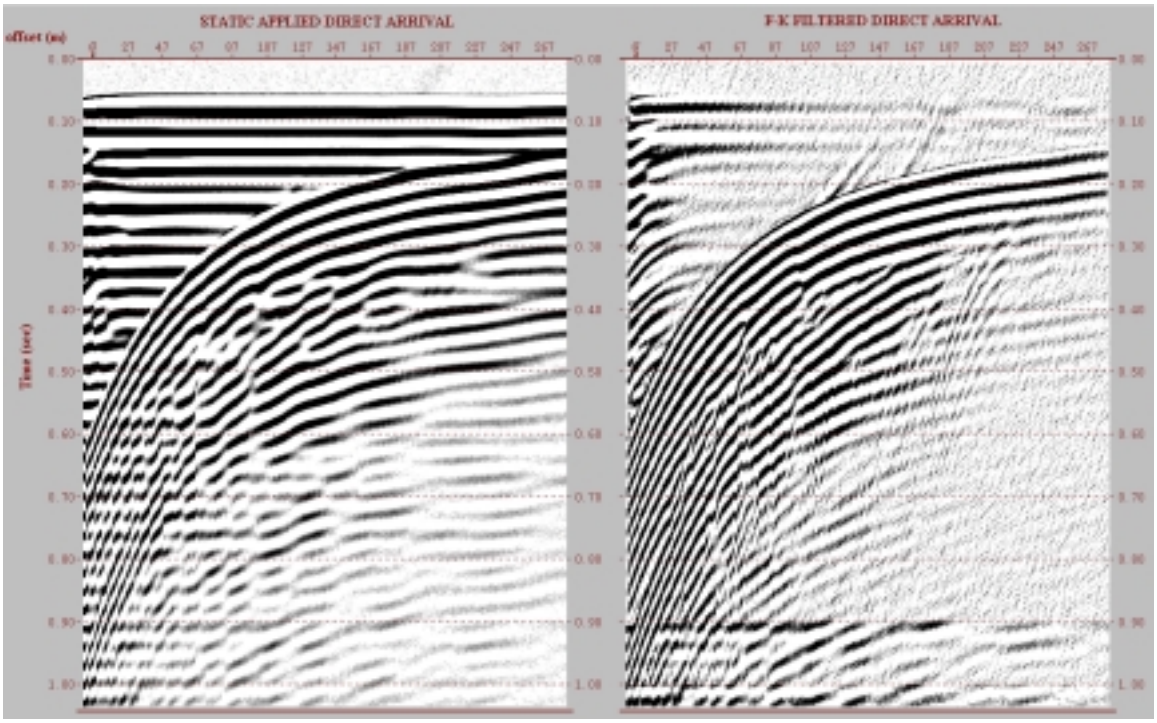

(a) (b)

FIG. 3.6.3 Ensemble, (a) before, and (b) after f-k filtering.

Notice that components of the direct wave still remain on the near offset due to imperfect flattening during static correction (Figure 3.6.2.b). I remove my moveout correction from the data, and then subtract the filtered ensemble (Figure 3.6.4.b) from the original one (Figure 3.6.4.a) to make sure that I have not degraded the signal (Figure 3.6.4.c). Some channel and model edge diffractions start to appear in our seismic section (Figure 3.6.4.b).

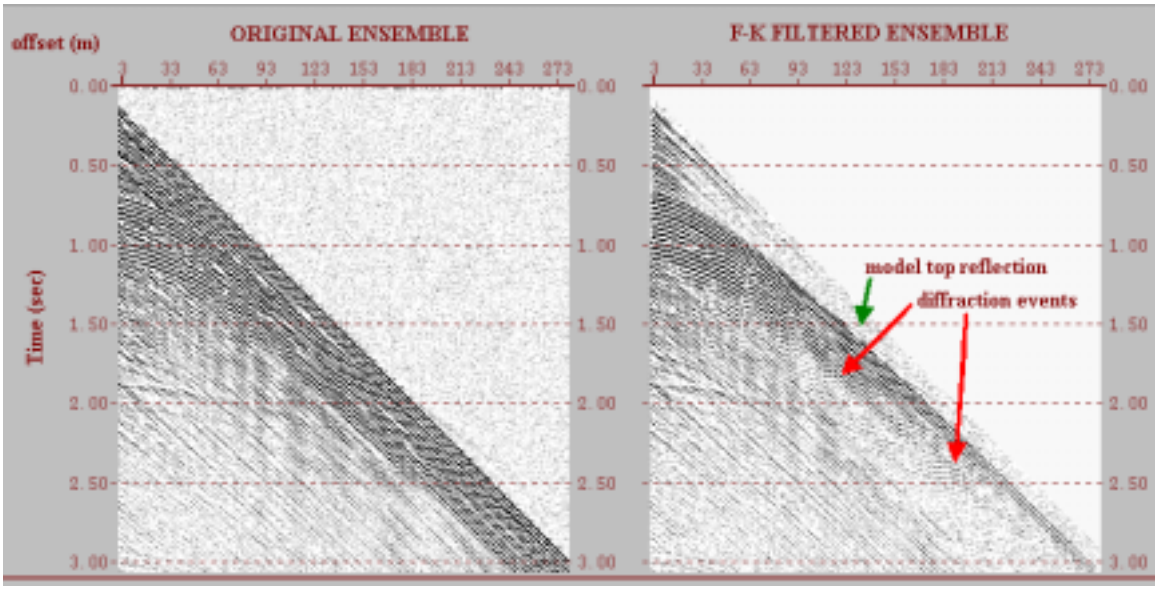

(a) (b)

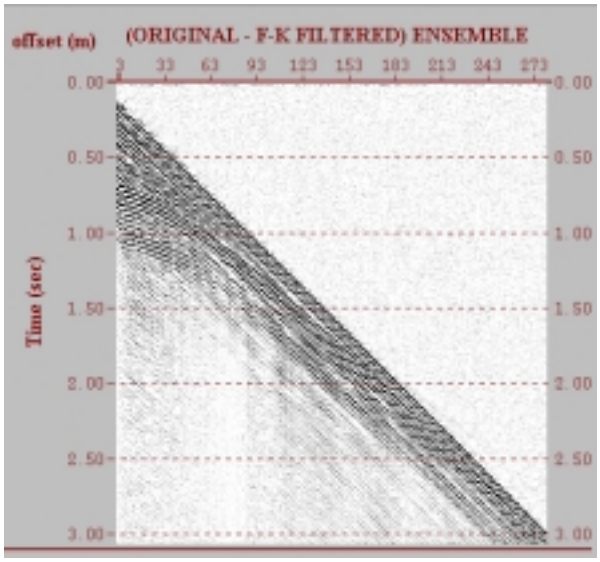

(c)

FIG. 3.6.4. Shot gathers (a) as recorded and, (b) after f-k filtering. (c) difference between (a) and (b) showing the rejected noise.

3.7 Filtering the Coherent Noise

High amplitude source generated noise including direct, surface, and scattered waves can easily mask lower amplitude reflections in seismic records. As mentioned previously, aggressive muting in the time-space domain can lead to the unintentional removal of shallow reflection events. Therefore, a robust method is required to minimize the effects of nonreflected energy. Many methods in the literature deal in part with coherent noise reduction. One of the most sophisticated methods suggests that wavefields can be separated according to their path of propagation and their actual moveout characteristics (Nemeth *et. al.*, 2000). This method is known as the migration filtering technique and accomplished by using forward modeling operators to compute the signal and the coherent noise arrivals. However, selecting proper forward model operators may be difficult most of the time and carries heavy computational costs. One other very popular method of separating reflections from source generated noise is tau-p (τ-p) filtering, where data are transformed into intercept time (τ) and ray parameter (p). Linear τ-p transformation converts linear and hyperbolic events in the t-x (time-space) domain to points and ellipses, respectively (Yilmaz, 1987). I used the flow shown in Figure 3.7.1:

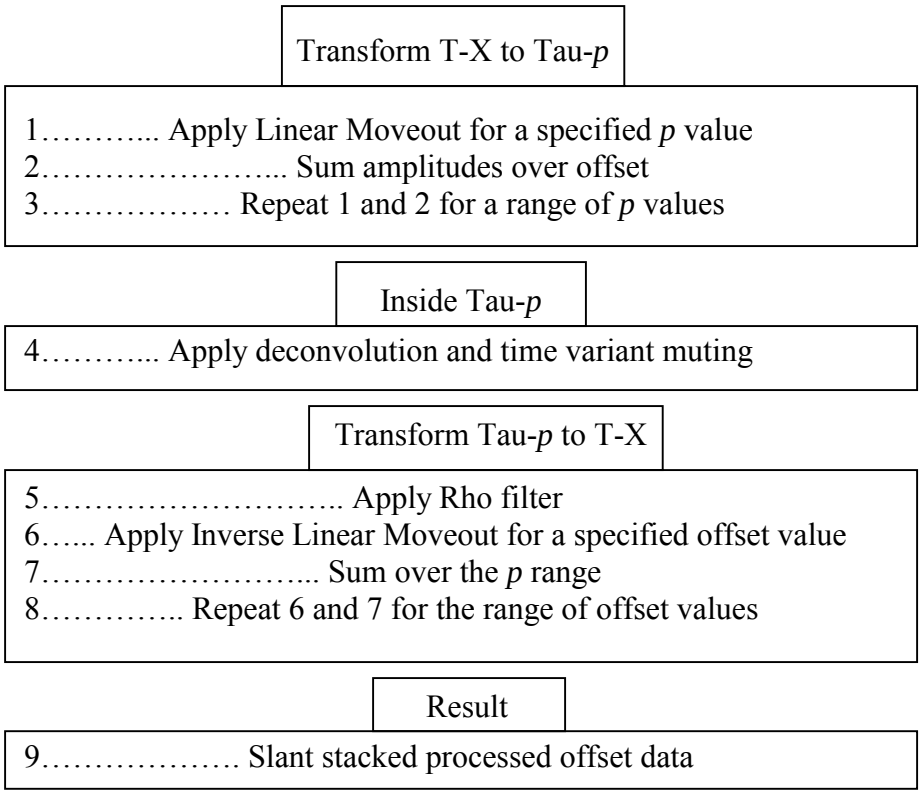

FIG.3.7.1. Slant Stack processing flow.

The reflections in shot gathers are primarily masked with source generated linear noise in our physical model data (Figure 3.7.2.a). To be able to remove these low velocity noise events in τ-p domain, I selected p value ranges between –550 μs/m and 750 μs/m. Note in Figure 3.7.2.b that linear coherent noise events map to slowness greater than that of water = 667 μs/m. Before applying a conventional time variant mute encompassing p-wave reflections, I investigated the deconvolution concept in the τ-p domain.

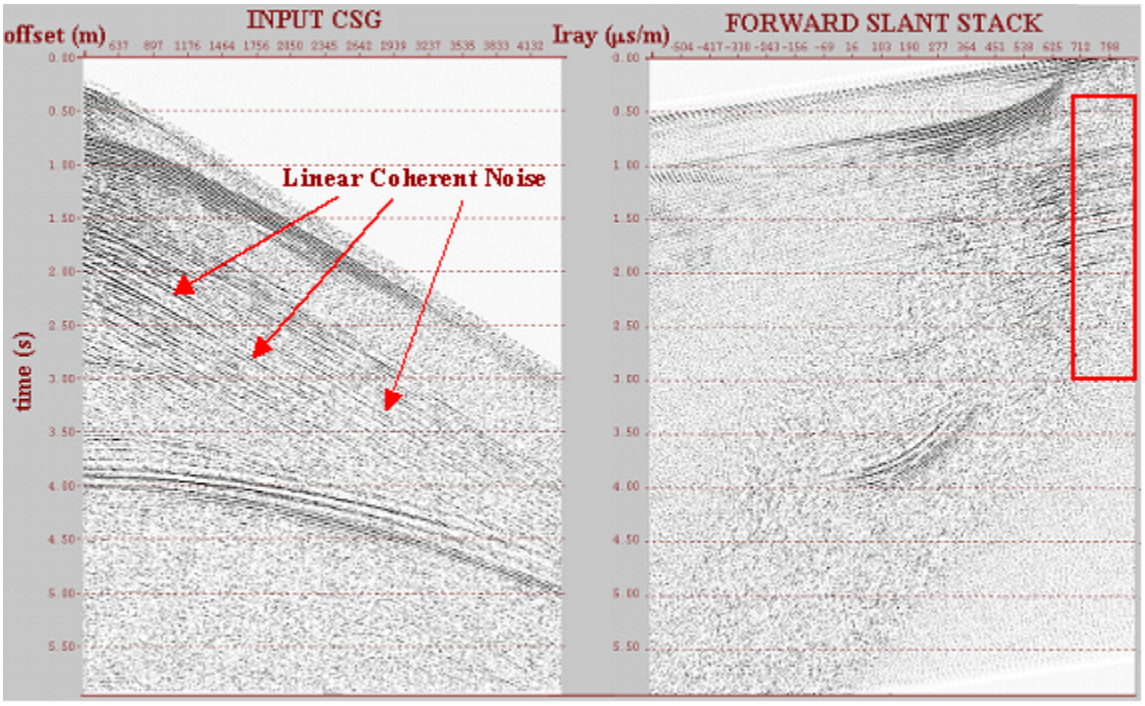

(a) (b)

FIG.3.7.2. Linear coherent noises shown with, (a) red arrows in t-x domain, (b) red rectangle in τ-*p* domain.

Predictive deconvolution in data processing can be used for two distinct purposes: (a) compressing or shaping the seismic wavelet s(t), and (b) predicting and suppressing multiples m(t) (Yilmaz, 1987). In the (x,t) domain, the periodicity of multiples is preserved with only zero degree incidence and zero offset recording. Therefore, multiple prediction and suppression may not be achieved with predictive deconvolution using common shot gather data.

For a flat multiple generator, the multiple periodicity is preserved in the τ-*p* domain for each value of *p*. Since the time separation along the summation path is regular, a predictive deconvolution operator can be designed from the autocorrelogram of each *p* trace in the τ-*p* domain. Unfortunately, geometrical spreading can contaminate the periodicity of multiples; therefore, I must first remove this compensation from common shot gather data before autocorrelation analysis in the τ-*p* domain. After constructing the autocorrelogram for each *p* trace, I selected a 128 ms operator length and prediction lag of 24 ms to be used in predictive deconvolution operation. Figure 3.7.3 and 3.7.4 show the autocorrelograms and data before and after predictive deconvolution. It may be noticed in Figure 3.7.3.b that at first look, there is a slight reduction of periodic events between 0.25 s and 3.0 sec. However, it should be noted that all deconvolution operators assume that recorded seismic data is noise free. This is not the real case most of the time. In fact, my physical model data suffers from high random noise contamination. I do not have strong multiples in my data. However, the wavelet shaping as a function of ray parameter effectively compresses the angle-dependent reverberations generated by my transducers as indicated with red arrows in Figure 3.7.4.b.

After applying predictive deconvolution in the τ-*p* domain, I separate coherent noise from reflection events in the τ-*p* domain by conventional outer muting.

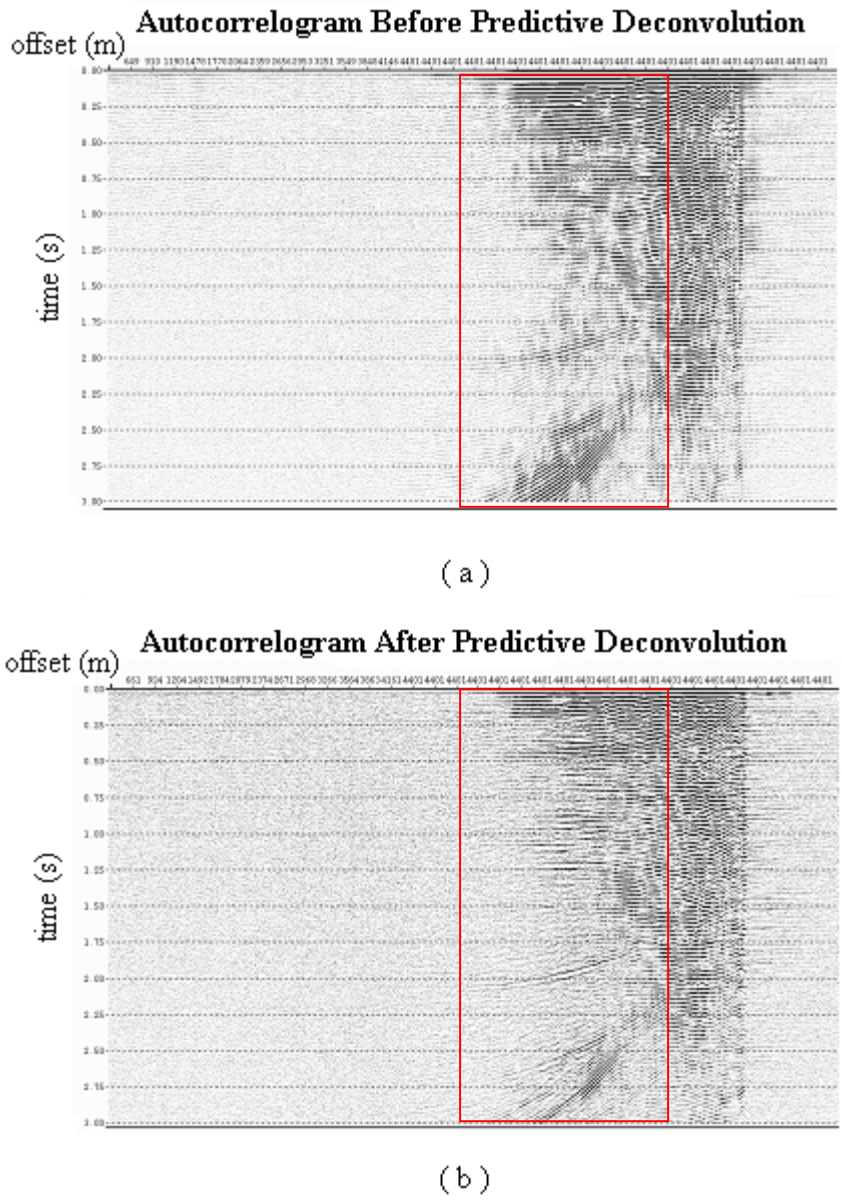

FIG.3.7.3. Autocorrelogram window results indicated in red box, (a) before predictive deconvolution, and (b) after predictive deconvolution.

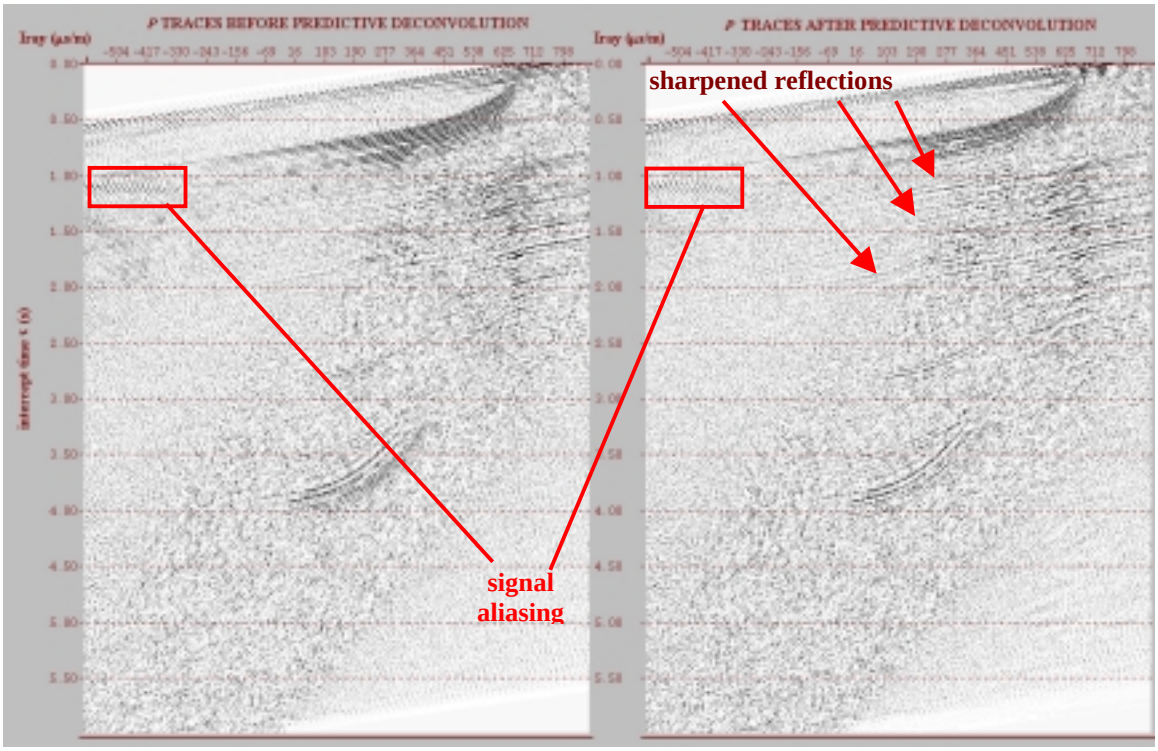

(a) (b)

FIG.3.7.4. Data in the in τ-*p* domain, (a) before predictive deconvolution, and (b) after predictive deconvolution. Red arrows indicate sharpened reflections. The red box indicates signal aliasing.

As indicated in Figure 3.7.2.b, some coherent noise is slower than the water slowness. A time variant outer mute along the water slowness boundary will reject the coherent noise from data. This operation, before and after mute, is shown in Figure 3.7.5 (a) and (b). After successfully filtering the source generated coherent noise in τ-*p* domain, I applied inverse slant stack operation in order to return to the t-x domain where I will perform the rest of the processing flow. The results before and after the slant stack operation are shown in Figure 3.5.6 (a), (b), and (c).

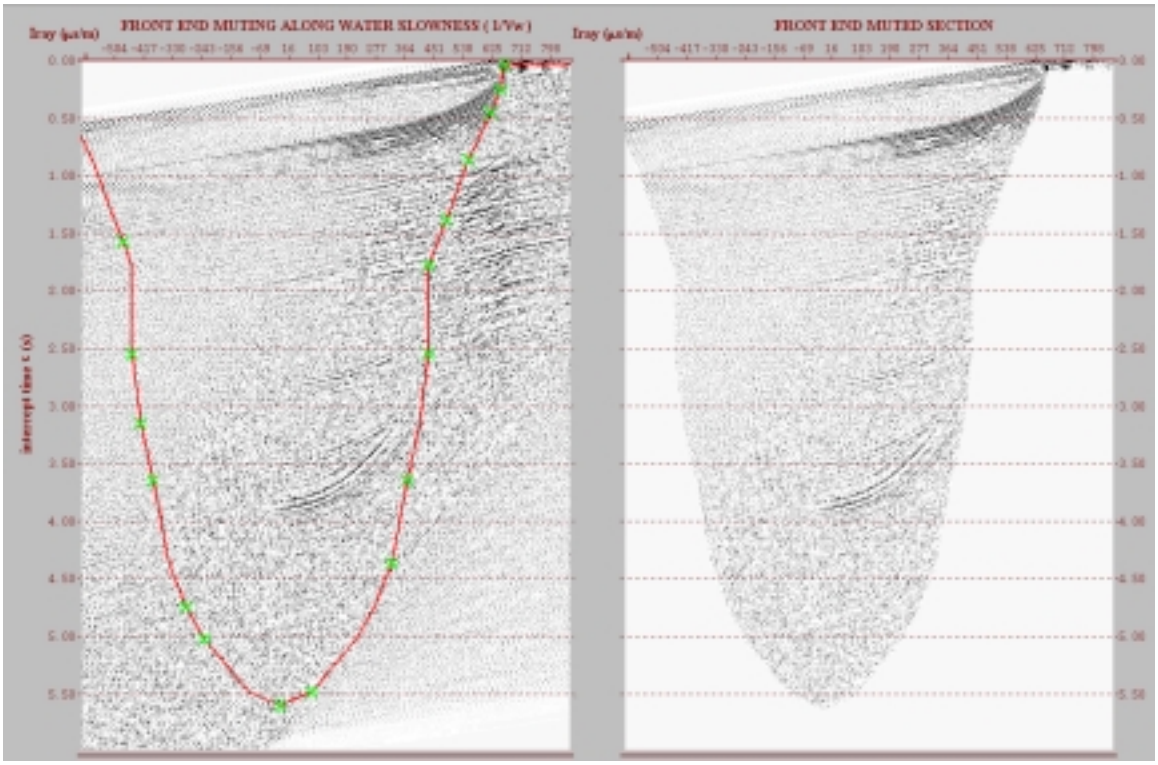

(a) (b)

FIG.3.7.5. Data in the τ-*p* domain, (a) before, and (b) after.

Figure 3.7.6.b shows that diffraction events from channel and model edges are preserved and become sharper after τ-*p* deconvolution and filtering. Figure 3.7.6.c shows rejected events. Notice that the data thrown away from the original input also contains some shallow primary reflection energy. The major cause of this energy loss is due to the nonorthogonality of the forward and inverse τ-*p* transform pair. Nevertheless, areas of interest in the CSGs have been improved.

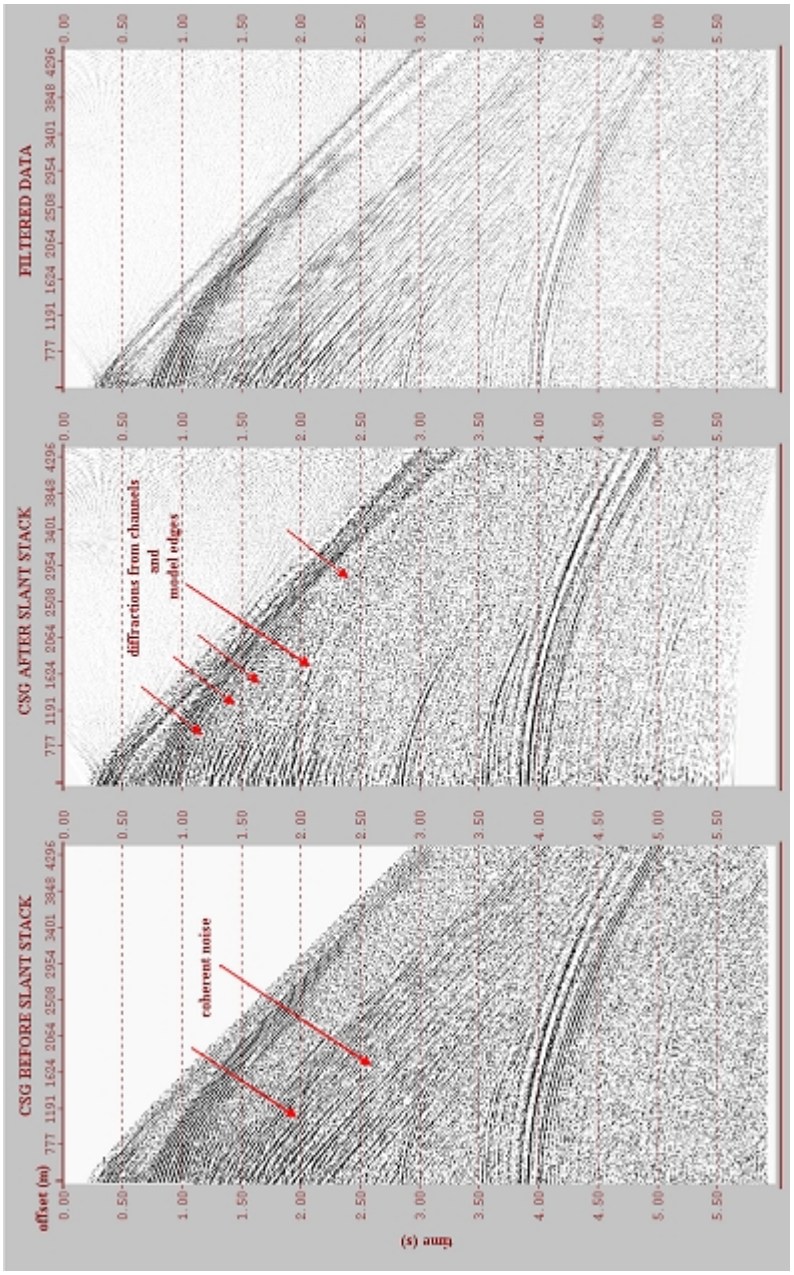

(c)

(b)

(a)

FIG.3.7.6. Common shot gather, (a) of input data, (b) after slant stack processing, and (c) of rejected data. Red arrows indicate events on CSGs.

3.8 Band-Pass Filtering

Inspection of Figure 3.8.2.a shows that significant 'white' noise below 8 Hz and above 68 Hz remain in the data even after multichannel filtering. The low frequency noise comes from a grounding while the high frequency noise comes from electrical instruments in the laboratory. By designing a simple band-pass filtering, I suppressed the noise outside the range of detectable signals (Figure 3.8.2).

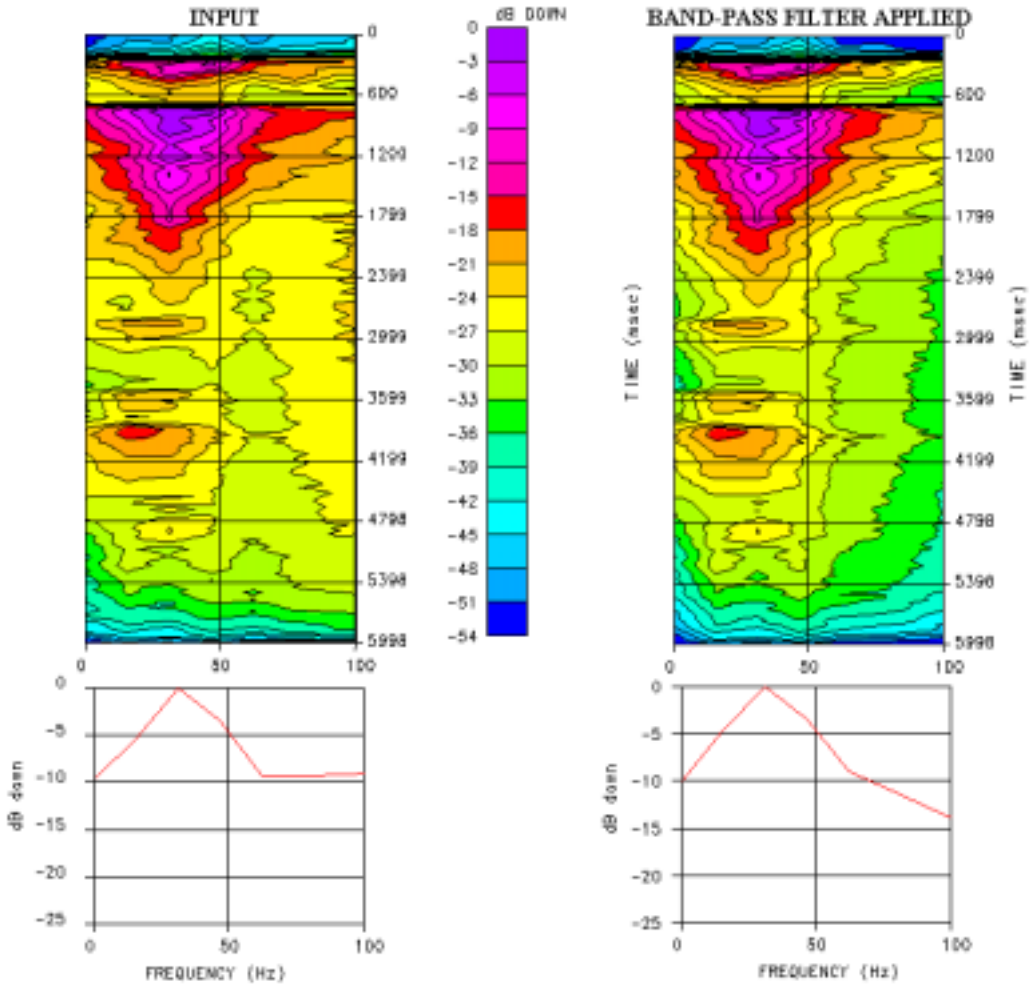

FIG.3.8.1. Spectrum of CSG, (a) before applying 6-8-60-90 Hz filter, and (b) after.

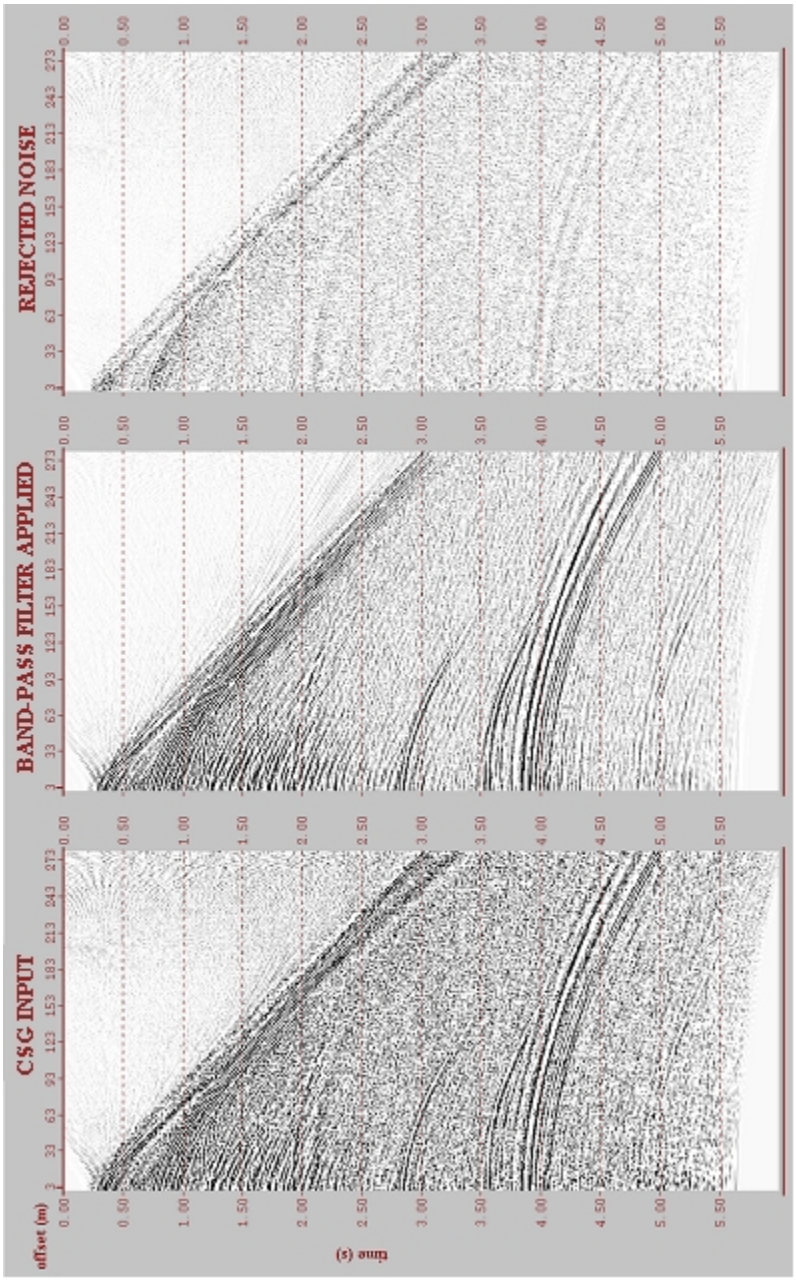

(c)

(b)

(a)

FIG.3.8.2. Common shot gather, (a) before filter applied, (b) after filter applied, and (c) of rejected random noise.

3.9 3-D Velocity Analysis

Proper velocity analysis is critical in order to have confidence in the resulting seismic images (Nelson, 1986). There are four different basic velocity terms available for different purposes: 1. Stacking velocity, 2.Root Mean Square velocity (RMS), 3. Average velocity, and 4. Interval velocity. Normal moveout correction for horizontally stratified model and most migration algorithms use RMS velocity, which in turn can be related to interval velocity and travel times thicknesses. Since this a model study, I calculated the RMS velocity values from the known internal velocities for each CDP locations in the physical model to be used in both NMO correction and 3-D Post and Prestack imaging:

$$V^2_{rms} = \frac{1}{t(0)} \sum_{i=1}^{N} V_i^2 \, \Delta t_i(0) \quad , \quad t(0) = \sum_{i=1}^{N} \Delta t_i \quad , \qquad (3.9.1)$$

where, Δt_i is the vertical two-way travel time through the i^{th} layer

V_{rms} is the RMS velocity

t(0) is the two-way travel vertical travel time to the N^{th} layer.

Figure 3.9.1 shows the RMS velocity model along line 1 of the physical model.

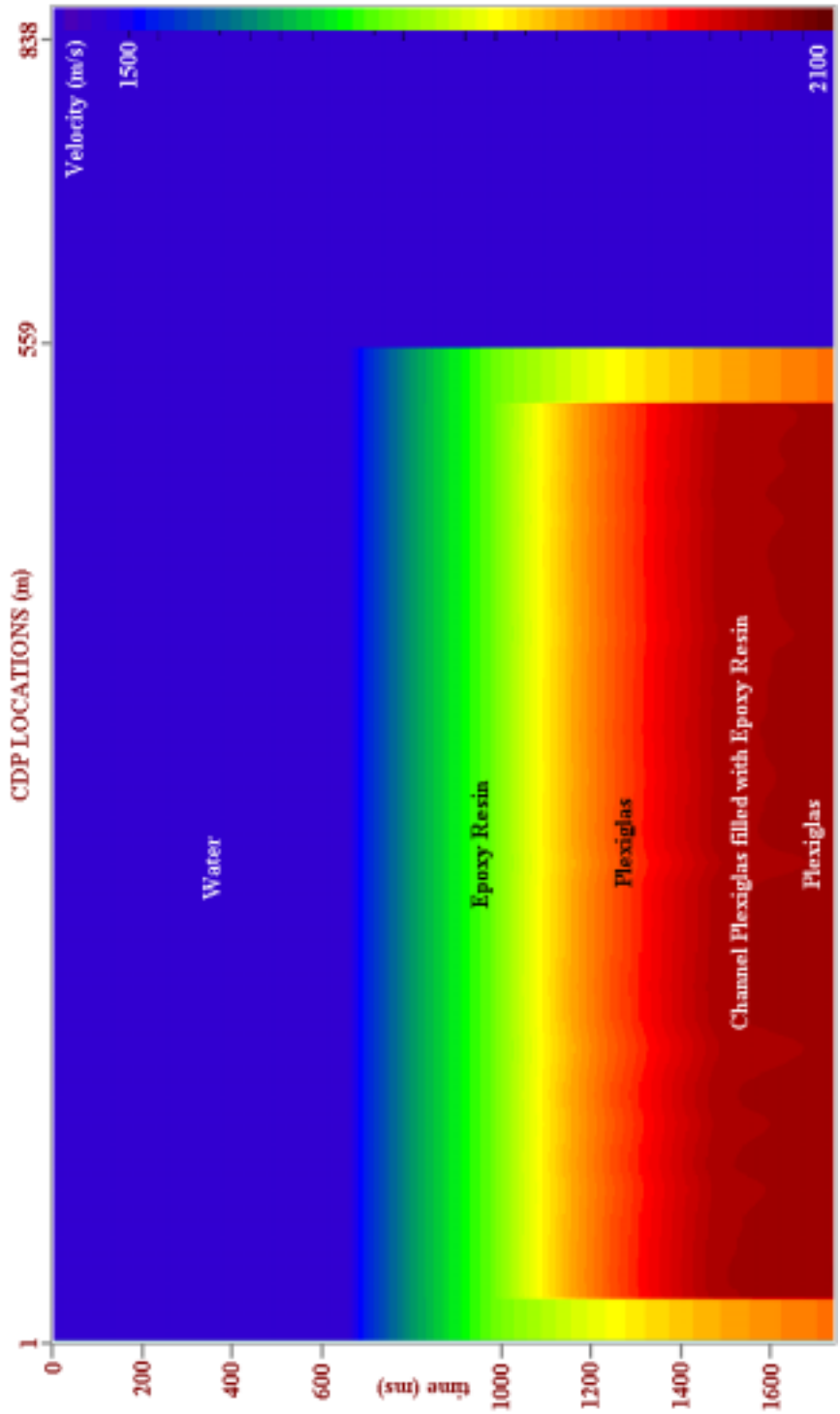

FIG.3.9.1. The RMS velocity model along line 1 of the physical model. This velocity will be used for NMO correction and 3-D migration.

3.10 NMO Analysis and CDP Stacking

NMO (Normal Move Out), which is the difference between two-way travel time at a given source-receiver offset, t(x), and two-way travel time at zero offset, t(0), is performed to flatten seismic reflection events in each CDP gather before they are stacked. Before applying NMO, I sorted the data from CSG to CDP gathers. Figure 3.10.1 shows selected NMO corrected CDP gathers from lines 1, 6, 11, and 16.

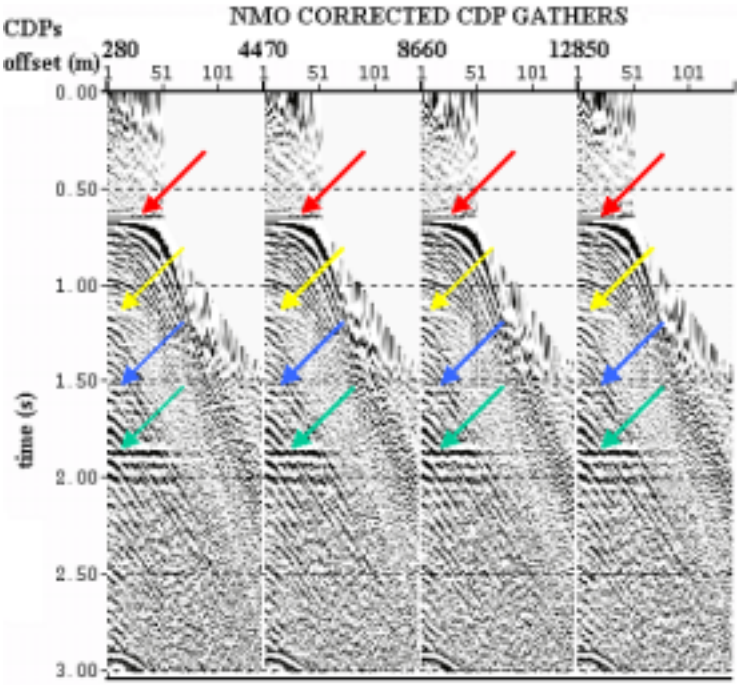

FIG.3.10.1 NMO corrected CDP gathers from lines 1, 6, 11, and 16. The red arrow shows the interface between water layer and layer 1, the yellow arrow exhibits the interface between layer 1 and 2, the blue arrow indicates the interface between layer 2 and 3, and the green arrow shows the interface between layer 4 and 5.

As indicated with the arrows in Figure 3.10.1, primary reflection events from my channel model are flattened while remaining back-scattered coherent noise and converted waves are undercorrected. Frequency distortion occurs at large offsets in the shallow events due to NMO stretch. Before stacking the NMO corrected data, it is recommended to mute these distorted data from gathers. I therefore performed an outer mute operation in all gathers (Figure 3.10.2.a). Furthermore, I also applied a very small window of inner mute to reduce transform artifacts introduced in the τ-*p* transform (Figure 3.10.2.a).

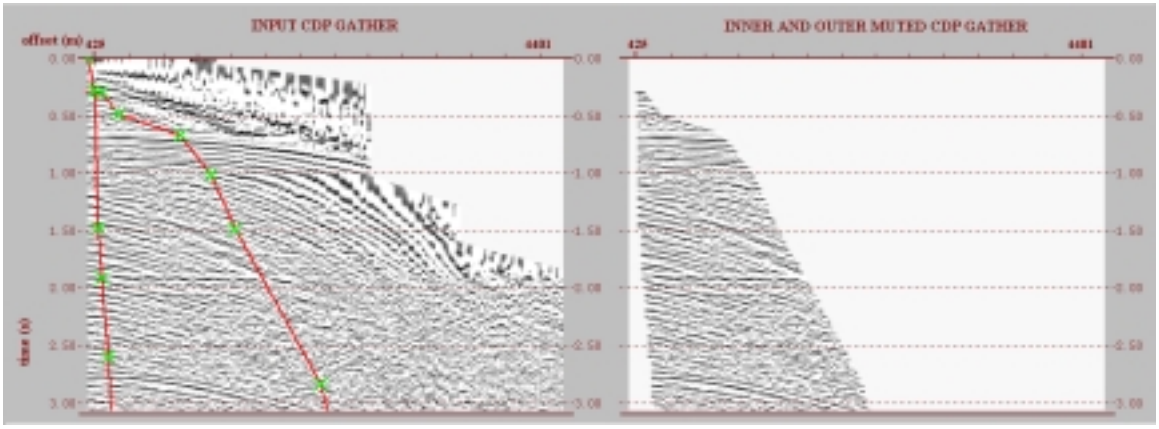

(a) (b)

FIG.3.10.2. A representative CDP gather (a) before mute applied, and (b) after.

After the muting process, I stacked each CDP gathers along the each crossline to perform 3-D post stack time migration later (Figure 3.10.3).

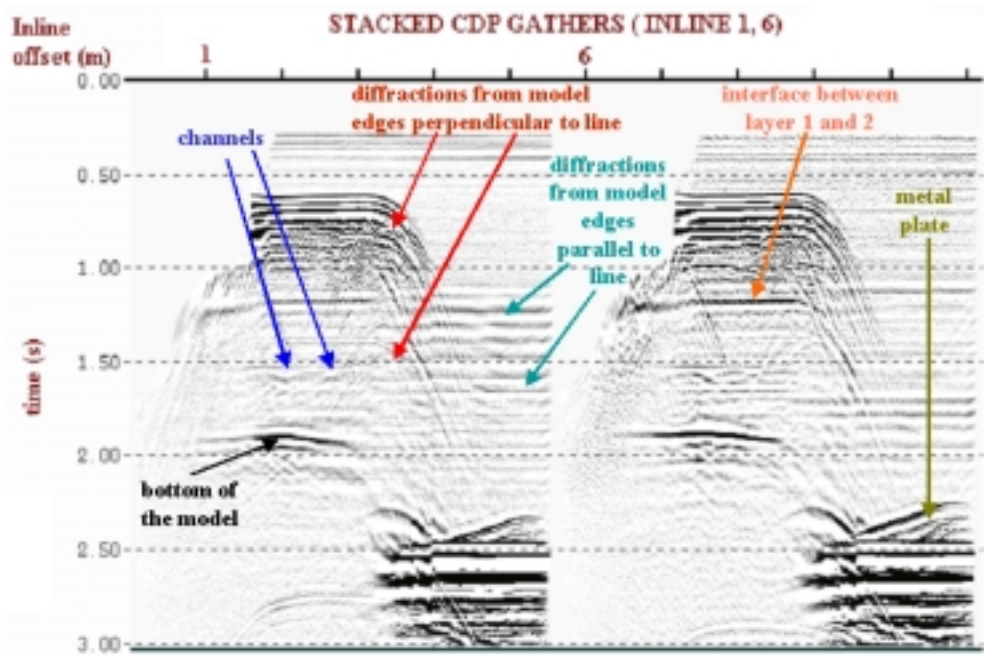

(a)

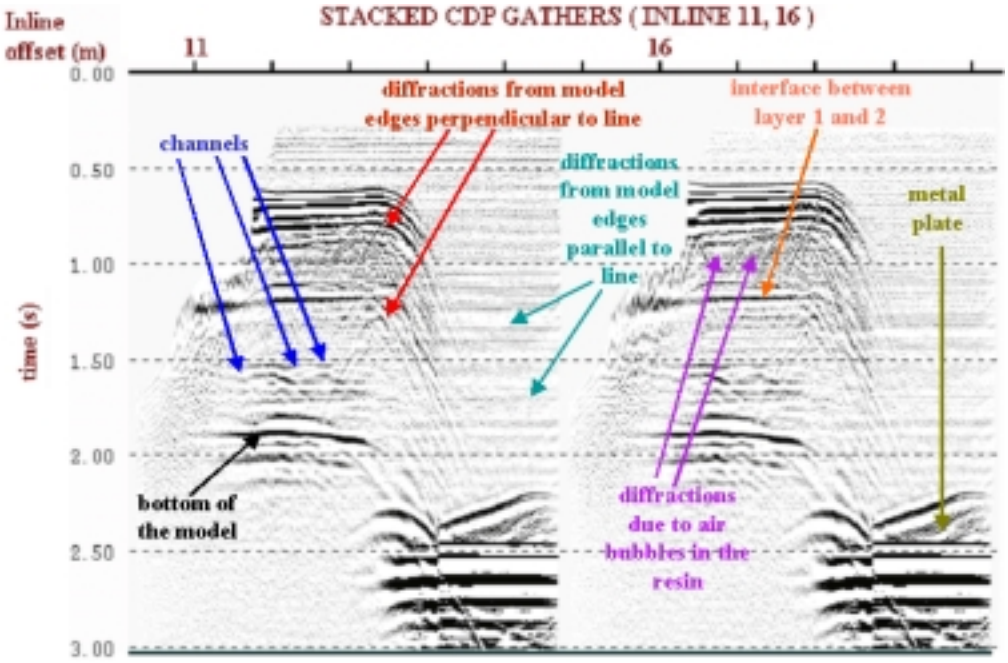

(b)

FIG.3.10.3. Stacked sections from the physical model, (a) lines 1 and 6, and (b) lines 11 and 16.

After careful examination of the stacked sections of lines 1, 6, 11, and 16, I noticed reflection time irregularities in the interface of layer 1 and 2. These errors may not be due to the RMS velocities since the reflections were flattened properly, but improper transducer levels during acquisition. I then looked at flattened events on each inline and analyzed reflection times. For instance, the metal surface reflection times from inline 1, 6, and 11 show no remarkable time shift whereas inline 16 thorough 20 indicate 5 ms upward time shift (Figure 3.10.4). Therefore, I applied 5 ms downward time shift to compensate this error for inlines from 16 to 20 (Figure 3.10.5).

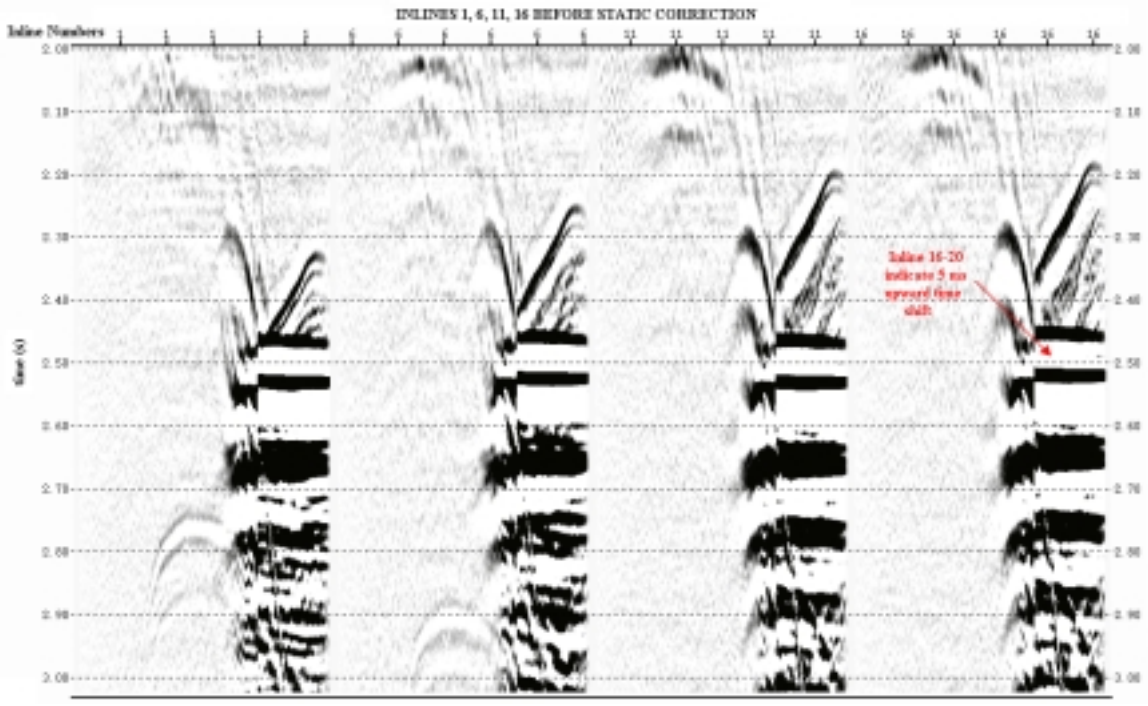

FIG.3.10.4. Observed time shift on metal plate reflections on inline between 1, 6, 11 and 16.

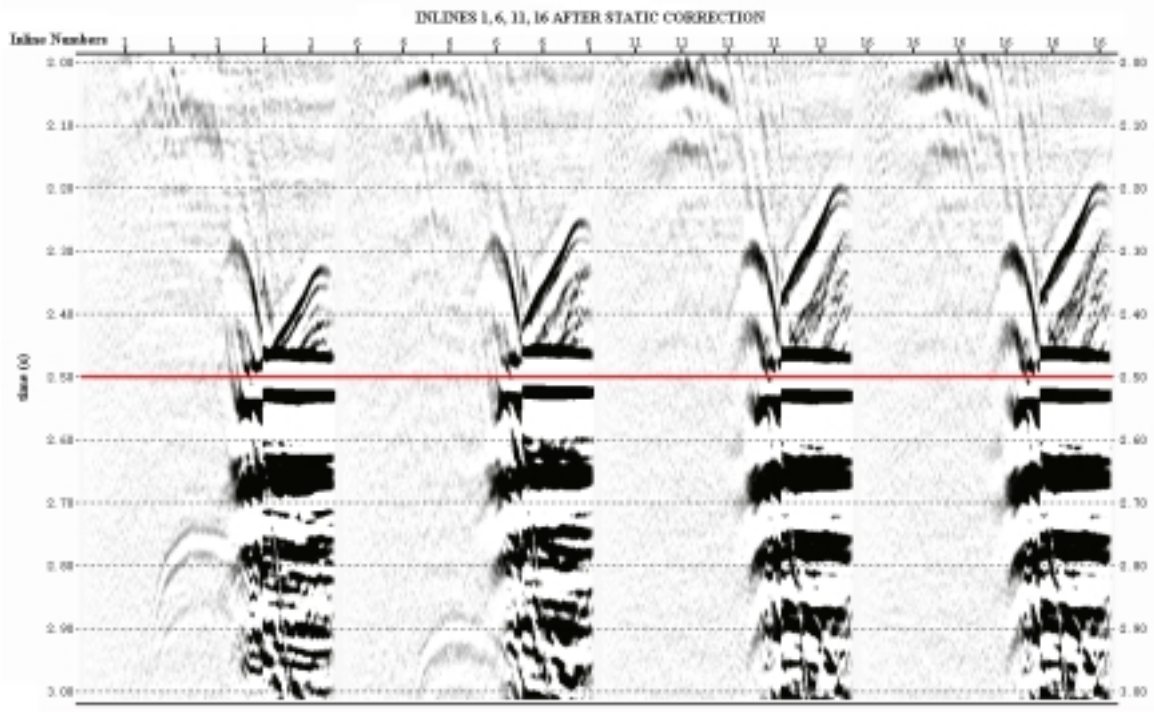

FIG.3.10.5. Corrected time shift using the metal plate reflection as a reference. Note that the red line indicates a smooth pass over a metal plate related reflections.

3.11 Imaging

In this section, I will finalize the conventional processing flow (see Figure 3.1.1) performing 3-D post-stack and pre-stack time migration on the physical model data. I will then make a comparative study on pre-stack image result of both the numerical and the physical model. In Chapter 4, I will analyze the 3-D post-stack image section to generate attributes.

3.11.1 3-D Post Stack Time Migration

Migration both collapses diffractions and moves dipping reflectors to their proper location. Different migration schemes including *Kirchhoff* migration (French, 1975, and Schneider, 1978), *finite-difference* migration (Claerbout, 1976), and *frequency-wave-number* domain migration (Stolt, 1978) are the most common time migration algorithms used. I will run the common offset frequency wave number time migration scheme based on Stolt's (1978) work:

$$p(x,y,t) \rightarrow P(k_x,k_y,\omega) \rightarrow P'(k_x,k_y,k_z \equiv [\omega^2/V^2 - k_x^2 - k_y^2]^{1/2}) \rightarrow p'(x,y,z), \qquad (3.11.1)$$

where, k_x, k_y, and k_z angular wave number in radians/meter,

ω is the angular frequency,

V is the RMS velocity,

$k_z = (\omega^2/V^2 - k_x^2 - k_y^2)^{1/2}$,

$p(x,y,t)$ is the recorded data, and

$p'(x,y,z)$ is the migrated data.

I implemented this migration scheme by using Paradigm Geophysical Company's product, Focus 5.2. Figure 3.11.1 demonstrates the migration result. Note that diffraction events (see Figure 3.10.3) have been focused as a result of migration such that the

channels are more clearly imaged. The interfaces between water layer and layer 1, layer 1 and 2, layer 2 and 3, layer 3 and 4 appear at 0.6, 1.18, 1.56, and 1.9 seconds.

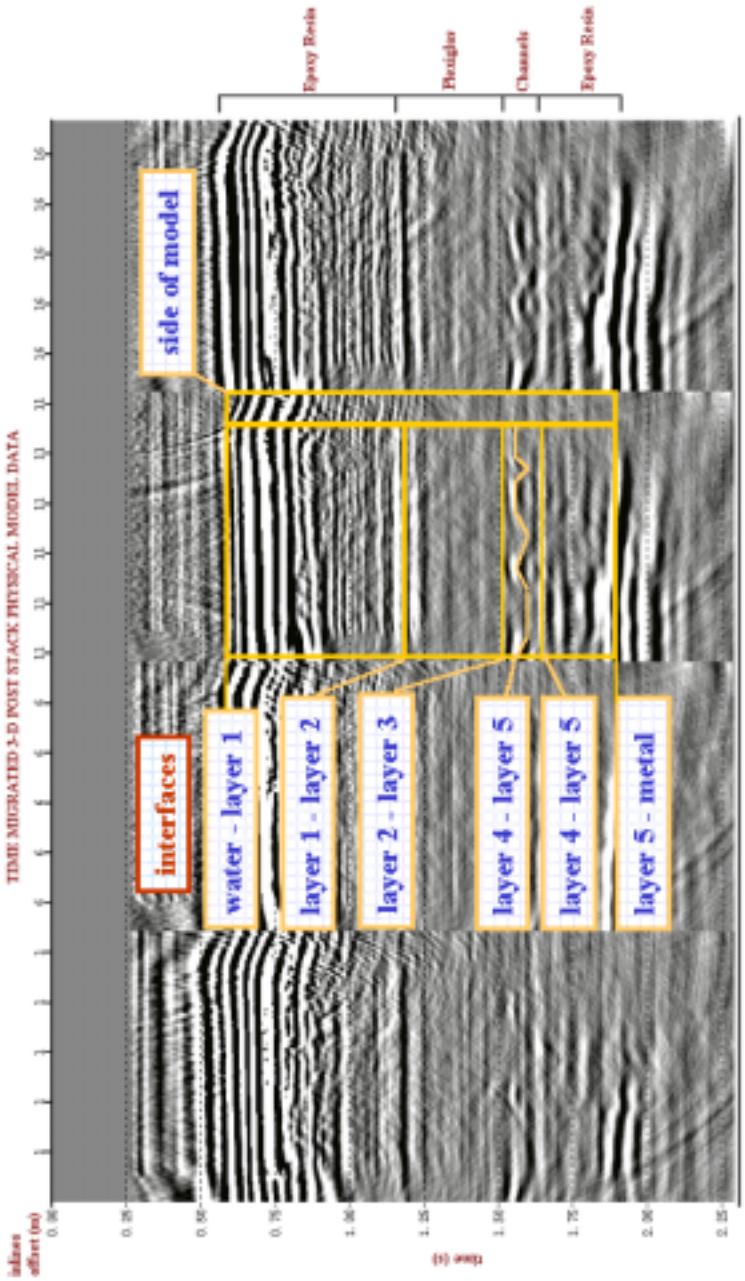

FIG.3.11.1. 3-D post stack time migrated data, inline sections 1, 6, 11, and 16.

Besides evaluating the migration results for inlines 1, 6, 11, and 16, I also generated the time slices from the interface between layer 1 and 2 (Figure 3.11.2), and the layer 2 and 3 (Figure 3.11.3).

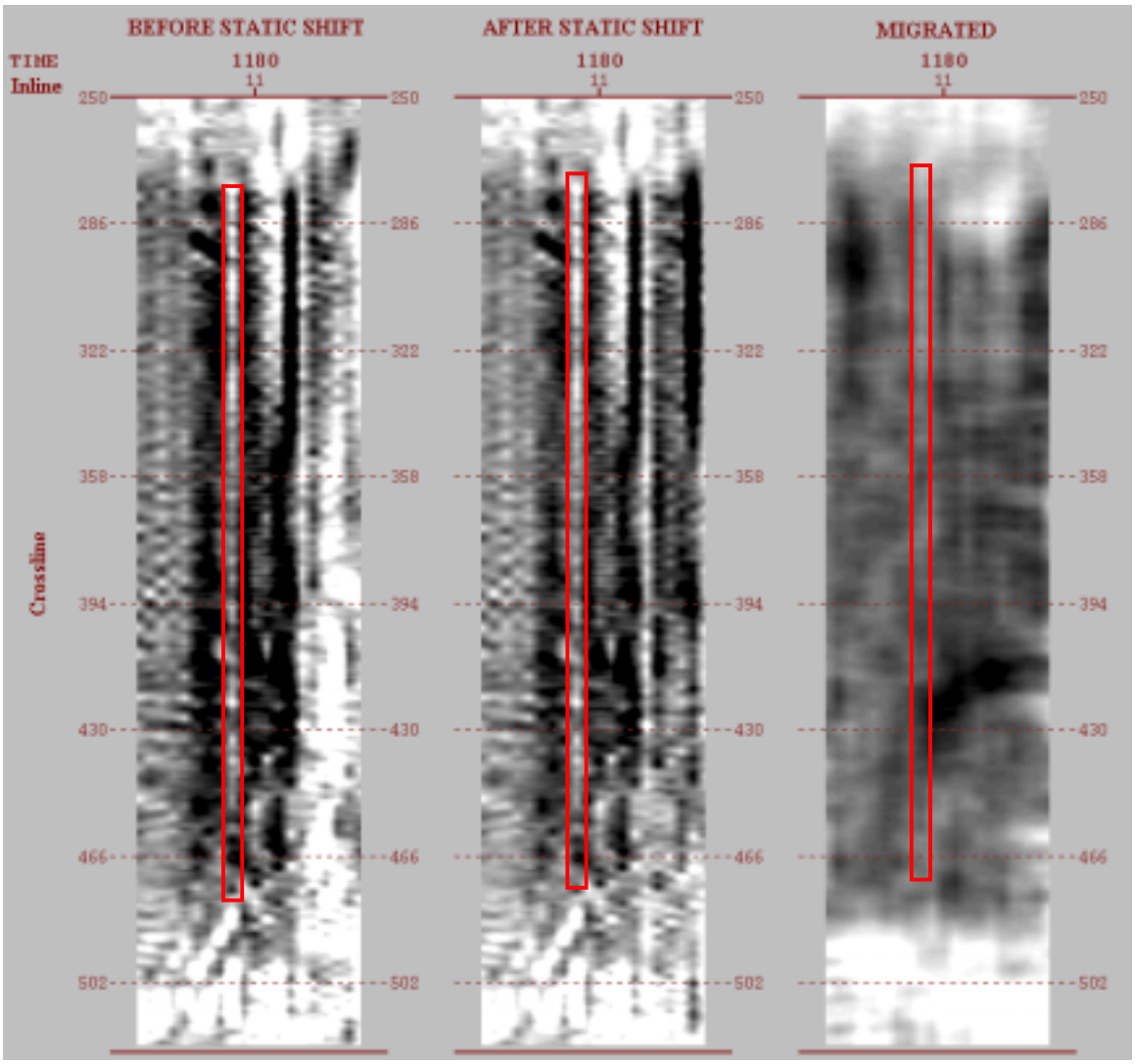

(a) (b) (c)

FIG.3.11.2 Time slices at 1800 ms corresponding to the interface between layer 1 and 2, (a) before static correction made on stacked data, (b) after static correction made on stacked data, and (c) time migrated data. Note that acquisition footprint marked with red rectangle in sections (a) and (b). This footprint is also seen on the migrated image.

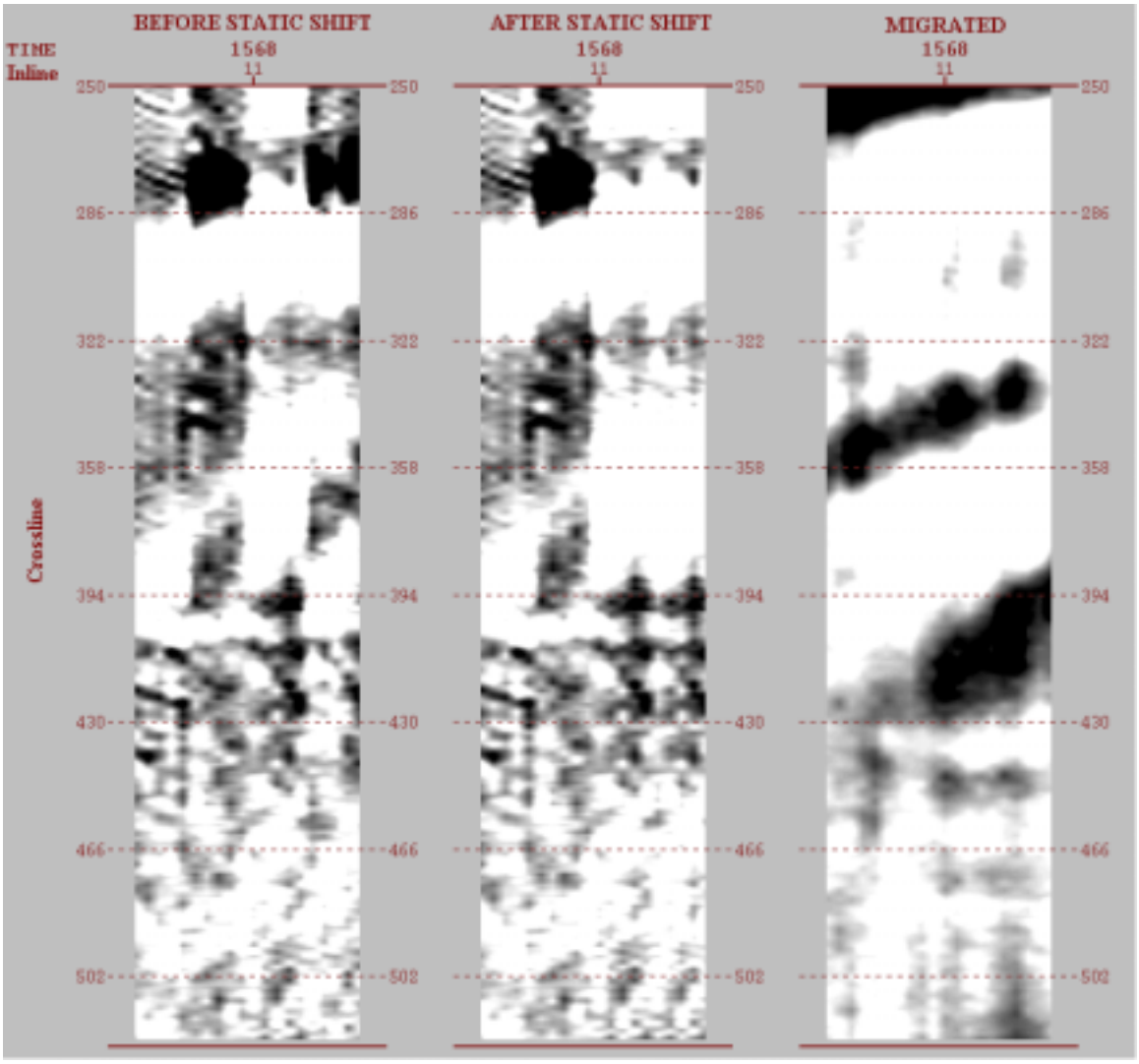

(a) (b) (c)

FIG.3.11.3. Time slices at 1568 ms from channels, (a) before static correction on stacked data, (b) after static correction on stacked data, and (c) time migrated data.

Note in the Figure 3.11.2 that the visibility of acquisition footprint marked with the red rectangles is highly reduced by the migration processes. Furthermore, Figure 3.11.3 explains how migration is effective in establishing the true locations of the subsurface

reflections (i.e., channels). Even so, distinct N-S and E-W lineations are seen in Figure 3.11.3.c.

3.11.2 3-D Pre-Stack Time Migration

In addition to 3-D post-stack time migration, I also applied 3-D pre-stack Kirchhoff time migration on the physical data. The aim of this study is to perform a comparative analysis between the migrated cross-section of both the physical and the numerical model. Figure 3.11.2.1 and 3.11.2.2 show the sparse migrated section along line 1 of both models.

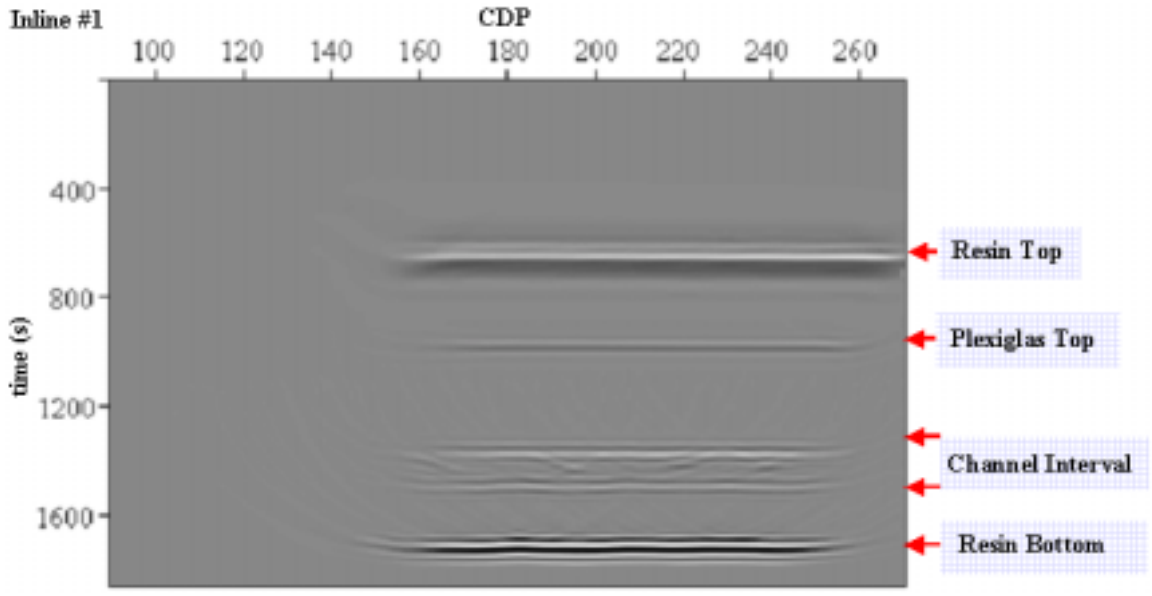

FIG.3.11.2.1. Sparse-migrated section of 3-D ray tracing.

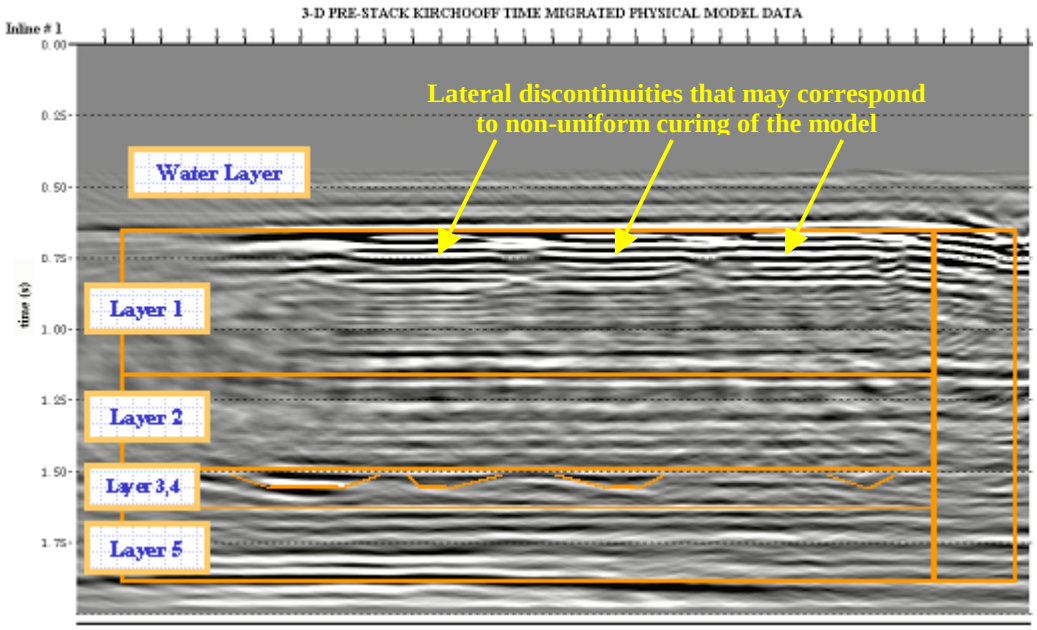

FIG.3.11.2.2. 3-D Kirchhoff pre-stack time migration on the physical model data.

Note from Figures 3.11.2.1 and 3.11.2.2 that the reflection arrival times show inconsistency inbetween the two models. This is due to defining the physical model initial parameters in ray tracing. The physical model is sensitive to variation in room temperatures and even curing of the model over time. Therefore, I went back and measured the model layer thicknesses and realized that the uppermost black epoxy resin layer (layer 1) showed almost 0.5 cm vertical expansion. In fact, the stack sections and the post stack migration results proved this anomaly as we look at the reflection times from the reflectors. It is also clear from Figure 3.11.2.2 that the top resin is not as homogenous as we assumed. Arrows indicate lateral discontinuities that may correspond to non-uniform curing of the model.

While the 3-D ray trace model is free of noise, it also lacks the diffractions necessary to properly image channel details. The physical model suffers from ringy characteristics of high frequency transducers and source generated back-scattered coherent noise. While careful data processing was performed on the physical model data, some of these unwanted events are still observable. Nevertheless, wave theory tells us that a significant amount of the channel energy will be seen as diffractions. Thus, inspite of the strong coherent noise in the physical model data, the channel boundaries are clearer in the physical model data rather than the numerical model.

Chapter 4

ATTRIBUTE ANALYSIS

In this chapter, I will make a comparative study by generating a suite of attributes on two dataset: Coherent noise filtered and unfiltered post-stack time migrated physical model data. Both of the datasets were generated by using the entire data processing described in Chapter 3, except I did not include 'Filtering the coherent noise' section in the processing flow while I produced the coherent noise unfiltered dataset. This evaluation will provide insight into how coherent noise affects the interpretability of the area of interest. I will finally build horizon cubes and extract time slices from generated attributes, which can be grouped in three categories, by using Paradigm Geophysical's 'Reservoir Characterization' software product.

4.1 Seismic Attributes

Seismic trace attributes are mathematical operations that are applied to each trace independently from the other traces. In this category, I will evaluate two types of trace attributes: instantaneous phase, and relative acoustic impedance.

4.1.1 Instantaneous Phase

The instantaneous phase enhances the continuity of events where amplitude information related with the reflection strength can be variable. Often, it makes weak coherent events appear more clearly. Instantaneous phase, θ(t), is obtained from the analytic or complex trace (Taner, *et. al.*, 1979):

$$\theta(t) = \tan^{-1} [\, d^{H}(t) / d(t) \,] , \qquad (4.1.1)$$

where, d(t) is the measured seismic data,

and $d^{H}(t)$ is its Hilbert transform.

Phase displays are expressed in degrees, usually from –180 (trough) through 0 (peak) to +180 (trough). Phase displays can be used for the regional visualization of stratigraphic features such as faults, pintchouts, angularities, onlaps, and in some cases fluid contacts. In this study, I will use the instantaneous phase attribute in order to discriminate channel fill material (black epoxy resin) from the surrounding matrix. Furthermore, I will look at the acquisition footprint and phase reversal in time slices. Figure 4.1.1.1 shows a 3-D horizon and extracted time slice corresponding to the interface between layers 1 and 2. In addition, Figure 4.1.1.2 and 4.1.1.3 show a 3-D horizon and extracted time slices corresponding to the interface between layer 2 and 3.

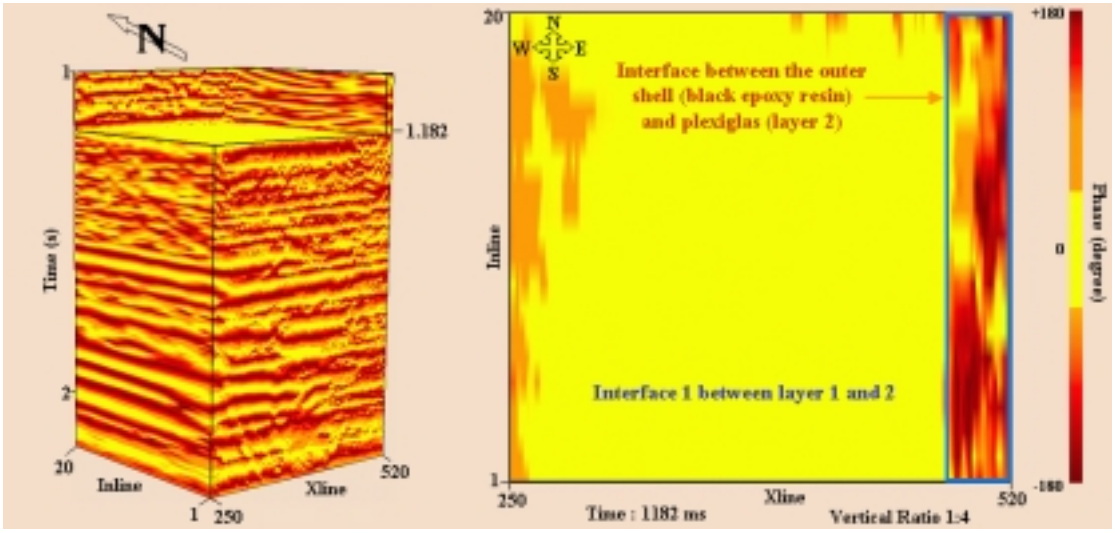

FIG.4.1.1.1. Instantaneous phase horizon cube (left), and time slice (right) of the coherent noise filtered data corresponding to the interface between layer 1 (top black epoxy resin) and layer 2 (top plexiglas block). Note that there is still little back-scattered coherent noise present.

Figure 4.1.1.1 indicates that the phase along the boundary of the low velocity uppermost black epoxy resin layer (layer 1) and the relatively high velocity lowermost acrylic plexiglas (layer2) is nearly constant with a value close to 0 degree. However, some phase distortions are observable towards the N-W. In addition, this distortion becomes more apparent in the deeper part of the model starting from the center towards East of the model. On the other hand, note that the boundary between the top plexiglas layer (layer 2) and the outer shell (black epoxy resin) is clear and the black epoxy resin outer shell also shows an 180 degree phase reversal indicated with the blue rectangle to the East of the model.

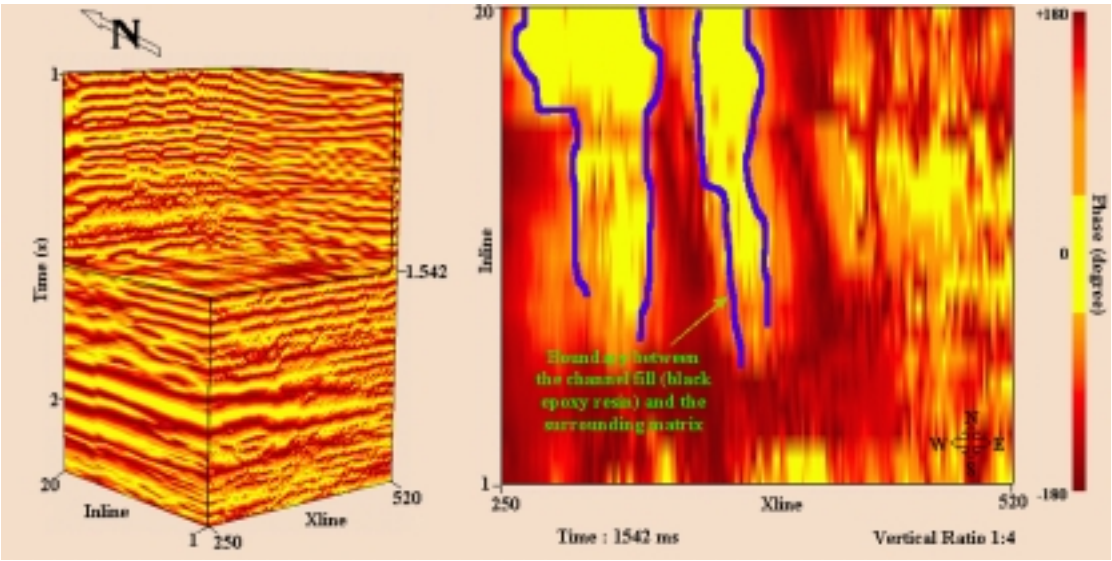

FIG.4.1.1.2. Instantaneous phase horizon cube (left), and time slice (right) of the coherent noise unfiltered data corresponding to the interface between layer 2 (top plexiglas block) and layer 3 (channel fill black epoxy resin). The boundary between the channel fills (yellow color) and the surrounding matrix (red color) is outlined in blue; there is a simple polarity change in reflection coefficient from 0 to 180 degree as we move in and out the channel. Note that there is high back-scattered coherent noise present.

Figure 4.1.1.2 indicates presence of the channels. The boundaries between the channel fill (black epoxy resin) and the surrounding matrix were drawn with the blue lines. However, we note that a high coherent noise masks the channels towards South of the model and does not allow us to draw a continuous boundary between the channel fill and its surrounding matrix.

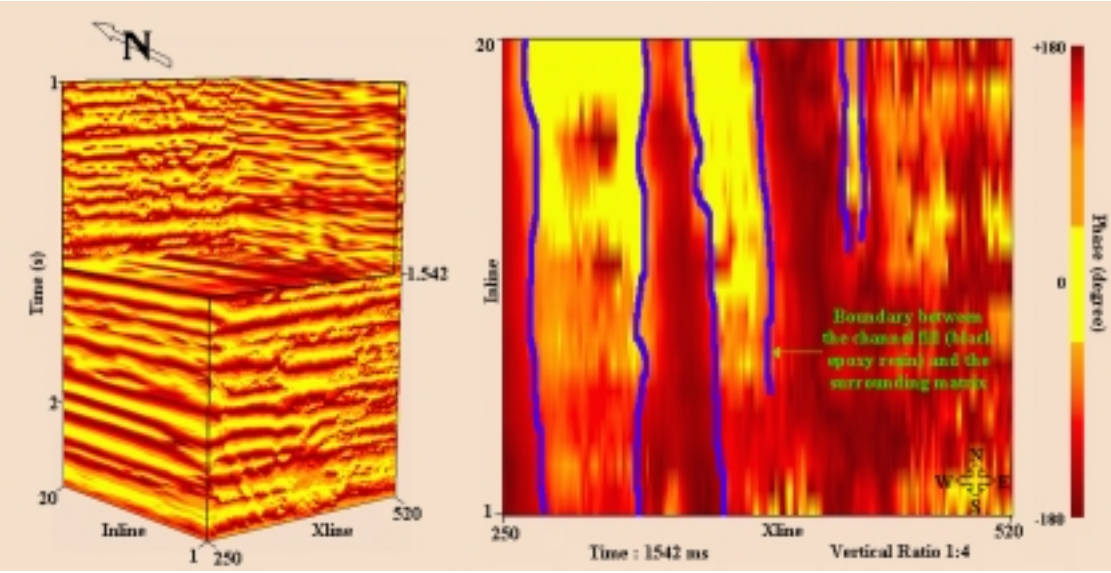

FIG.4.1.1.3. Instantaneous phase horizon cube (left), and time slice (right) of the coherent noise filtered data corresponding to the interface between layer 2 (top plexiglas block) and layer 3 (channel fill black epoxy resin). The boundary between the channel fills (yellow color) and the surrounding matrix (red color) is outlined in blue. Note that there is still little back-scattered coherent noise present.

A careful examination of Figure 4.1.1.3 shows that the boundary between these 'lithologies' is more linear and continuous in the South. In addition, we observe the presence of the third channel in the N-E, which is not observable in Figure 4.1.1.2.

Next, I generated a 3-D horizon cube and time slice corresponding to the interface between layers 3 and 4 shown in Figure 4.1.1.4 and 4.1.1.5.

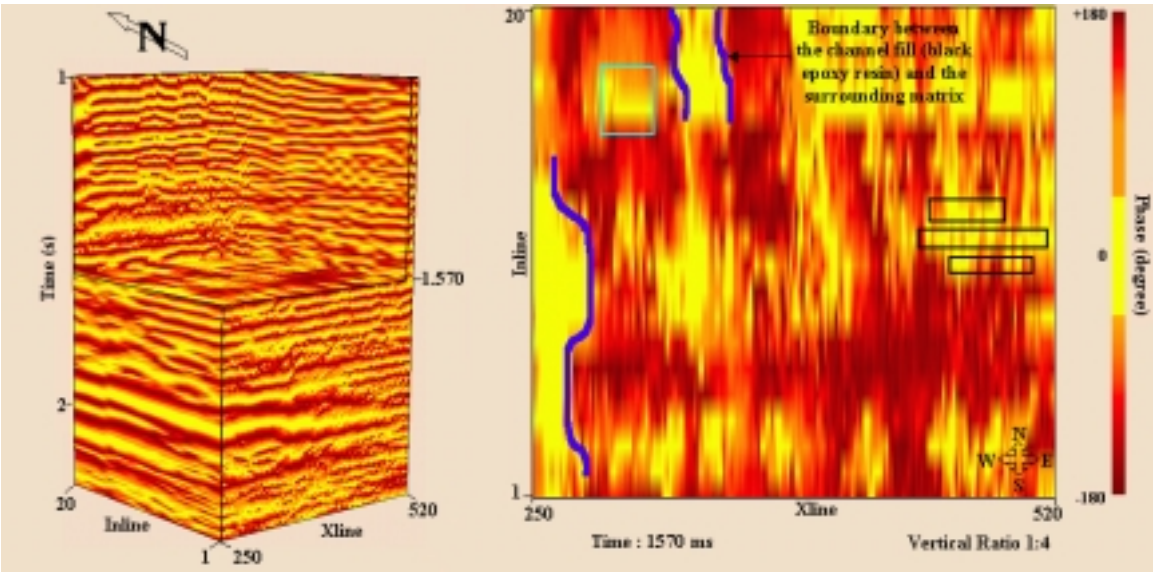

FIG.4.1.1.4. Instantaneous phase horizon cube (left), and time slice (right) of the coherent noise unfiltered data corresponding to the interface between layer 3 (channel fill black epoxy resin) and layer 4 (channel plexiglas). The boundary between the channel fills (yellow color) and the surrounding matrix (red color) is outlined in blue. Note that there is high back-scattered coherent noise present. In addition, the black boxes and the lineations along the N-S indicate the acquisition footprint, and the cyan boxes display the bottom interface between layer 3 and 4.

Figure 4.1.1.4 shows that in the presence of high coherent noise, the instantaneous phase attribute does not clearly exhibit the phase reversal phenomena in the interface between channel fill (black epoxy resin) and the surrounding medium itself. On the contrary, Figure 4.1.1.5 indicates clearer phase shifts along the boundary of the channel fill and its surrounding matrix. We also note that the phase shifts inside the channel fills shown with the cyan boxes are the indicators of roughness of the channel's bottom. The acquisition

footprint is not only caused by back-scattered coherent noise but also due to the acquisition geometry. As shown with the black boxes in Figure 4.1.1.4 and 4.1.1.5, the acquisition footprint appears as shiny stripes along the W-E direction due to narrow azimuth data as well as a consistent N-S overprint of lineations. Despite these artifacts, the instantaneous phase attribute exhibits a good correlation between the events and enhancement of the continuity of reflections as observed in 3-D horizon cubes.

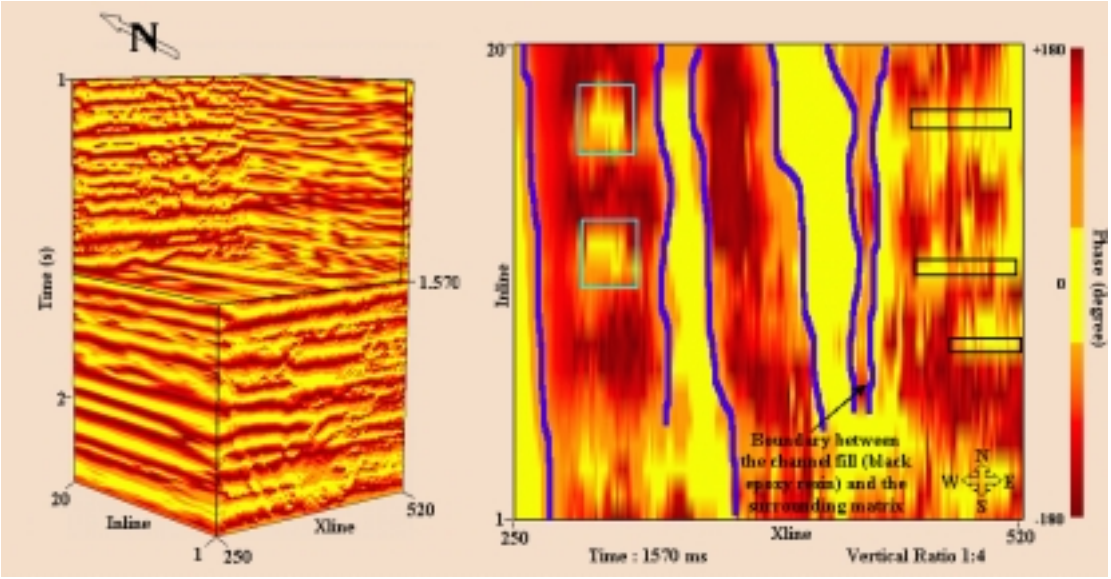

FIG.4.1.1.5. Instantaneous phase horizon cube (left), and time slice (right) of the coherent noise filtered data corresponding to the interface between layer 3 (channel fill black epoxy resin) and layer 4 (channel plexiglas). The boundary between the channel fills (yellow color) and the surrounding matrix (red color) is outlined in blue. Note that there is little back-scattered coherent noise present. In addition, the black boxes indicate the acquisition footprint along the W-E, and the cyan boxes display the bottom interface between layer 3 and 4.

4.1.2 Relative Acoustic Impedance

The use of an acoustic impedance estimate computed from high-resolution seismic data is a well-established tool in seismic interpretation. The approximate computation of acoustic impedance from the seismic data is usually based on a recursive formula given by Berteussen and Ursin, (1981):

$$Z_{k+1} = Z_k \exp (2r_k) , \qquad (4.1.2)$$

where,

Z_k is the acoustic impedance in layer k, and

r_k is the reflection coefficient for the interface between layer k and k+1.

We also define the reflection coefficient for the interface by:

$$r_n = \frac{(\rho_{n+1} V_{n+1} - \rho_n V_n)}{(\rho_{n+1} V_{n+1} + \rho_n V_n)} , \qquad (4.1.3)$$

where, ρ_n is the density of n^{th} layer in g/cm^3, and V_n is the velocity of n^{th} layer in m/s.

Equation (4.1.2) produces visually identical results to the interfaces for reflection coefficients less than 0.4 in absolute value. For this reason, relative acoustic impedance attribute maps will allow us to discriminate lateral variations including channel edges as

well as acquisition footprint. Figure 4.1.2.1 shows a 3-D horizon and extracted time slice corresponding to the interface between layers 1 and 2. In addition, the Figure 4.1.2.2 and 4.1.2.3 show a 3-D horizon and extracted time slices corresponding to the interface between layer 2 and 3.

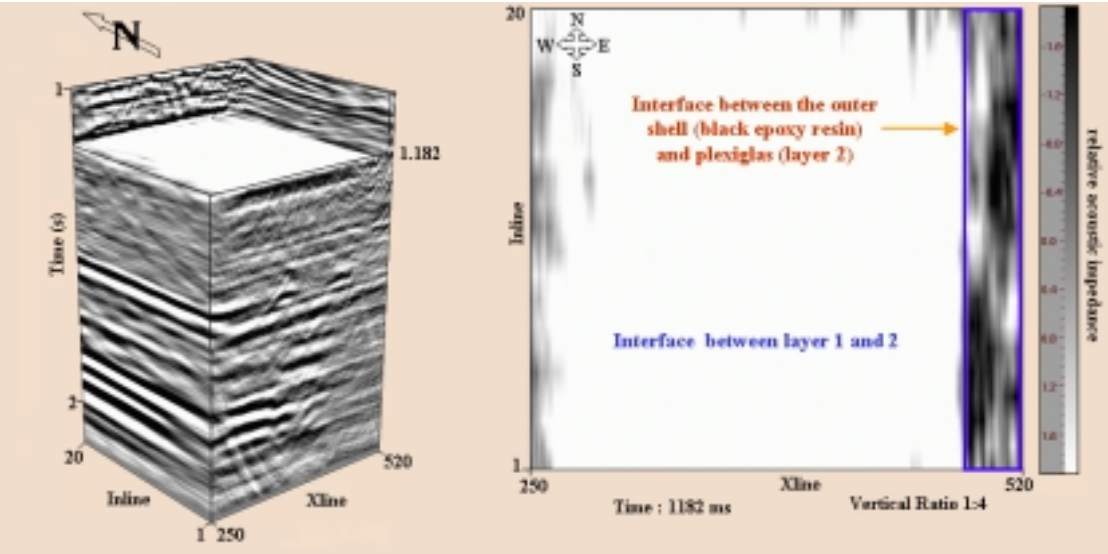

FIG.4.1.2.1. Relative acoustic impedance horizon cube (left), and time slice (right) of the coherent noise filtered data corresponding to the interface between layer 1 (top black epoxy resin) and layer 2 (top plexiglas block). Note that there is little back scattered coherent noise present.

Figure 4.1.2.1 shows no acoustic impedance change along the interface of layer 1 (black epoxy resin) and layer 2 (plexiglas block) except to the East. Recall from Chapter 2 that when I constructed my physical model, the layered model was embedded in larger black epoxy resin matrix on all six sides in order to avoid any water leakage into the model

(Figure 2.2). Therefore, it is not surprising to see a relative acoustic impedance change along this boundary, indicated with the blue rectangle, where the reflection coefficient is ± 0.106, which is large enough to produce impedance according to exponential recursive equation (4.1.2).

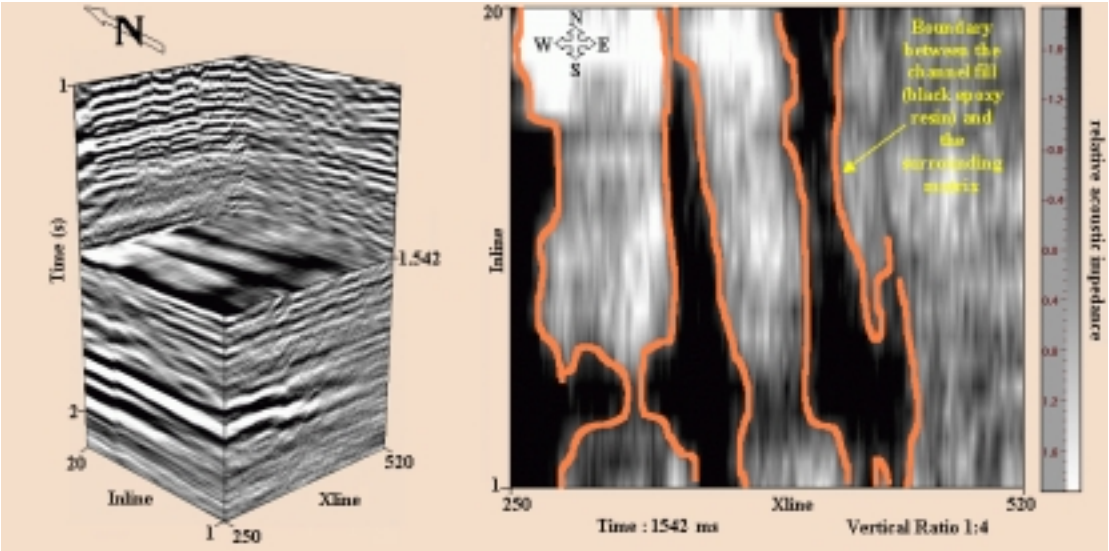

FIG.4.1.2.2. Relative acoustic impedance horizon cube (left), and time slice (right) of the coherent noise unfiltered data corresponding to the interface between layer 2 (top plexiglas block) and layer 3 (channel fill black epoxy resin). The boundary between the channel fills (white color) and the surrounding matrix (black color) is outlined in orange. Note that there is high back-scattered coherent noise present.

The boundary between the filled channels (black epoxy resin) and the surrounding matrix (plexiglas) is highlighted with the orange line along the N-S direction in Figure 4.1.2.2. However, it is not possible to establish the true channel's widths under the influence of

high back-scattered coherent noise. On the contrary, Figure 4.1.2.3 shows a sharp and regular acoustic impedance boundary between these lithologies. In addition, the existence of another channel along the N-E and S-E is obvious where the image is less effected by back-scattered coherent noise. We also note that this channel structure is visible on inlines between 10 and 20 in Figure 3.11.1, Chapter 3.

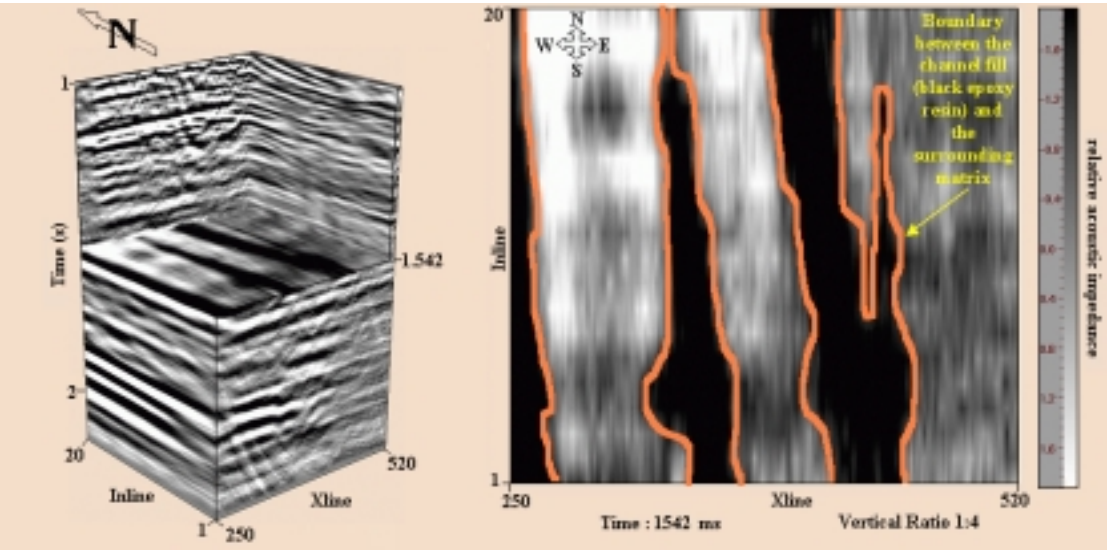

FIG.4.1.2.3. Relative acoustic impedance horizon cube (left), and time slice (right) of the coherent noise filtered data corresponding to the interface between layer 2 (top plexiglas block) and layer 3 (channel fill black epoxy resin). The boundary between the channel fills (white color) and the surrounding matrix (black color) is outlined in orange. Note that there is still little back-scattered coherent noise present.

Next, I generated a 3-D horizon cube and time slice corresponding to the interface between layers 3 and 4 shown in Figure 4.1.2.4 and 4.1.2.5. In this section, I attempted to

resolve the boundary between the channel fills (black epoxy resin) and layer 4, which is channel plexiglas.

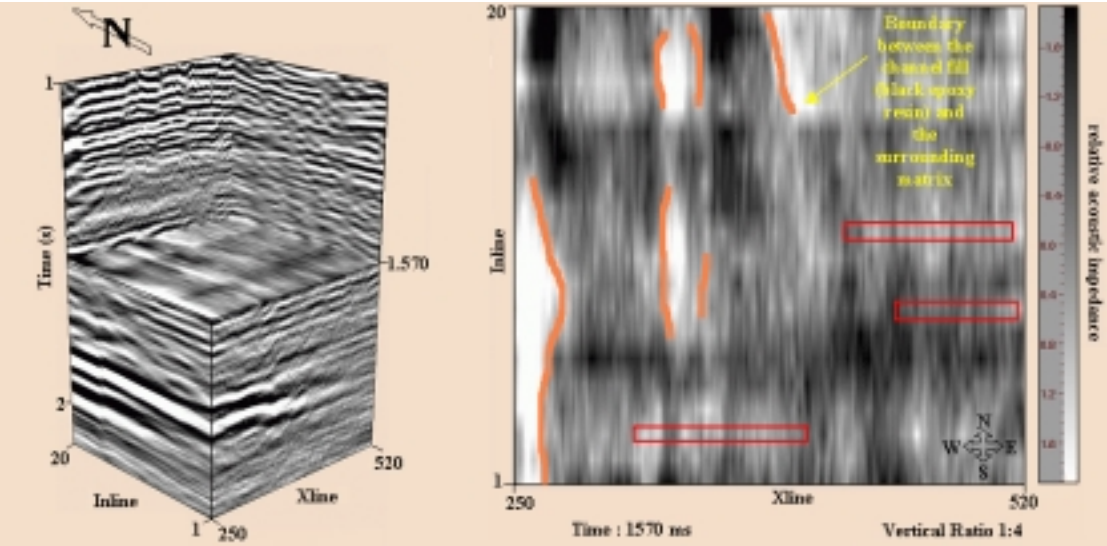

FIG.4.1.2.4. Relative acoustic impedance horizon cube (left), and time slice (right) of the coherent noise unfiltered data corresponding to the interface between layer 3 (channel filled with black epoxy resin) and layer 4 (channel plexiglas). The boundary between the channel fills (black color) and the surrounding matrix (white color) is outlined in orange. Note that there is high back-scattered coherent noise present. In addition, the red boxes and the lineations along the N-S indicate the acquisition footprint.

Figure 4.1.2.4 indicates that the boundary between the channel fills and the surrounding medium is quite distorted due to the presence of high back-scattered coherent noise. Therefore, it is almost impossible for us to draw a sharp boundary between them. On the other hand, the acquisition footprint is not only caused by back-scattered coherent noise but also due to acquisition geometry. As shown with the red boxes in Figure 4.1.2.4, the

acquisition footprint appears as shiny stripes along the W-E direction due to narrow azimuth data as well as a consistent N-S overprint of lineations. On the contrary, in Figure 4.1.2.5, these boundaries are more obvious when there is little coherent noise. In addition, the relative acoustic impedance map reveals more information about the contact between layer 3 (black epoxy resin) and layer 4 (channel plexiglas) that is indicated by the cyan boxes in Figure 4.1.2.5. We also note that the acoustic impedance variations inside the channel fills are the indicators of roughness of the channel's bottom.

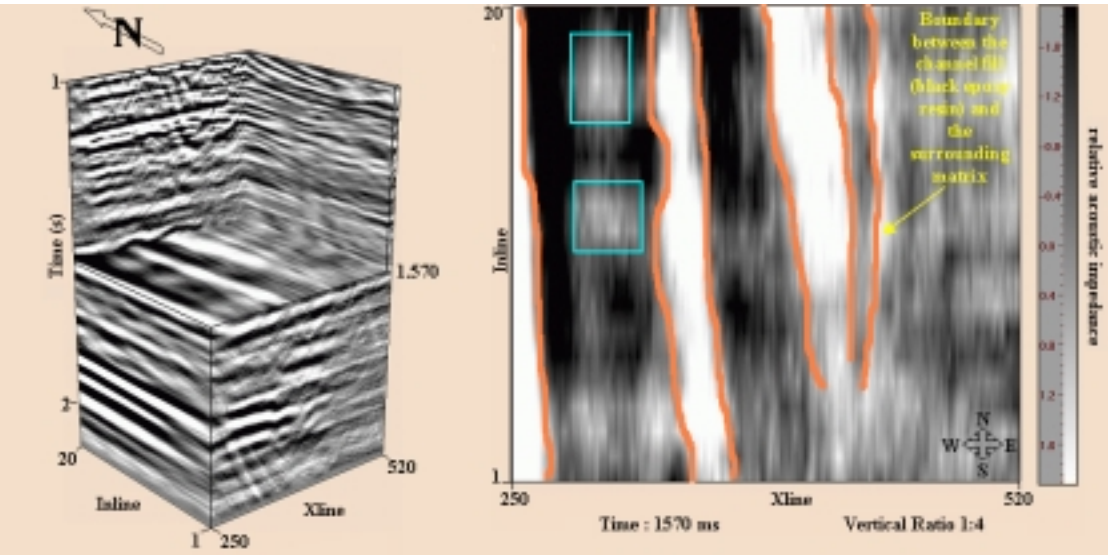

FIG.4.1.2.5. Relative acoustic impedance horizon cube (left), and time slice (right) of the coherent noise filtered dataset corresponding to the interface between layer 3 (channel fill black epoxy resin) and layer 4 (channel plexiglas). The boundary between the channel fills (black color) and the surrounding matrix (white color) is outlined in orange. Note that there is little back-scattered coherent noise present. In addition, the cyan boxes display the bottom interface between layers 3 and 4.

Finally, I generated a cross-section along line 16 for both the acoustic impedance attribute data influenced by little and high back scattered coherent noise shown in Figure 4.1.2.6.

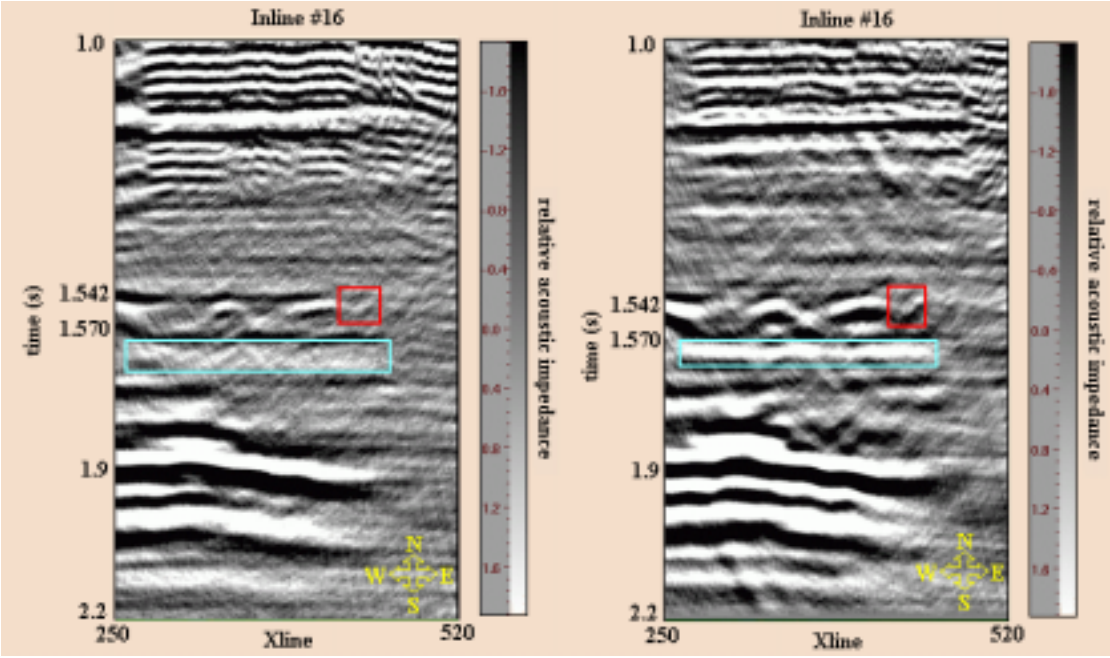

(a) (b)

FIG.4.1.2.6. The cross-section of relative acoustic impedance map along line 16 where (a) coherent noise unfiltered data has high coherent noise, and (b) coherent noise filtered data has little coherent noise. Note that the red boxes indicate the channel in East direction, and the cyan boxes exhibit the interface between layers 3 and 4 indicated by the cyan boxes along the W-E direction.

As we notice in Figure 4.1.2.6, the coherent noise filtered clearly shows the boundary between layers 3 (channel fill black epoxy resin) and 4 (channel plexiglas). We may also note that inhomogeneties inbetween time of 1.00 and 1.25 s are due to the model

construction. As a conclusion, the relative acoustic impedance attribute shows good discrimination between the channel fill and the surrounding matrix, and highlights the existence of the third channel to the East as well.

4.2 Spectral Decomposition Attributes

Spectral Decomposition is a form of wavelet transform where a single input trace is represented with a series of traces each with a different frequency band. It provides a novel means of utilizing seismic data and discrete Fourier transform (DFT) for imaging and mapping temporal bed thickness within the selected horizon window and geologic discontinuities over large 3-D seismic volumes (Partyka, *et. al.*, 1998). In this section, I will examine the generated time slices and the horizon cube over the channel area of interest by using the reflection strength (also called envelope) attribute given by Taner (1979):

$$A(t) = [\, f^2(t) + f^H(t) \,]^{1/2}, \qquad (4.2.1)$$

where,

A (t) is the reflection strength

$f^H(t)$ is the Hilbert transform, and

f (t) is the real part of the seismic trace.

Prior to generating the envelope attribute of 3-D volume, I specified the frequency range between minimum 15 Hz and maximum 55 Hz with the 10 Hz increment. In this interpretation, I used 35 Hz energy maps within the bandwidth of 30-40 Hz that describe the channel structures best. The signal-to-noise ratio is good, since it is also the transducer's resonance frequency. Figures 4.2.1 and 4.2.2 show 3-D horizon and extracted time slices corresponding to the interface between layers 2 and 3.

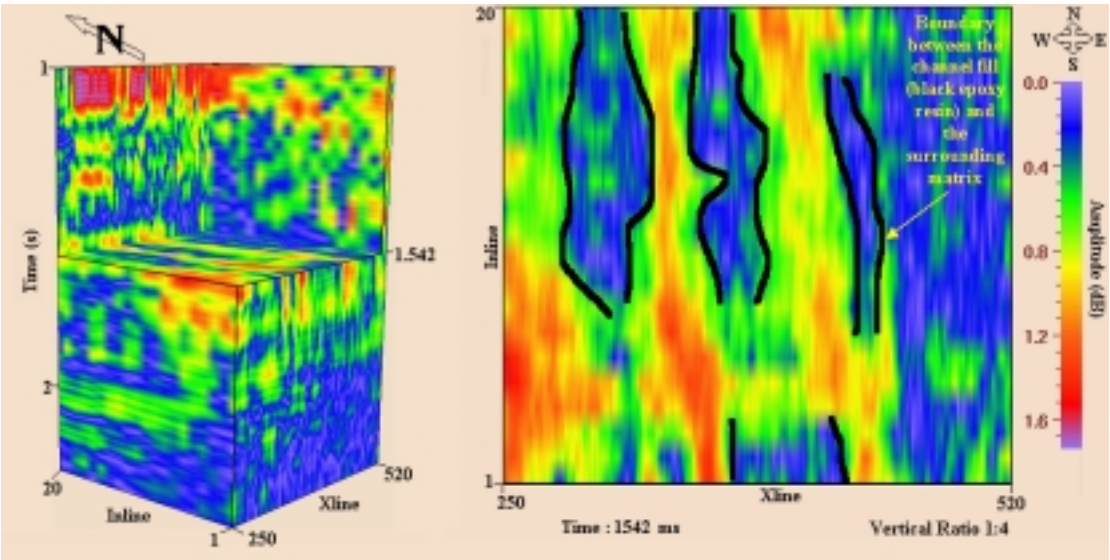

FIG.4.2.1. 35 Hz spectral component horizon cube (left), and time slice (right) of the coherent noise unfiltered dataset corresponding to the interface between layer 2 (top plexiglas block) and layer 3 (channel fill black epoxy resin). The boundary between the channel fills (blue color) and the surrounding matrix (green color) is outlined in black. Note that there is high back-scattered coherent noise present.

We see in Figure 4.2.1 that the reflection strength variations of the coherent noise unfiltered data along the W-E direction do not allow us to resolve the boundary between

the channel fills (black epoxy resin) and the surrounding matrix (channel plexiglas) under the influence of high back-scattered coherent noise. However, the reflection strength attribute map of the coherent noise filtered data in Figure 4.2.2 reveals the lateral lithology changes. Therefore, the boundaries between the channel fills (black epoxy resin) and the surrounding medium (channel plexiglas) become clearer outlined in black. In addition, continuity of the third channel to the East becomes more apparent to the South. Although the boundary between the channel fills and the surrounding matrix are more distinguishable with respect to the strong amplitude variations, the sharp boundary between them is still not clear.

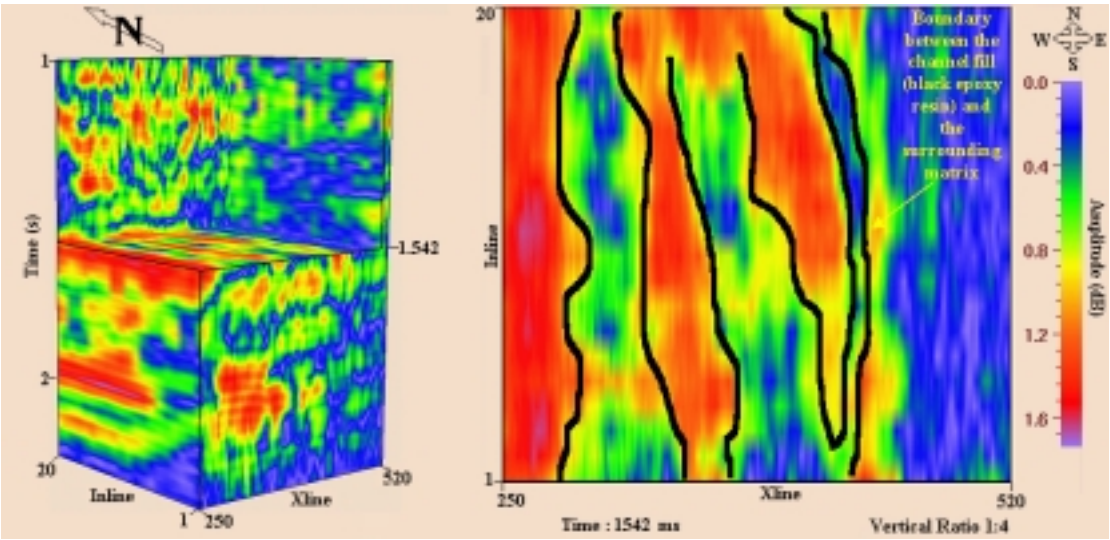

FIG.4.2.2. 35 Hz spectral component horizon cube (left), and time slice (right) of the coherent noise filtered data corresponding to the interface between layer 2 (top plexiglas block) and layer 3 (channel fill black epoxy resin). The boundary between the channel fills (green color) and the surrounding matrix (red color) is outlined in black. Note that there is little back-scattered coherent noise present.

Next, I generated a 3-D horizon and time slice corresponding to the interface between layers 3 and 4 shown in Figures 4.2.3 and 4.2.4. In this section, I attempt to resolve the boundary between the filled channels (black epoxy resin) and layer 4, and also the discontinuity of the channels under the influence of both high and little back-scattered coherent noise.

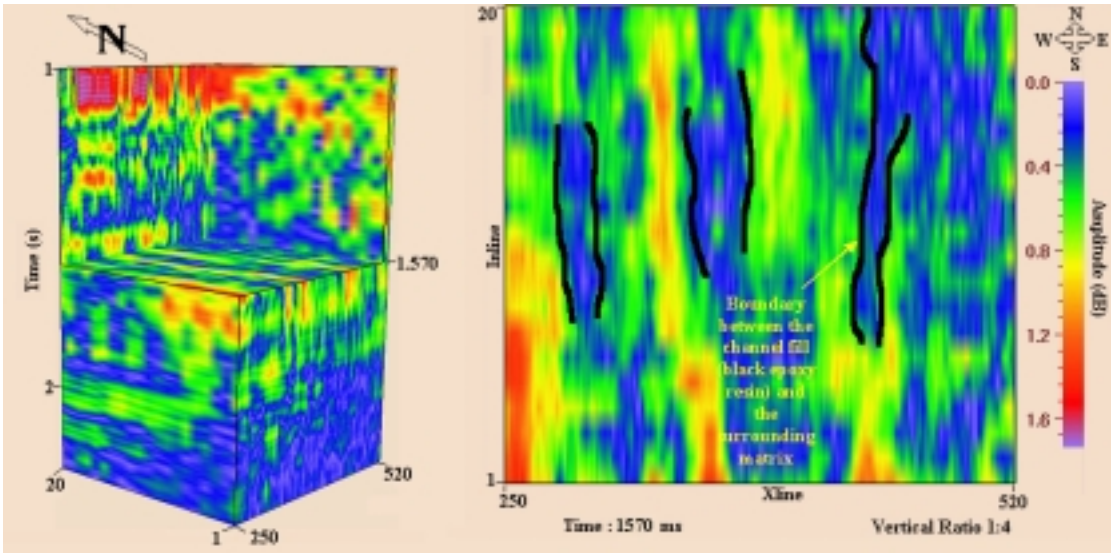

FIG.4.2.3. 35 Hz spectral component horizon cube (left), and time slice (right) of the coherent noise unfiltered data corresponding to the interface between layer 3 (channel fill black epoxy resin) and layer 4 (channel plexiglas). The boundary between the channel fills (blue color) and the surrounding matrix (green color) is outlined in black. Note that there is high back-scattered coherent noise present.

Figure 4.2.3 reveals no information about discrimination of the channel fills (black epoxy resin) and the surrounding matrix (channel plexiglas) under the influence of high

coherent noise. In addition, the reflection strength attribute map of the coherent noise unfiltered data does not allow us to interpret the roughness characteristic of the channel bottom since there is not reflection strength variations inside the channel fills. On the other hand, Figure 4.2.4 shows remarkable results in terms of discrimination of the channel fills and the surrounding medium itself. Although the reflection strength attribute map of the coherent noise filtered data does not indicate any discrimination of bottom interface between layer 3 (channel fills black epoxy resin) and layer 4 (channel plexiglas) compared to the seismic attributes, discussed in previous sections, they reveal discontinuities in 35 Hz spectral component maps as we see in Figure 4.2.2.

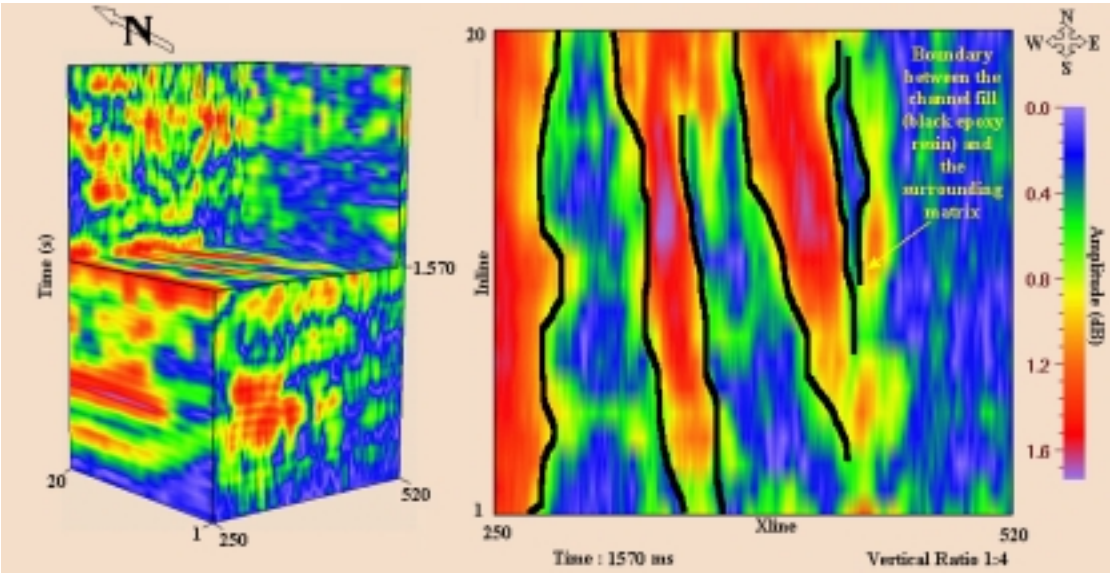

FIG.4.2.4. 35 Hz spectral component horizon cube (left), and time slice (right) of the coherent noise filtered data corresponding to the interface between layer 3 (channel fill black epoxy resin) and layer 4 (channel plexiglas). The boundary between the channel fills (blue color) and the surrounding matrix (red color) is outlined in black. Note that there is little back-scattered coherent noise present.

4.3 Geometric Attributes

I did not generate the geometric attributes such as dip/azimuth, coherence, and so forth, due to not having enough data volume in this research.

Chapter 5

CONCLUSION

A. I have successfully used physical modeling to evaluate the impact of acquisition and data processing on seismic attribute analysis of a complex channel system. Strong acquisition footprint appears due to mode conversions and side-scattered noise that were inadequately sampled in the acquisition design.

B. Careful data processing is essential to minimizing the source-generated noise. τ-p filters, including deconvolution in the τ-p domain, proved to be particularly effective in improving the data quality.

C. Seismic attributes provided a reasonable discrimination of channels and fill. In particular, instantaneous phase, and relative acoustic impedance demonstrated the phase reversal expectation in high-low velocity transition zone.

D. Spectral decomposition and reflection strength attributes improve vertical resolution but do not sharpen the channel boundaries.

E. The limited 3-D data volume made it difficult to create and analyze geometric attributes.

F. In support of this thesis, I also significantly advanced the AGL's capabilities to model 3-D elastic wave propagation for future attribute and 3-D AVO studies.

G. Sensitive measurement of transducer directivity is necessity in order to correctly determine amplitude variations in seismology.

H. The laser scanner is a useful tool for accurately mapping the surface of the physical model. This accurate surface map can then be input to a numerical modeling program to provide a comparison between the physical model data and the numerical model data.

I. I also found that our new laboratory facility in the basement of the 6-story Science and Research building is significantly noisier than our former one story prefabric building site. To attenuate such noise, our new electronic system will need to vertically stack seismic traces to improve the signal-to-noise ratio.

I also learned that 3-D asymptotic ray theory modeling can help optimize my physical modeling acquisition design. Specifically, I collected 1.6 million traces at 6 s recording time over a 3 month period. Numerical modeling showed my latest channel diffractions arrived at less than 2 s. I also needed to discard the furthest 40 percent of the traces as they fall beyond the NMO stretch mute. Finally, my source and receiver spacing was 2 times too far for the 30 Hz peak frequency used. In summary, with proper sampling, I could have imaged an area 8 times as large with the same number of traces.

REFERENCES

Auld, B.A., 1973, *Acoustic Fields and Waves in Solids*, John Wiley & Sons, Canada

Berteussen, K.A., and Ursin, B., 1983, Approximate computation of the acoustic impedance from seismic data: Geophysics, **48**, 1551-1558.

Brown, A., 2001, Understanding seismic attributes: Geophysics, **66**, 47-48.

Calderon, C., Shirley, T., Smith, J., Hinkley, D., and North, P., 1999, Efficient computation of 3D DMO responses for 3D-acquisition footprint analysis: SEG Expanded Abstracts.

Carning, A., and Gardner, G., 1998, Reducing 3-D acquisition footprint for 3-D DMO and 3-D prestack migration: Geophysics, **63**, 1177-1183.

Daley, P.F., Marfurt, K.J., and McCarron, E.B., 1999, Finite-element ray tracing through structurally deformed transversely isotropic formations: Geophysics, **64**, 954-962.

Drummond, J., Ryan, J., and Kasmi, R., 2001, Adapting to noisy 3-D data: Enhancing Algerian giant field development through strategic planning in 3-D seismic in Berkine Basin: The Leading Edge, **20**, 718-728.

Entralgo, R., and Spitz, S., 2001, The challenge of permanent 4-C seafloor systems: The Leading Edge, **6**, 614-620.

Gulunay, N., 1999, Acquisition geometry footprint removal: SEG Expanded Abstracts, 637-640.

Hill, S., Shultz, M., and Brewer, J., 1999, Acquisition footprint and fold-of-stack plots: The Leading Edge, **6**, 686-695.

Julian, B.R., and Gubbins, D., 1977, Three-dimensional seismic ray tracing: J. Geophys., **43**, 95-114.

Krail, P., 1994, Vertical cable as a subsalt imaging tool: The Leading Edge, **8**, 885-887.

Krail, P.M., and Shin, Y., 1990, Deconvolution of a directional marine source: Geophysics**, 55**, 1542-1548.

La Bella, G., Loinger, E., and Savini, L., 1998, The cross-shooting methodology: Design, acquisition, and processing: The Leading Edge, **17**, 1549-1553.

Marfurt, K., Scheet, R., Sharp, J., and Harper, M., 1998, Suppression of the acquisition footprint for seismic sequence attribute mapping: Geophysics, **63**, 1024-1035.

Moldoveanu, N., and Ronen, S., 1999, Footprint Analysis of Land and TZ Acquisition Geometries using a 2-D finite difference anisotropic viscoelastic modeling: SEG Expanded Abstracts.

Moser, J.T., 1991, Shortest path calculation of seismic rays: Geophysics, **56**, 59-67.

Nemeth, T., Sun, H., and Schuster, G.T., 2000, Separation of signal and coherent noise by migration filtering: Geophysics, **65**, 574-583.

Nelson, R.H., 1986, *Exploration Geophysics*, Gulf Publishing Company, Houston.

Transducer Handbook, 2001, Panametrics, USA.

Peyton, L., Bottjer, R., and Partyka, G., 1998, Interpretation of incised valleys using new 3-D seismic techniques: A case history using spectral decomposition and coherency: The Leading Edge, **9**, 1294-1298.

Sheriff, R.E., and Geldart, L.P., 1995, *Exploration Seismology*, Cambridge University Press

Soubaras, R., 2002, Attenuation of acquisition footprint for non-orthogonal 3D geometries, EAGE 64th Conference and Exhibition, Florence, Italy.

Stephen, K.C., and Stolt, R.H., 2002, Applications of 3D data mapping-Azimuth moveout and acquisition footprint reduction, SEG Convention, Salt Lake City, Utah.

Stolt, R.H., 1978, Migration by Fourier transform: Geophysics, **43**, 23-48.

Stolt, R.H., 2000, Seismic data mapping and reconstruction: Geophysics, **67**, 890-908.

Stone, D., 1994, Designing seismic surveys in tow and three dimensions, Soc. Expl. Geophys., Tulsa, OK.

Taner, M.T., Koehler, F., and Sheriff, R.E., 1979, Complex trace analysis: Geophysics, **44**, 1041-1063.

Wardhana, R., 2001, Analysis of Time-Lapse Seismic Technology Using a Physical Model of a Porous Channel Sand, 76-88.

Yilmaz, O., 1987, *Seismic Data Processing*, SEG, Tulsa

Ziolkowski, A., and Stoffa, P.L., 1983, Seismic source decomposition: Geophysics, **48**, 1-11

APPENDIX A

LASER SURFACE SCANNING

A.1 Introduction

Numerous situations arise in which it is necessary to digitize a 3-dimensional surface, and one method of doing so is to use a laser surface scanner. Such devices are currently used in a wide range of applications, including medicine, CAD, forensics, natural sciences, and animation, to name but a few. Most commercially available laser surface scanners employ one or more laser / camera assemblies, where the object is illuminated with a spot or stripe of laser light, which is then viewed by a camera from an offset angle, thus allowing the 3-D surface coordinates along the laser line to be calculated by triangulation. The entire object surface is covered by either moving the object, moving the laser / camera assembly, or scanning the laser spot.

Today in the Allied Geophysical Laboratories [AGL], a Model 300 laser scanner supplied by 3DD corporation is widely used in order to measure thicknesses, widths, and heights of geological structures such as salt domes, channels, and other non-linear structures. These geologic models are built at an appropriate scale to simulate real world problems. Seismic data can be acquired over these models and used to test processing and interpretation technology. Unfortunately not all of today's geophysical studies are based on physical models but mostly on numerical models. The laser scanning process

establishes a link between physical and numerical studies. The method of numerical modeling consists of generating synthetic traces, which are analyzed with targeted processing, or interpretation techniques. To create these synthetic traces, one needs a model that exhibits either simple or complex geology depending on the study requirements. Spatial data information from any physical model can be gathered using laser surface scanners and then input to numerical model simulation software to generate these traces. Part of this thesis covers this special scanning effort from beginning to end and the processing of these spatial data with different software applications to make a suitable model for numerical modeling.

A.2 Laser Scanner Description

Commercial laser scanners are somewhat inflexible, in that each model tends to be designed for scanning a particular type of 3-D object only. The volume and dimensions of objects control the type of laser scanner needed. There are two types of laser scanners available, mechanical and hand-held. The mechanical laser scanners attached to non-stationary assemblies controlled by computer are often used for large objects whereas hand-held scanners are employed on relatively small objects. Although they differ in terms of assembly structure and control, in theory both work by the same optical rules. Figure A.2.1 simply demonstrates the components of a laser scanner. Our 3DD 300 Model scanner is a combination of the two types. According to needs, our laser scanner can be assembled either on tripod, which is manually moved in any directions, or on an electro-mechanical system. One important issue when choosing an appropriate assembly

system is that the receiver lenses and the fan beam of the laser light should be free of any obstruction. This will definitely affect relief information gathered from the object.

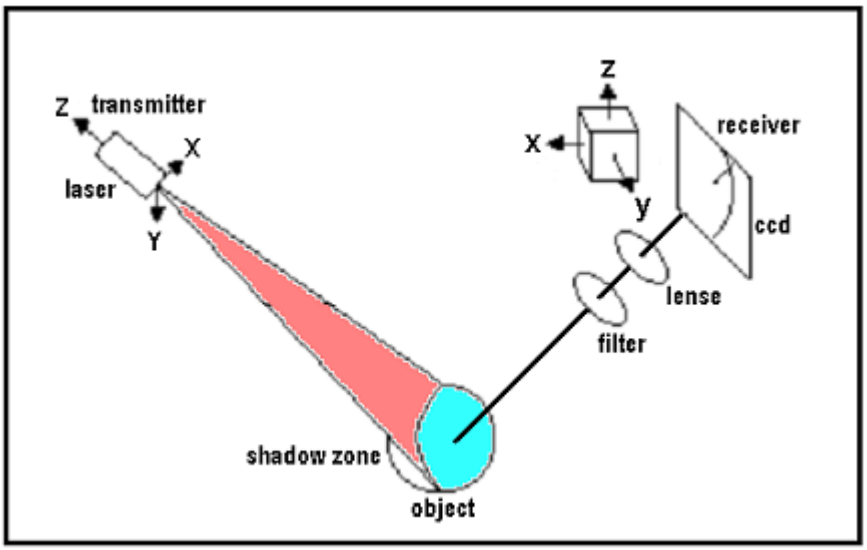

FIG. A.2.1. Components of laser scanner and basic optical principles

Laser scanners show different performances in terms of resolution. Resolution is simply a function of the illuminated surface of object by the laser beam (X, Y, Z cm^3) over the distance between the laser projector and the object surface (X cm). The degree of scanning surface capability of a laser scanner device is measured in points per stripes. Stripes can be imagined as 2-D laser lines consist of group of points. The unit volume of a 3-D object that is illuminated by laser beam is proportional to the distance between the laser scanner and the object. There is a limited number of laser stripes to cover a 3-D object no matter what the distance is. A larger distance between the laser generator and the object would enable the laser beams to cover a larger area on the object. However, since the number of points of each stripe are limited, dx (distance between points in the x-direction) and dy (distance between stripes) must increase. This definitely affects the

sampling of data and the resolution. High-resolution data plays an important role on information that is collected over an object. To increase the resolution, an object can be divided into the small segments and each of these are scanned one by one and finally merged together to realize the whole object. However, it is very time consuming to acquire these data and requires a large amount of disk space. Next, I will explain how acquisition may be possible over my plexiglas channel object both saving some storage space and obtaining high resolution.

A.3 Acquisition

Seismic interpretation is usually checked by comparing field data with synthetic data. Therefore, accuracy of presenting geological structures in numerical modeling positively changes the comparison between them. Scanning an object is somewhat similar to multistreamer marine acquisition in the seismic world. On the other hand, processing of scanned data may not be as difficult as that of seismic data but should be given careful attention. I now explain the data processing of the scanned channel model in stepwise manner in Table A.3.1.

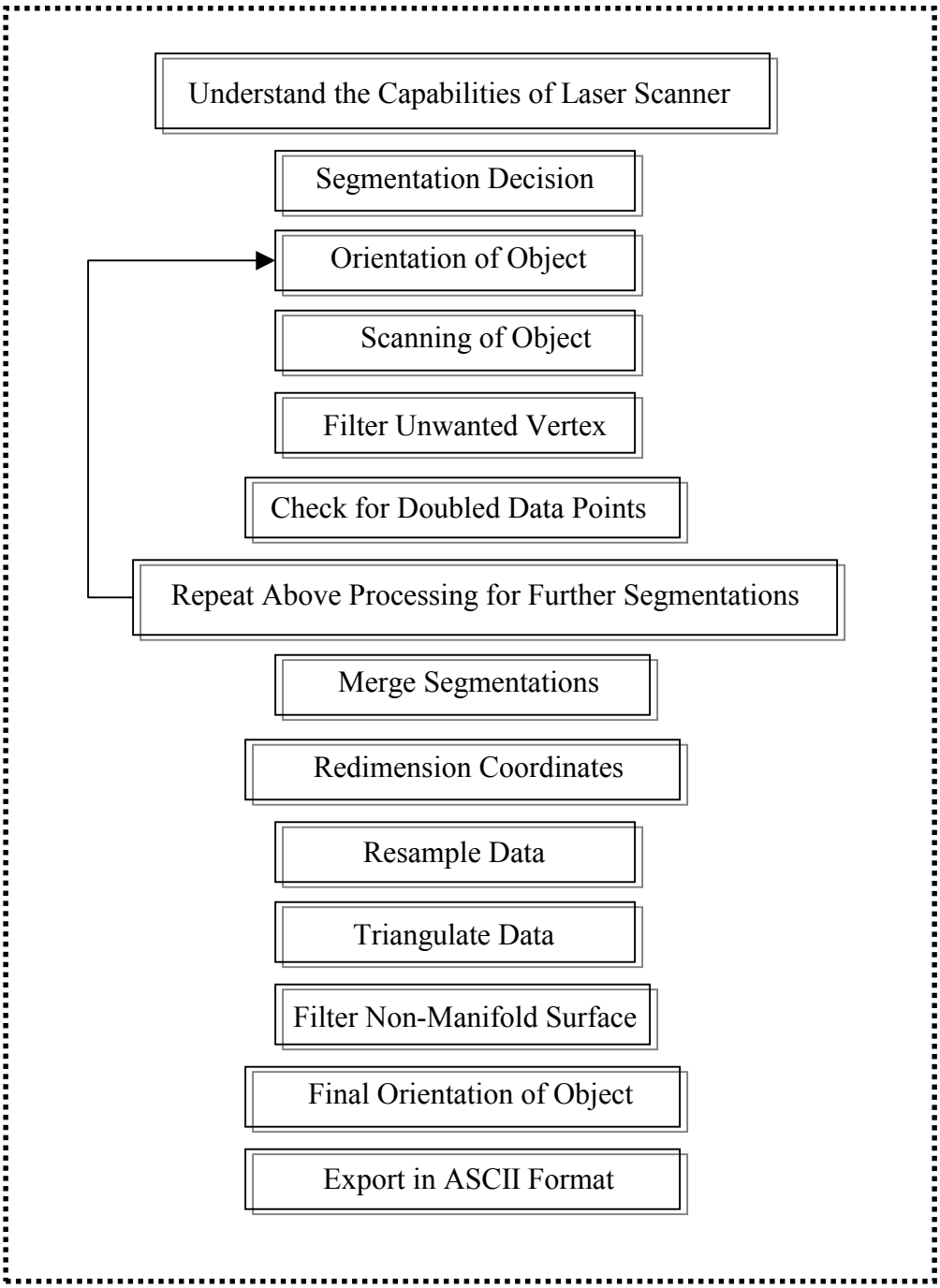

Table A.3.1. Laser Scan processing flow.

Physical and numerical seismic modeling experiments were conducted on a model with flat layers. The model contained a complex channel system curved into one block of plexiglas and embedded in between plexiglas and resin blocks. In order to generate a numerical model of this structure, I needed to define z (thickness), x (direction along x-axis), and y (direction along y-axis) of each layer. For flat layers, the thickness (z) is constant for every x and y location so that they can be easily defined. However, the channel model used in this physical modeling experiment (Figure A.3.1) needs some special treatment in order to extract x, y, and z information.

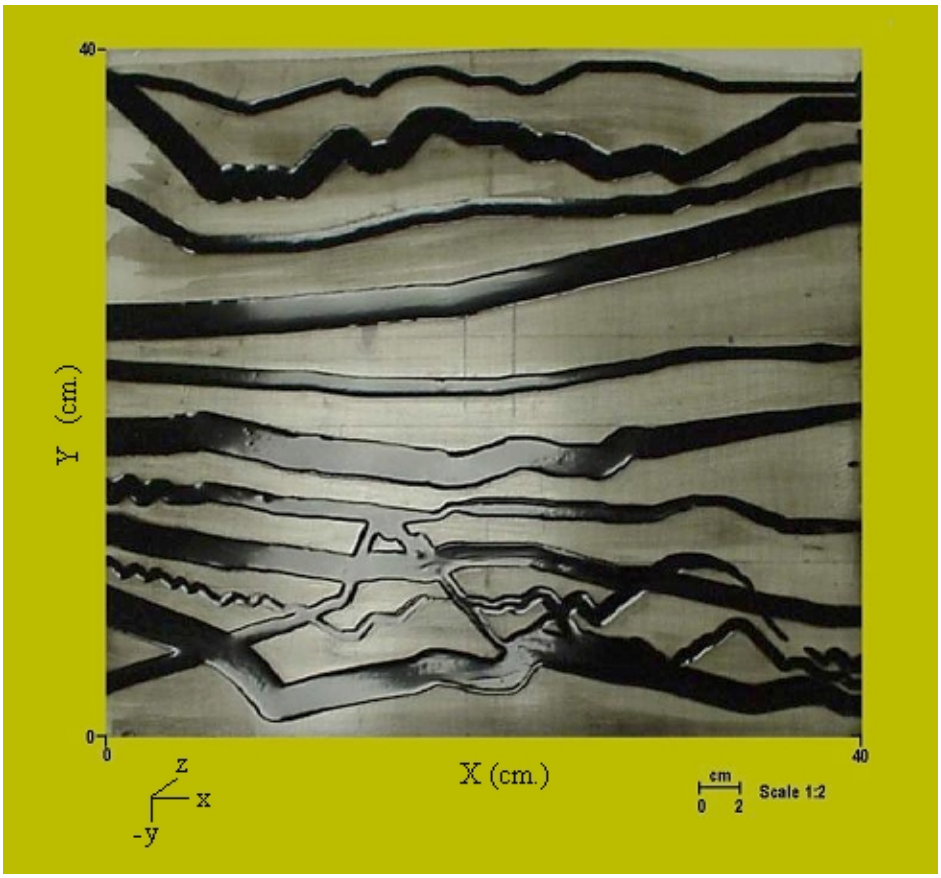

FIG. A.3.1. 40cm*40cm*1.5cm Plexiglas channel structure filled with resin.

Our A 300 model laser scanner generates laser stripes with 30 degree fan-out angle and has a point density of 512 per stripe and 500 lines. Having such a highly capable laser scanner, it should be possible to scan the plexiglas channel model only once from an appropriate distance and angle. This effort saves time, data storage space, and extra processing steps such as merging each individual segmentation with another.

Theoretically, laser scanners gather data from flat or rough surfaces by following optic rules. The laser beam is emitted from the transmitter to the surface of the object and reflected back from surface to receiver. Plexiglas is a transparent material that allows the laser beam go through its surface all the way to the bottom of the block. Therefore, the laser beam will never be reflected from the surface and that information cannot be acquired. To avoid the problem, the entire surface of the plexiglas channel model was painted with white paint before acquiring the data over it. Orienting an object properly relative to the laser scanner prior to scanning is a very crucial step. Since the laser stripes approach the surface of the object at an angle, some steeply dipping channel sides cannot be detected and the information may be lost from that part of the channel structures. To minimize this problem, I tilted the model approximately at an angle of 45 degree relative to the laser scanner and stabilized the laser scanner on a flat wooden structure high enough from the middle of the channel model (approximately 80 cm.) in order to cover the whole plexiglas channel model with laser stripes. This resulted in good resolution in both the x-direction ($dx \approx 0.78$ mm) and the y-direction ($dy \approx 0.78$ mm). The model A

300 laser scanner is interfaced to a computer program called Realscan which controls range characteristics such as points per stripe and number of lines generated during scanning. In this entire effort, the full range characteristics of the software within the maximum limitations of hardware were used.

A.4 Processing

An aim of processing the data is simply to clean it from unwanted features. Like seismic data processing, the steps of processing laser scanned surface data could vary depending on how the data is acquired. Table A.1 shows the processing procedure that is commonly followed for laser utility when using physical model materials in the Allied Geophysical Laboratories (AGL). During processing of scanned complex channel structures model, some steps that are not relevant to or not required for this work were skipped.

A.4.1 Vertex Filtering

Realscan software outputs the data in an ASCII format, which is a recognized format for most of the commercial software used in processing. During the processing, laser scanned surface data is mostly treated visually. Different topography visualization and processing software were used to make the processing less complicated. First, 3-D Scan and Surf software was used in order to see the data vertices. A vertex is defined as the intersection of two or more edges, it has coordinates in three dimensional space (Figure A.4.1.1)

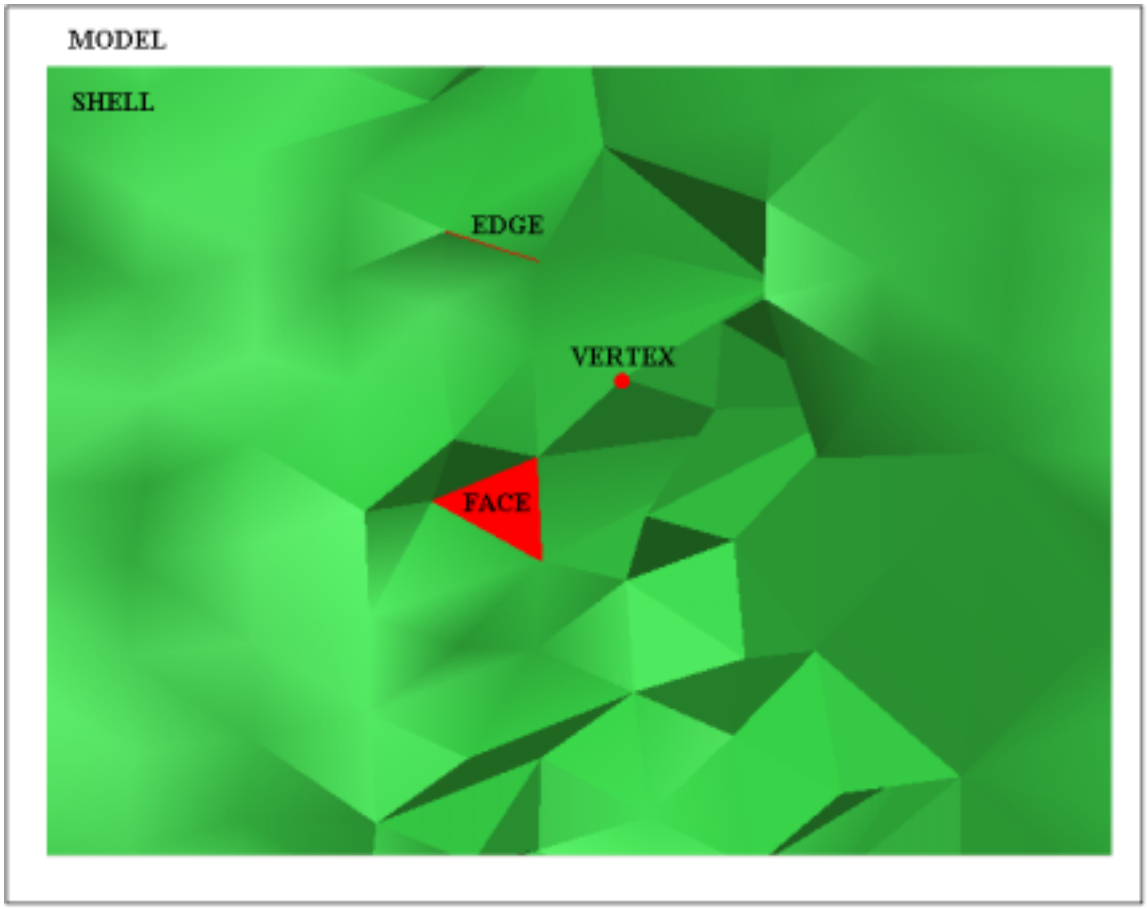

FIG. A.4.1.1. Visual description of model, shell, edge, face, and vertex.

Most of the time, unwanted surfaces such as the platform that the object is placed on appear on scanned data. These surfaces can be easily distinguished and eliminated from real data if the minimum topography of an object is high enough, especially at the edges. For instance, if the topography of an object starts gradually decreasing from the inside towards the edge from centimeters (cm.) to millimeters (mm.), the laser scanner behaves as if it is scanning a smooth hill. The spatial point, in which the edge of an object merges with the platform, looks like a common reflection point in the vertex display. Therefore,

they are not distinguishable. To avoid this problem, an object should be positioned well above the platform. The plexiglas channel structure has steep and thick edges that create distinguishable patterns in vertex display (Figure A.4.1.2).

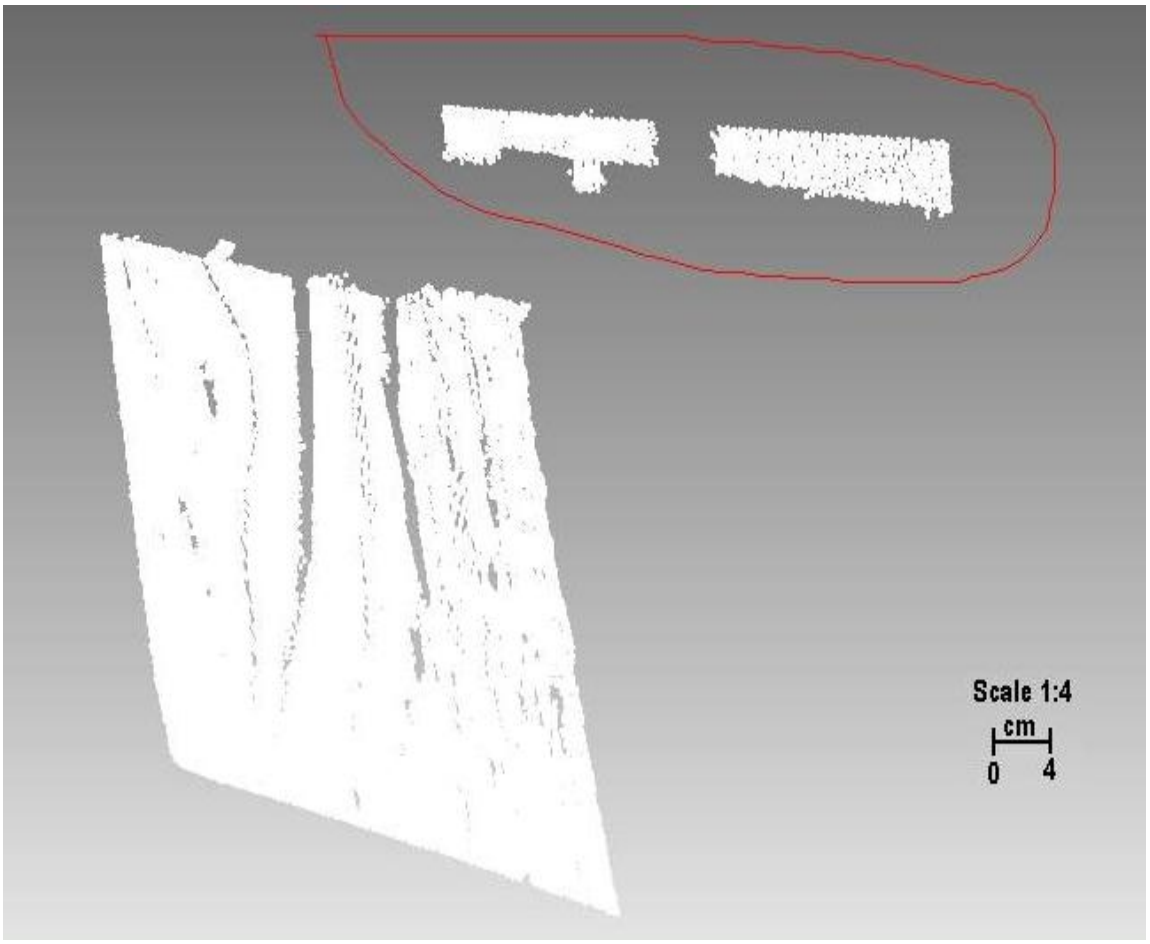

FIG. A.4.1.2. Unwanted platform data is selected in vertex display.

The unwanted platform data were easily identified and removed from the real data. Next, the real channel data free of platform data were exported in an ASCII format for further processing.

A.4.2 Orientation and Redimensioning of Data

Most of the time, the original laser scanned data may not reflect the desired x, y, and z dimensions. To make the numerical model comparable with the physical model, both topographic and seismic parameters must be precisely implemented in the numerical model. In the original laser scanned plexiglas channel dataset, the x and y dimensions contain both negative and positive values. On the other hand, z values are always negative. The reason for both negative and positive values is that acquisition geometry is referenced (x=0, y=0, z=0) to the position of laser scanner transmitter. Since the laser scanner is placed approximately 80 cm above the middle of the channel model, everything below the transmitter position would carry negative values in the z coordinate, and both negative and positive values for x and y coordinates. The orientation of the channel model, in order to prevent missing any topography information during scanning, must be shifted under the laser (Figure A.4.2.1). Therefore, the original data needs to be transformed in terms of x, y, and z.

The most practical and convenient way is to apply a rotation to an object before redimensioning. Once the object edges are on the corner of x and y coordinates, it is easy

to define new reference points (x=0, y=0, z=0). The rotation parameter was defined by measuring the angle between horizontal surface and the lower edge of model. Then, I used computer software (Surfer 8.0) to transform the vertices into the new positions (Figure A.4.2.2).

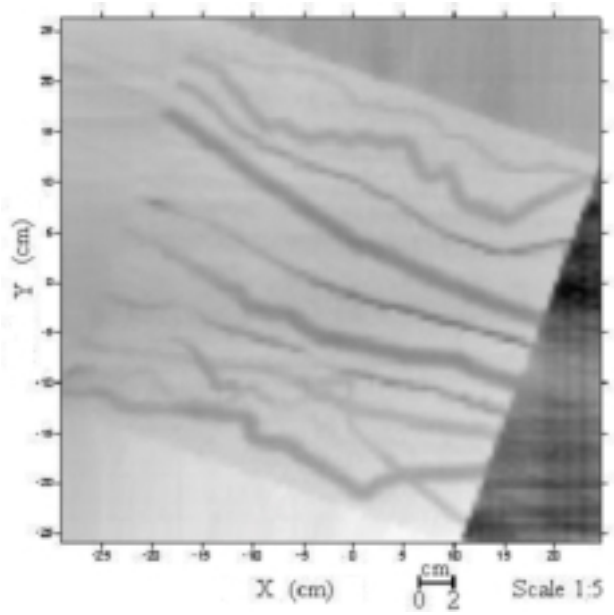

FIG. A.4.2.1. Scanned channel model before redimensioning and rotation.

Next, the rotated dataset were exported in an ASCII format to redefine new x, y, and z coordinate values for each vertex. I applied the following equation in order to bring the original x and y values to a new location with respect to the lower left corner of the data:

$$X_i^{/} = X_i + (-1)*(X_{min})$$

$$Y_i^{/} = Y_i + (-1)*(Y_{min}) \quad , \qquad (4.1)$$

where $X_i^{/}$ and $Y_i^{/}$ are the new locations for vertex (i), X_i and Y_i are the old location for vertex (i), and X_{min} and Y_{min} are the minimum values for x and y in the entire dataset. The conversion of the z values is different from x and y value conversions and is simply:

$$Z_i^{/} = Z_i + h \quad , \tag{4.2}$$

where $Z_i^{/}$ is the new altitude for vertex (i), Z_i is the old altitude for vertex (i), and h is the positive distance between laser transmitter and maximum topographic altitude of model. Finally, I used equation (4.1) to transform the z values into a new reference point appropriate for numerical modeling.

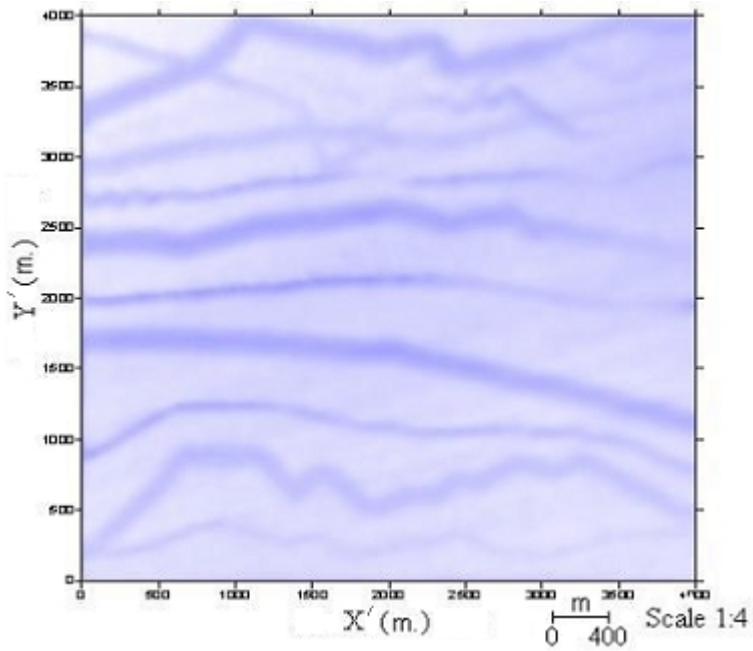

FIG. A.4.2.2. Channel model in new ($x^{/}$,$y^{/}$,$z^{/}$) coordinate system.

A.4.3 Resampling the model data

A regularly sampled dataset is easier to manipulate and often results in more efficient computational algorithms. The numerical model definition in GX-III requires such a regular grid. The 'Point Krigging' method described well by Abramowitz, and Stegun (1972), which:

1. Honors the spacing between the point to be interpolated and the data locations,
2. Honors the inherent length scale of the data,
3. Weights the result by the confidence in the data, and
4. Allows for a preferred orientation of the point to be interpolated.

Point krigging is used in this process flow in order to locate the vertex values at regularly defined grid nodes. As a result, the same picture in Figure A.4.2.2 is visually identical even though the vertices are defined on a regular grid. Figure A.4.3.1 shows the number of nodes in the x and y directions and their locations in 2-dimensional view.

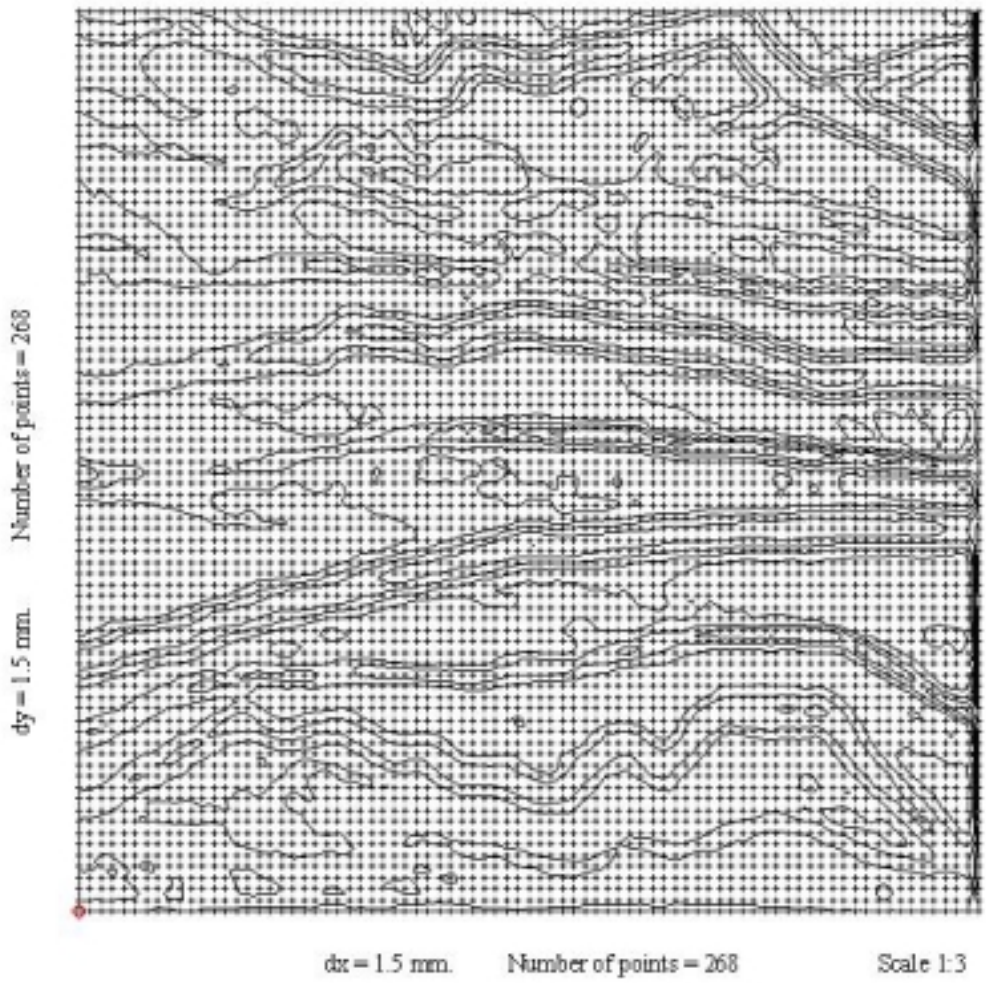

FIG. A.4.3.1. Regularly sampled dataset in x and y directions. Grid increment dx = dy = 1.5 mm, corresponding to world coordinates of 15 m, or my CDP spacing.

A.4.4 Triangulation and Final results

Triangulation is the final process in our flow to project vertices in 3-dimensional space. 3-dimensional visualization honors the presentation and also supplies quality control of the data. Many different triangulation algorithms are developed and used today. For my dataset, I used "Optimal Delaunay Triangulation" provided in the Surfer 8.0 software.

The algorithm creates triangles by drawing lines between data points. The original points are connected in such a way that no triangle edge is intersected by other triangles and the triangles are as equilateral as possible. The result is a patchwork of triangular faces over the extent of the grid. During the patchwork, two faces share only one edge, which is called a manifold edge. Others are defined as non-manifold edge and should be removed from the data.

Each triangle defines a plane over the grid nodes lying within the triangle, with the dip/azimuth and elevation of the triangle determined by the three original data points defining the triangle. All grid nodes within a given triangle are used in the definition of the triangular surface. Because the original data are used to define the triangles, the data are very closely honored. Figure A.4.2.2 is the final result of scanning and processing, and will be used in 3-dimensional numerical modeling study.

APPENDIX B

TRANSDUCER CALIBRATION

B.1 Introduction

Elastic waves exhibit different modes of vibration as they travel through different environments. In air, sound waves move by compression and rarification of air molecules in the direction of movement. In solids, a number of different types of sound waves may be generated (Table B.1.1).

Waves Modes in Solids	**Particle Vibration**
Compressional Waves	Parallel to wave direction
Transverse Waves	Perpendicular to wave direction
Rayleigh Waves	Elliptical orbit - symmetrical mode
Love Waves	Parallel to plane layer, perpendicular to wave direction
Stoneley Waves	Wave guided along interface

Table B.1.1. Possible wave modes in solids.

Acoustic transducers that convert electrical energy to mechanical energy and vice versa are designed to generate either compressional or transverse waves. The core element of most acoustic transducers is a piezoelectric ceramic in which energy conversion happens.

Piezoelectric transducers were first used commercially in early 1950s. Preceding the advent of piezoelectric ceramic, piezoelectric crystals fabricated from quartz and magnetostrictive materials were employed in the design of underwater acoustic transducers. However, today, these types of transducers are rarely used in industry due to the high cost to manufacture and limitations in the piezoelectric properties. When piezoelectric ceramics were introduced they soon became the dominant materials for transducers due to their good piezoelectric properties and their ease of manufacture into variety of shapes and sizes. Barium Titanate was first used as an active piezoceramic material and then following the 1960s, Lead Zirconate Titanate (PZT, where the 'P' corresponds to the chemical symbol Pb, for lead) compositions are being commonly employed to manufacture piezoelectric transducers. Today, many manufacturers offer a wide selection of piezoceramic materials that are available to suit specific applications. The following Table B.1.2 shows some piezoceramic compounds and their characteristics provided by the Center of Nondestructive Evaluation, University of Iowa.

Piezoelectric	Longitudinal Velocity (cm/μ sec)	ε R,	d_{33} (10^{-12} m/v)	g_{33} (10^{-3} vm/n)	Frequency Constant (Hz-m)	Density (g/cm^3)	Acoustic Impedance g/cm^3-sec ($\times 10^5$)
Barium Titanate	0.564	1200	149	14.1	2740	5.55	33.5
Lead Metaniobate							
K-81	0.305	300	85	32	1524	6.2	19
K-83	0.548	175	65	42	2743	4.5	24.5
K-85	0.335	80	180	27	1676	5.7	18.5
PVDF	0.22	12	33	339	1100	1.78	2.5

Table B.1.2. Piezoceramic materials and their properties.

Lead Zirconate Titanate							
PZT-2	0.441	450	152	38.1	2090	7.6	31.3
PZT-4	0.46	1300	289	26.1	2000	7.5	34.5
PZT-5A	0.435	1700	380	24.8	1890	7.75	33.7
PZT-5H	0.456	3400	593	19.7	2000	7.5	34.2
K180	0.4	425	180	41	2006	7.7	31
K270	0.406	1300	270	26	2032	7.5	31
K278	0.406	1100	240	26	2032	7.5	31
K350	0.396	1700	290	25	1981	7.7	30.5
K500	0.396	2700	500	20	1981	7.6	30.5
K550	0.408	3000	550	20	2032	7.8	31
Lead Titanate							
K NTA	0.417	170	62	40	2082	7.5	33
K N3B	0.427	215	70	37	2134	7.65	33
Lithium Niobate							
(Z-cut)	0.773					4.64	34
(Y-cut)	0.688					4.64	31.9
Sodium Bismuth Titanate		140	18	15	2082		
K15	0.417					7.2	29
Lithium Sulfate (Y-cut)	0.546	10.3	15	165	2730	2.06	11.2
Quartz	0.566	4.5	2.3		2830	6.62	15.2
Tourmaline	0.754	7.5			3770	3.1	23.4

Table B.1.2 (Cont'd). Piezoceramic materials and their properties.

Manufacturing transducers is based on part design and inspection. An ultrasonic transducer may be characterized by detailed measurements of its electrical and sound radiation properties. Such measurements can completely determine the response of any

individual transducer. Figure B.1.1 shows the components of a transducer that influence these measurements.

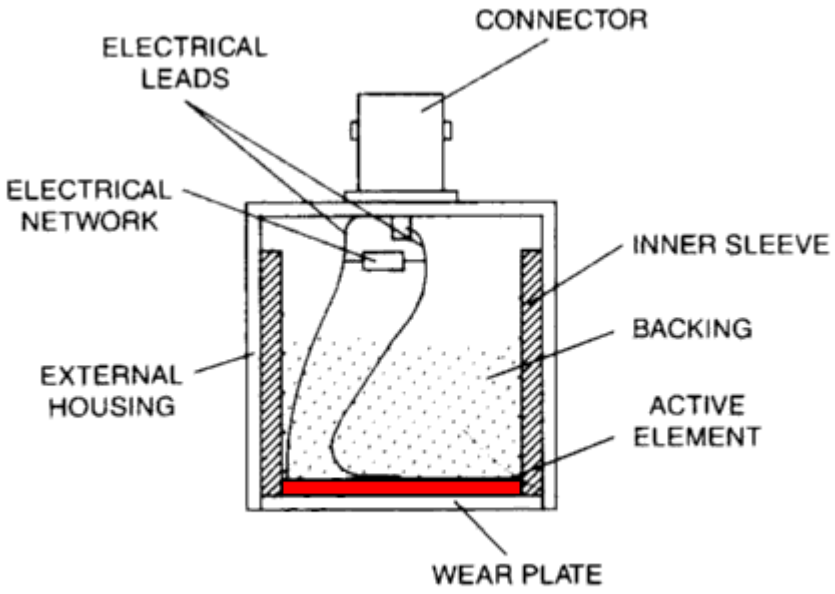

FIG. B.1.1. Piezoceramic contact transducer components.

Backing materials, size and shape of active piezoceramic materials as well as type and length of cable and models of pulser-receivers greatly affect the ultrasonic signals emitted by piezoelectric transducers. Epoxy and araldite doped with tungsten powder are commonly used as backing materials. The job of the backing material is to absorb the energy that radiates in the direction opposite that of the front face of the transducer active element. Increasing the density of backing powder will assess the absorption of sound in a medium according to equation 1.1:

$$Z = \rho * \nu \quad , \tag{1.1}$$

where Z is the acoustic impedance of the material (kg/m^2s), ρ is the density of powder (kg/m^3), and ν is the velocity (m/s). The other effective material, for instance, is the thickness of the active element that changes the desired wavelength of the radiated sound waves. A thin wafer vibrates with a wavelength that is twice its thickness; therefore, piezoelectric crystals are cut to a thickness that is ½ the desired radiated wavelength. Optimal impedance matching is achieved while a matching layer thickness is ¼ of the sound wavelength (Figure B.1.3).

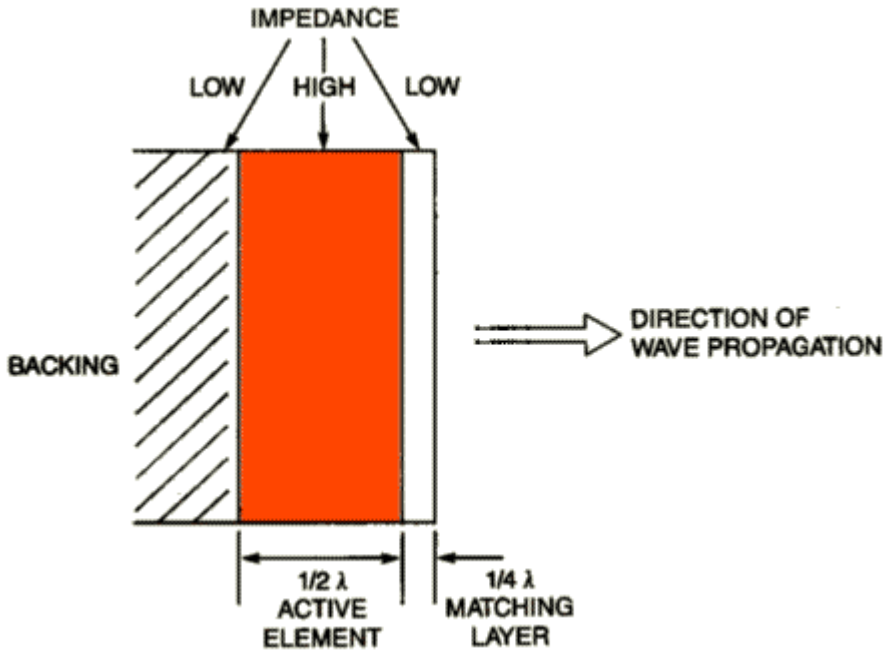

FIG. B.1.2. Thickness (λ) of active element and matching layer of a transducer.

The sound that emanates from a piezoelectric transducer does not originate from a point, but instead, originates from most of the surface of the piezoelectric element. The shape of a piezoelectric transducer, therefore, affects the ultrasound intensity along the beam. The ultrasound beam is extremely complex in the near-field due to variations within this region, known as Fresnel Zone, whereas it is more uniform in the far field, or Fraunhofer Zone, where the beam appears to spread out in a pattern originating from the center of the transducer (Figure B.1.3).

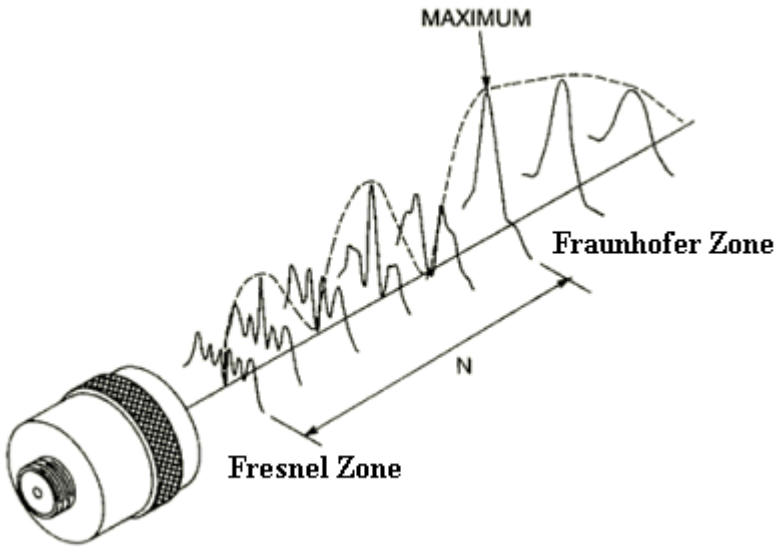

FIG. B.1.3. Beam spread in Fresnel and Fraunhofer Zone.

The transition between these zones occurs at a distance N and is sometimes referred to as the 'Natural Focus' of a flat transducer. The distance N is significant because the amplitude variation reaches its maximum value at that distance and starts to decline smoothly to some finite value.

Beam angle consideration has an important value when selecting a transducer. It simply defines how much the beam will spread with distance. The beam angle is largely determined by the frequency of the sound waves. High frequency transducers produce a narrow beam and on the contrary, low frequency transducers produce a wide beam. Unlike the flat or unfocused transducers, spherical or cylindrical focusing changes the structure of the transducer field by reducing the distance to a point nearer to the transducer focal point. This generates broad band high frequency waveforms.

B.2 Transducer Radiation Pattern Experiment

Several hundreds of physical modeling experiments have been run in the AGL since the 1970s including seismic tomography, illumination, source signature, and multiple. Recently, Wardhana (2001) addressed radiation characteristics of different transducers that are extremely important for seismic attribute analysis. Therefore, this work helps those who deal with physical experiments to determine the variations in radiation pattern for different types of transducers. These variations also occur in different transducers of the same type. Transducer manufacturers usually publish the same performance characteristics for common types of transducers. However, in reality, constructing two identical transducers that have the same performance characteristics may not be possible because of their different size and shape of crystal structures. Consequently, the transducers that are used in physical modeling experiments should be well calibrated.

Wardhana's (2001) methodology was used in this experiment. Furthermore, this experiment was extended into a full semicircle (0^0-180^0 or 0 to π), and plotted in terms of angle interval to get a more sensitive amplitude variation measurements. The same types of Panametrics Acoustic HTI-96-300 spherical transducers that are used in acquisition over physical model are evaluated in this experiment. First of all, a semicircle with the radius of 14.5 cm. was drawn on the bottom surface of the acoustic water tank (Figure B.2.1) and angle points were marked at every 5 degrees. Then, two transducers were placed in the water tank facing each other. One of them was held stationary at middle of the semicircle, and the other was rotated on a semicircle from 0^0 to 180^0 at a constant distance.

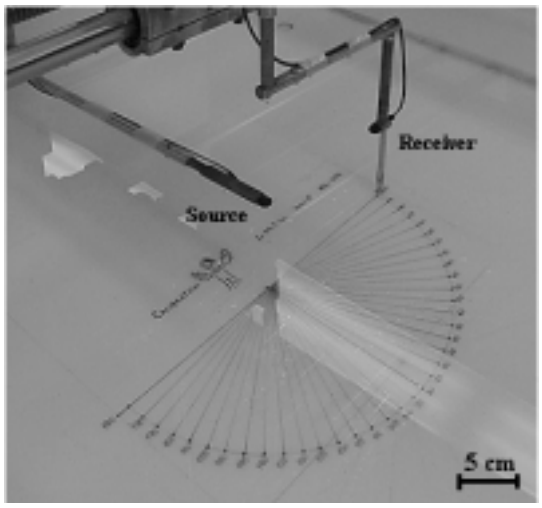

FIG. B.2.1. Radiation pattern data acquisition.

To avoid bottom multiples, and side-effects of acoustic water tank, the transducers were high enough from the bottom part of the tank, and the water level was also kept high

enough above the top of the transducers to eliminate surface multiples. Finally, the Panametrics 5055PR Pulser Receiver was used to collect 30 traces at every 5 degrees of rotation starting from 0^0 and going to 180^0 in order to diminish random background noise in the data that may result from low frequency sources. After vertically stacking the 30 traces from each receiver position, the maximum amplitude value from each corresponding stack trace (Figure B.2.3) was plotted into an angle vs. amplitude graph (Figure B.2.2).

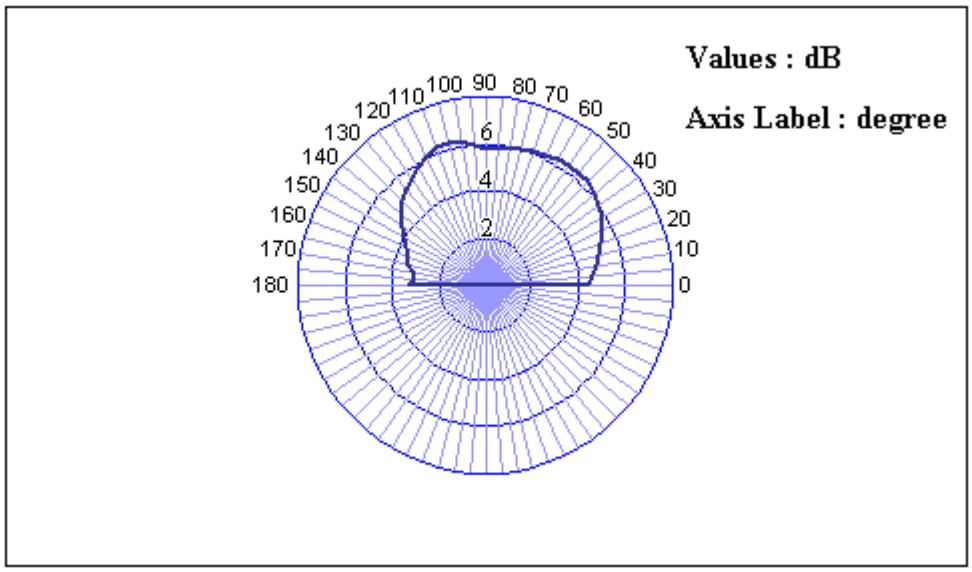

FIG. B.2.2. Amplitude-Angle directivity of a single 300 kHz Panametrics HTI-96-300 spherical transducer printed from the data shown in Figure B.2.3.

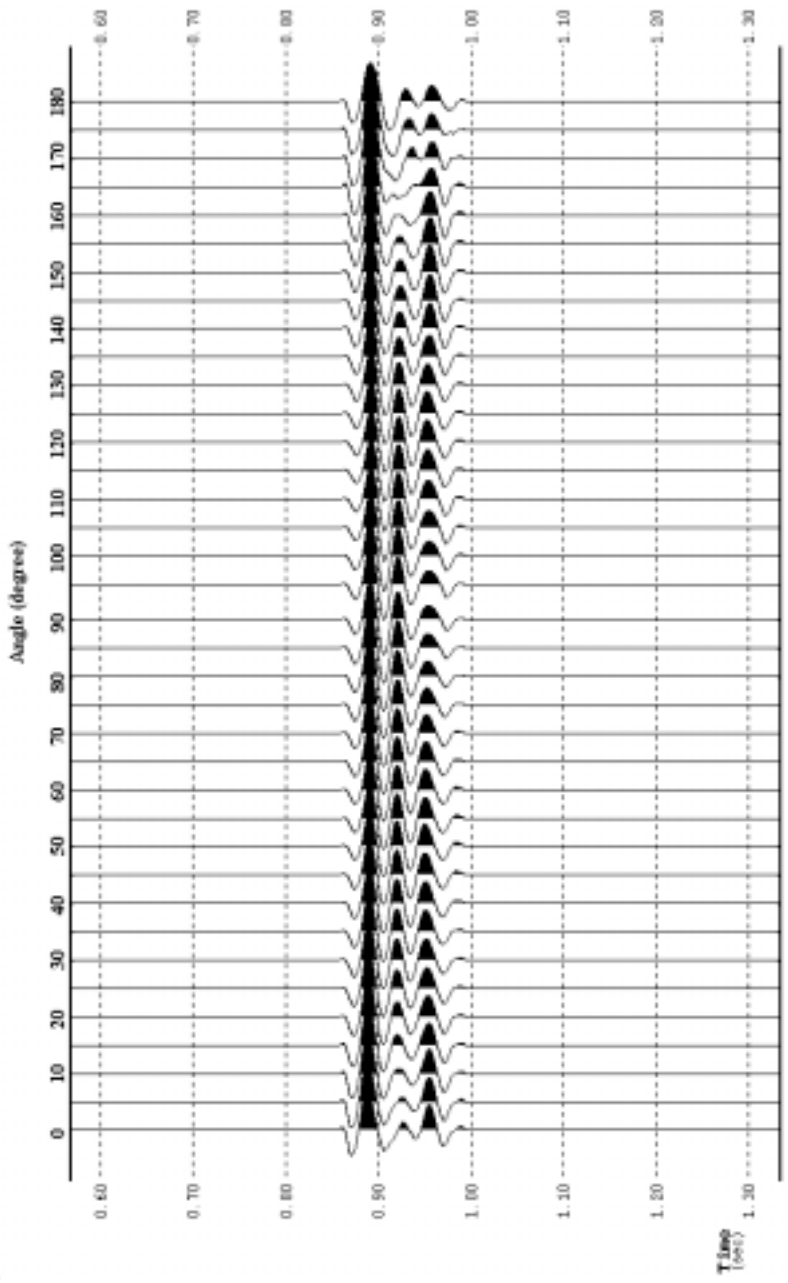

FIG.B.2.3. Seismic traces from 0 to 180 degrees with 5 degrees angle increment of a pair of Panametrics HTI-96-300 spherical transducers. Note the change in waveform for angles $\theta<20^0$ and $\theta>145^0$.

As mentioned before, transducers show different radiation patterns due to their different characteristics and shapes. The amplitude vs. angle graph demonstrates that the radiation of ultrasonic sounds from this particular Panametrics HTI-96-300 spherical transducer vary dramatically from one side to another. These data are also printed out in (Table B.2.1).

Side 1 (0-90) (degree)	Amplitude Variations (dB)	Side 2 (90-180) (degree)	Amplitude Variations (dB)
0	0.0000	90	0.2093
5	0.3605	95	0.3020
10	0.4333	100	0.0595
15	0.3763	105	-0.0456
20	0.3554	110	-0.2602
25	0.4202	115	-0.3142
30	0.3907	120	-0.3641
35	0.2801	125	-0.3407
40	0.2073	130	-0.5837
45	0.1337	135	-0.5912
50	0.0856	140	-0.6136
55	-0.0226	145	-0.6404
60	-0.0472	150	-0.6217
65	-0.0670	155	-0.4861
70	-0.1362	160	-0.3886
75	-0.1297	165	-0.5580
80	-0.0870	170	-0.2409
85	-0.0976	175	0.5089
90	-0.0238	180	0.0000
Min. Var. Max. Var. High/Low Var.	0.02 dB 0.4 dB 3 dB	Min. Var. Max. Var. High/Low Var.	0.2 dB 0.5 dB 6 dB

Table B.2.1. Amplitude variations from trace to trace in decibel unit.

The amplitude variation between each trace in the first quarter (0^0-90^0) is reasonably acceptable (minimum 0.02 dB. and maximum 0.4 dB.) and changes within a very small percentage. However, in the second quarter from 90^0 to 180^0 of the face of transducer, the radiation pattern drastically changes from the symmetry expectations. The amplitude, in this portion varies from a low of 3 dB to a high of 6 dB. Imperfection of active element roundness of piezoelectric transducer may be one of the reasons for this unexpected behavior of the transducer. Consequently, the same transducers, employed in acquiring the data in the physical facility, should be used to calibrate the amplitude of the data because even the same type of transducers may show variations in radiation patterns. Although transducers are expensive, in the future, I recommend that physical modelers choose a pair of transducers with as uniform radiation pattern as possible.

APPENDIX C

3-D RAY TRACING MODELING

C.1 Introduction

Numerical modeling is an alternative for generating synthetic seismic records to physical modeling from 2-D or 3-D earth models. Since numerical models mimic true geologic structures, the synthetic data will be useful in order to illuminate, understand, and improve current acquisition surveys and seismic imaging algorithms. There are two approaches for numerical modeling: 1. Ray theoretical (Julian *et. al.*, 1977), and 2. Wave theoretical (Daley *et. al.*, 1999). Both approaches have common concerns about calculating travel-times and ray-paths for a given subsurface model. As it relates to this study, I will now discuss ray theory based numerical modeling.

Ray theory based numerical modeling can be classified under three categories: 1. One-point ray tracing, 2. Two-point ray tracing, and 3. Three-point ray tracing. Traditionally two methods are used to calculate seismic ray paths between two points in the earth. The first one is the shooting method, which is an example of one-point ray tracing, which tries to find ray path by solving the differential equations that follow the ray theory from different initial conditions until the trial ray arrives at the preassigned point (Moser, 1991). In other words, the ray iteratively propagates in different directions (fan shooting)

from the same initial position until the ray path falls within the source and receiver offset. The second method is the bending method that can be counted as an example of two-point ray tracing. The bending method tries to find the shortest ray path between two points. As it searches, a ray path connected to those two fixed points becomes systematically bent until it converges to the true ray path, Fermat's path. Julian, (1977) and Moser, (1991) discussed the advantages and drawbacks of these methods. They showed that the bending method is both efficient and flexible compared to shooting method. However, the bending method is still computationally expensive when a large number of ray paths are considered. Finally, three-point ray tracing may include the third point in the subsurface as a diffractor or a reflection point beside the fixed source and receiver points.

C.2 Model Parameterization and Acquisition Survey

In this study, I will use a kinematic two-point ray tracing package program provided by GX-Technologies. Therefore, by means of kinematic ray tracing, our concern will be the travel times and ray path computations without dealing with the waveforms (amplitude and phase). Prior to designing the acquisition survey in ray tracing, I built the sub-surface model, which mimics our physical model, by using thickness and length information of each layer (See Chapter 2, Figure 2.2 and also Appendix A for a description of my channel model). I then defined model parameters including P-velocity, V_p, S-velocity, V_s, and density, ρ, (see Chapter 2, section 2.1) for each layer that represents our complete

physical model. Figure C.2.1 shows one of the inline profiles that represents a cross sectional view of the physical model.

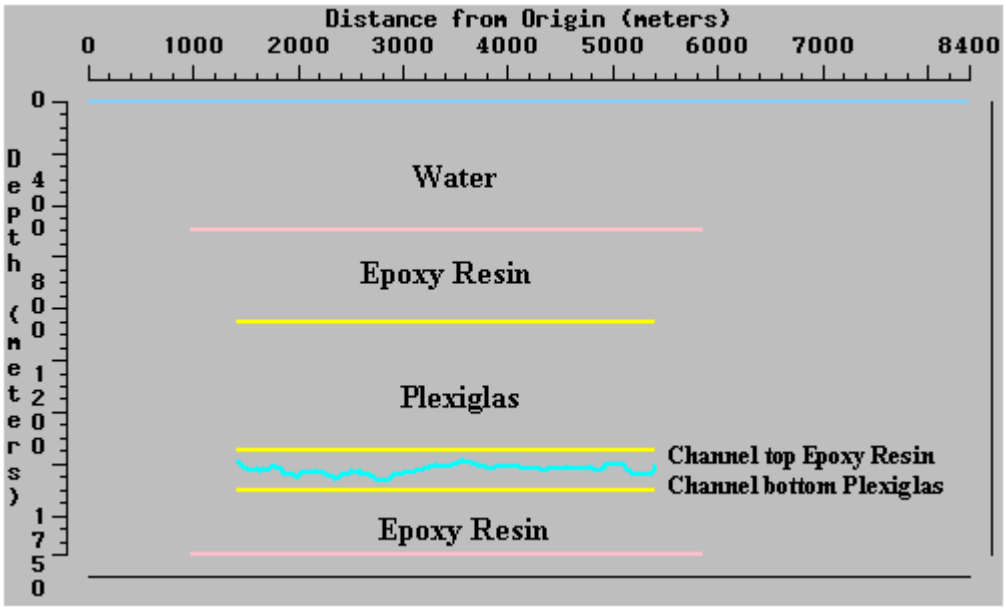

FIG.C.2.1 Model profile in crossline direction, presents layers of physical model.

To make comparable imaging results of both the 3-D physical and ray-trace models, in the survey designing phase, I tried to remain loyal to a 3-D four-streamer marine acquisition survey (see Chapter 2, Figure 2.5) acquired over the physical model. However, considering current limits in the ray-tracing package including the number of shots per line, the number of lines, and the number of receivers per shot, the results were limited in order to avoid low efficiency and incomplete results. As a result, 150 receivers were employed for each shot, and a total of 840,000 traces were generated during the survey. Figure C.2.2 and Figure C.2.3 consecutively show survey coverage over the

model and 3-D ray-path from one shot point. I also generated an illuminated map for each layer (Figure C.2.4). It can be observed that the illumination of the channel area and the bottom resin layer is very irregular when compared to that of the top of the plexiglas layer and the epoxy resin layer. I conclude that the illumination of the deeply buried layers suffers due to lack of diffractions in the ray tracing process and to the low critical angle for the ray path at larger offsets.

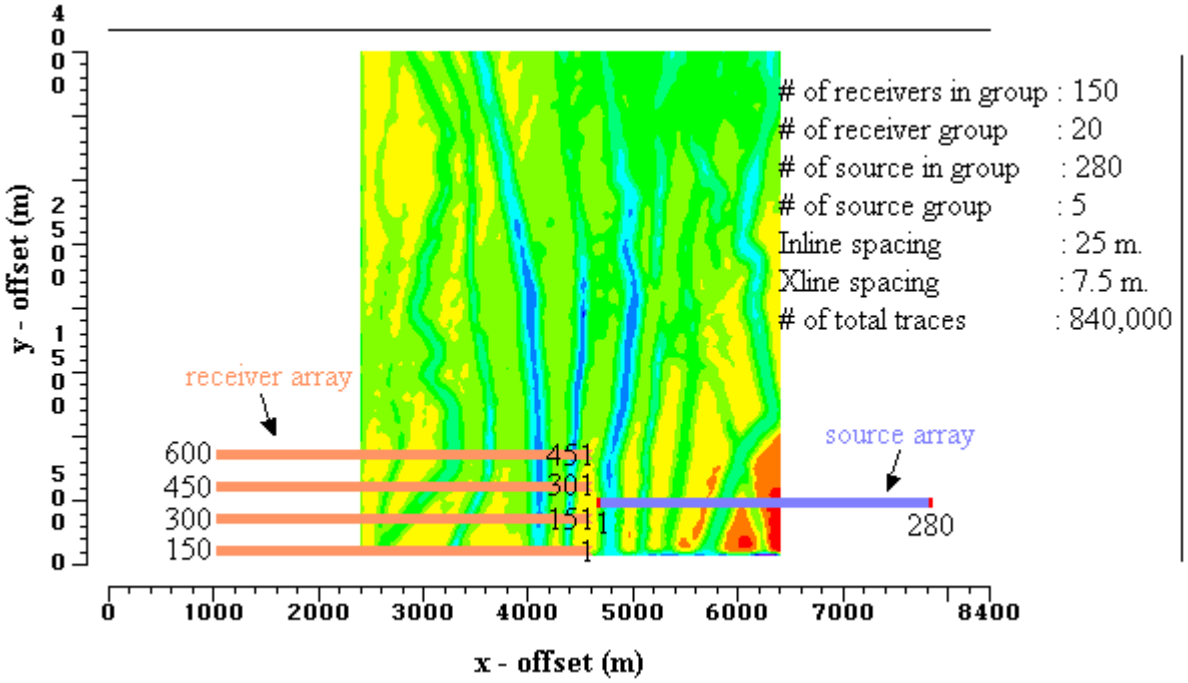

FIG.C.2.2. Ray tracing acquisition geometry, the channel model appears in the background to give an idea about where the acquisition starts and ends.

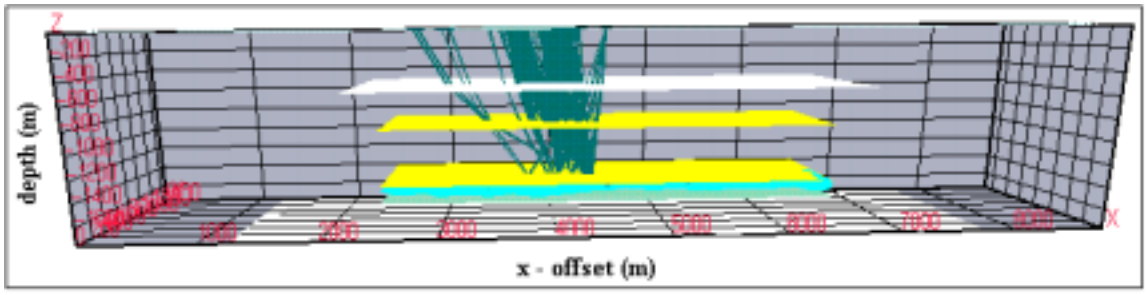

FIG.C.2.3. 3-D Ray-path over channel area from one shot point.

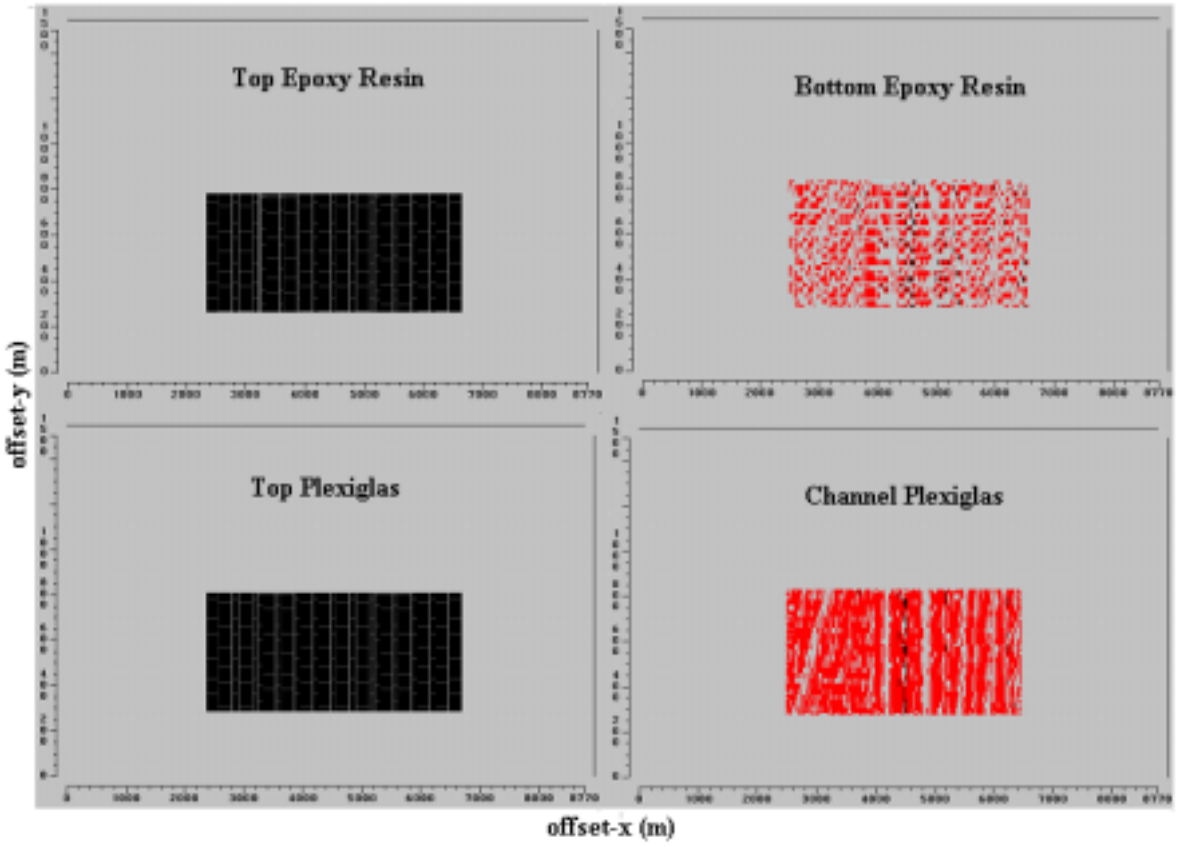

FIG.C.2.4. Illumination maps of various layers.

C.3 Imaging

Once all the parameters for the seismic survey were determined, a total of 1400 shot gathers were generated and preprocessed as described in Chapter 3, section 3.2. A 3-D Pre-stack Kirchhoff Time Migration was performed on the ray-traced model data. The imaging results from both physical and ray-tracing model were discussed in Chapter 3, section 3.11.2, Figure 3.11.1 and 3.11.2. Figure C.3.1 shows one of the shot gathers from the ray trace data.

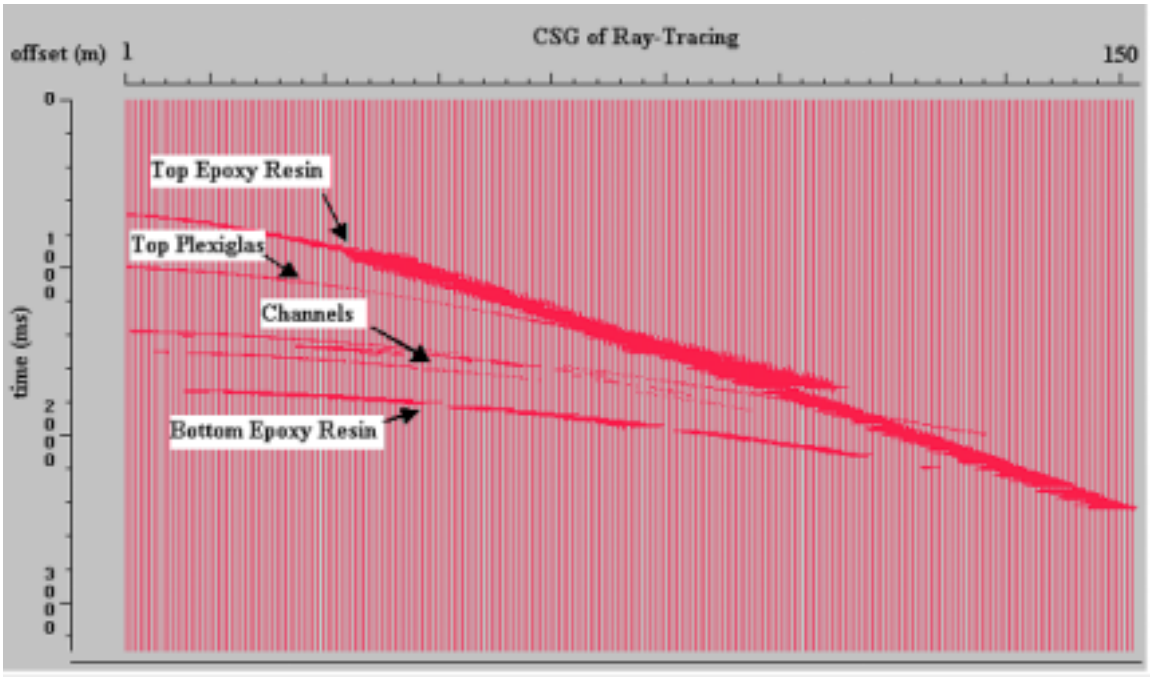

FIG.C.3.1. An example of ray-trace generated common shot gather.